THEORY AND SIMULATION OF COLLOIDS NEAR INTERFACES: QUANTITATIVE MAPPING OF INTERACTION POTENTIALS

A Dissertation

by

MINGQING LU

Submitted to the Office of Graduate Studies of
Texas A&M University
in partial fulfillment of the requirements for the degree of

DOCTOR OF PHILOSOPHY

August 2007

Major Subject: Chemical Engineering

THEORY AND SIMULATION OF COLLOIDS NEAR INTERFACES: QUANTITATIVE MAPPING OF INTERACTION POTENTIALS

A Dissertation

by

MINGQING LU

Submitted to the Office of Graduate Studies of
Texas A&M University
in partial fulfillment of the requirements for the degree of

DOCTOR OF PHILOSOPHY

Approved by:

Co-Chairs of Committee,	David M. Ford
	Michael A. Bevan
Committee Members,	Tahir Cagin
	Kenith E. Meissner
Head of Department,	N.K. Anand

August 2007

Major Subject: Chemical Engineering

ABSTRACT

Theory and Simulation of Colloids near Interfaces:
Quantitative Mapping of Interaction Potentials. (August 2007)
Mingqing Lu, B.S., Daqing Petroleum Institute
Co-Chairs of Advisory Committee: Dr. David M. Ford
Dr. Michael A. Bevan

The behavior of dense colloidal fluids near surfaces can now be probed in great detail with experimental techniques like video and confocal microscopy. In fact we are approaching a point where quantitative comparisons of experiments with particle-level theory, such as classical density functional theory (DFT), are appropriate. In a forward sense, we may use a known surface potential to predict a particle density distribution function from DFT; in an inverse sense, we may use an experimentally measured particle density distribution function to predict the underlying surface potential from DFT. In this dissertation, we tested the ability of the closure-based DFT to perform forward and inverse calculations on potential models commonly employed for colloidal particles and surface under different surface topographies. To reduce sources of uncertainty in this initial study, Monte Carlo simulation results played the role of experimental data. The accuracy of the predictions depended on the bulk particle density, potential well depth and the choice of DFT closure relationships. For a reasonable range of choices of the density, temperature, potential parameters, and surface features, the inversion procedure yielded particle-surface potentials to an accuracy on the order of 0.1 k_BT. Our results demonstrated that DFT is a valuable numerical tool for microcopy experiments to image three-dimensional surface energetic landscape accurately and rapidly.

To my wife Ani Ma and my lovely son Kevin M. Lu.

ACKNOWLEDGMENTS

Firstly, I would like to express my sincere appreciation to my advisor Dr. Ford for his invaluable guidance and help in this research. Dr. Ford's kindness, enthusiasm and great ability built a role model for me. He has provided me with constant encouragement to help me through difficult situtations during my 4 years studying at Texas A&M. I've learned a lot from him, especially on how to sell your idea and how to approach the problem step by step during our numerous personal meetings. I have no doubt that those wonderful experiences will benefit me for a long time.

I sincerely thank my co-advisor Dr. Bevan for inculcating in me the need to look at results from a different perspective and to be careful about small details. I really enjoyed the excellent environment of his group, which broadened my knowledge in colloidal science and educate me to make decent presentations.

I would like to thank my committee Dr. Cagin and Dr. Meissner for all their help and suggestions. I express my gratitude to members of the Bevan research group: Wu, Pradip and Richard for experimental support and discussions.

I always appreciate the admission committee of the chemical engineering department and in particular, Dr. Anthony. My invaluable thanks are attributed to all of the professors in the courses I took and to the wonderful support staff in the department. I've been delighted to have such wonderful professors, teachers, and friends (Jie Yang and Xianchun Wu in particular) who helped me a lot through my academic career.

Lastly, I owe an immeasurable amount of gratitude to my wife Ani Ma, without her all of this would not have been possible.

TABLE OF CONTENTS

Page

Page

Page

LIST OF FIGURES

FIGURE Page

FIGURE Page

FIGURE Page

FIGURE Page

FIGURE Page

LIST OF TABLES

1. INTRODUCTION

1.1 Objectives and Significance

Colloidal particles are small objects with a size range from 1nm to 10μm and have been employed in many industries such as foods, emulsions, paints, coatings, ceramics, photonic crystals, and novel electronic devices.[1] The structure of colloidal dispersions near surfaces is frequently important, particularly in applications such as coatings, where a given micro-structure is desired on a surface. Furthermore, colloidal structure under confinement is increasingly important to the assembly and function of nano- and micro-scale materials and devices. The coming age of biotechnology in the next several decades will provide the impetus for the quantitative understanding of the properties of the surfaces and interfaces such as liquid crystals, colloidal dispersions, and self-assembling.[2] The weak, non-covalent nature of the multi-body and multi-dimensional k_BT-scale interactions in these systems competes with the entropy of the system will lead to a rich variety of microstructures and phases.[2]

The larger size of the colloidal particles compared with atoms makes it feasible to use optical and scattering techniques to study their behavior. For instance, confocal scanning laser microscope (CSLM),[3] atomic force microscopy (AFM),[4] total internal reflection microscopy (TIRM),[5] video microscopy (VM)[6] and Diffusing Colloidal Probe Microscopy (DCPM)[7] have been used in imaging colloidal particles.

On the simulation side, tools for atomistic simulation such as Monte Carlo (MC) and molecular dynamics (MD)[8] have been extensively used to study colloidal dispersions since the pioneering work by Snook and Henderson in 1978.[9] Molecular simulations calculate macroscopic properties such as pressure, internal energy, and so on

---

This dissertation follows the style of The Journal of Chemical Physics.

using microscopic level information;[8] their results may be considered "exact" for a given choice of the interaction potential model, within statistical limitations. On the theoretical side, classical density functional theory (DFT) has been a useful tool for studying colloidal dispersions.[10-12] A major advantage of DFT is that it predicts equilibrium density profiles and associated thermodynamic properties at a computational cost significantly lower than that required for direct molecular simulation methods. In DFT one expresses the grand potential for the inhomogeneous system as a functional of single-particle density, which upon minimization yields the equilibrium density distribution of the system. Integral equation theory (IET), which predicts structural correlation functions in fluids, is a close relative of DFT. In IET, one solves the Ornstein-Zernike (OZ) equation with a suitable closure to obtain particle–particle correlations such as the radial distribution function $g(\mathbf{r}_1,\mathbf{r}_2)$ and the direct correlation function $c(\mathbf{r}_1,\mathbf{r}_2)$.[10] IET is used most often to predict properties of bulk fluids,[13] but it may be used directly to obtain the structure of inhomogeneous fluids as well.[14,15]

There has been a large amount of research done on the structure and dynamics of colloidal particles near surfaces. However, the vast majority of the work done by either simulation or DFT and IET has been to solve the "forward problem," i.e., given the particle-particle and particle-surface potentials, predicting the structural properties. Since one of the key expectations underlying DFT is a unique correspondence between external (e.g. surface) potential and density profile, DFT can also be used to solve "inverse problem" i.e., given the particle-particle potentials and the structural properties, predicting particle-surface potentials. Thus, we expect that if we extract an equilibrium density profile $\rho(\mathbf{r})$ from the experimentally measured particle trajectories, we can invert it to obtain the colloid-surface potential $\varphi_{ext}(\mathbf{r})$ by inverse DFT. The requirements for the inverse DFT approach are:

(1) Accurate to within the inherent experimental limitations, typically on the order of 0.1 k_BT,

(2) Fast enough to report a surface potential within minutes on a computer workstation,

(3) Systematically adaptable to a range of different particles and surfaces features.

To achieve the goal of this research, we studied four particular problems in this dissertation: (1) measuring colloidal particle-surface interactions on homogeneous planar surface, (2) obtaining colloidal particle-surface interactions on homogeneous planar surface under gravity, (3) studying colloidal self-assembly on chemically and physically patterned surfaces, (4) investigating monolayer colloidal self-assembly on patterned surface.

1.2 Background

In this section, the current experiment techniques for colloidal dispersion are briefly reviewed first; reviews for particle-based simulation and modeling efforts such as DFT and IET follow.

1.2.1 Confocal scanning laser microscope (*CSLM*)

The original concept for CSLM was originally developed by Marvin Minsky[16] in 1953; it became a standard technique toward the late 1980s after the development of laser and computer power. CSLM is a valuable tool for obtaining high resolution images and 3-D reconstructions; it is able to produce blur-free images of thick specimens at depths up to 100 μm.[3] In CSLM, a laser beam is used to provide the excited light to get very high intensities. Dye in the sample fluoresces and omits light to pass through a pinhole and then is detected by a photo-detection device (photomultiplier tube); data is recorded by a computer after being transformed from a light signal to an electric signal.

CSLM has recently become an invaluable tool in interfacial fluids, crystalline and glass state investigations that allows individual particles to be imaged within a three dimensional assembly in real space.[17] Several pioneering studies have been carried out to directly probe the structure and dynamics of colloidal crystals[18] and glasses[19,20] in

bulk systems using CSLM. Two advantages of CSLM are: it is ability to provide simultaneous qualitative and quantitative information on surfaces; and to measure a wide range of surface areas. The primary disadvantage of CSLM is due to the limited number of excitation wavelengths, which make it an expensive process.

1.2.2 Atomic force microscopy (AFM)

AFM was invented by Binnig *et al.*[21,22] and is one of the principal tools for imaging, measuring and manipulating matter at the nano-scale. It directly detects the interaction between a surface and a fine tip, which ranges in size from 10nm to 100nm.[23] The force AFM can measure is on the order of 10^{-9}-10^{-10} N[24] between a tip and the surfaces. Different objects, such as colloidal particles,[4] polymer and lipid films[25], single DNA molecules[26], and oil droplets,[27] also be attached to the tip to measure force between a given object and surface.

The advantages of AFM include the following: it can provide a true three dimensional surface landscape; no special treatment to samples are needed; it can operate in ambient air or even in liquid; it can accurately measure the interactions between a single object (e.g. colloids, proteins, DNA) even as small as a molecule and a templated surface. In contrast, the disadvantages of AFM include its inability to image large surface areas (the maximum area AFM can measure is 150μm×150μm); absolute separations between surfaces can not be determined directly; the deformation of the fine tip would increase the difficulties to interpret the AFM results.

1.2.3 Total internal reflection microscopy (TIRM)

TIRM is first developed by Prieve *et al.*[28] to measure particle-particle and particle-surface interactions for colloidal particles levitated above the surface. Particle-wall instantaneous separation can be determined by measuring scattering intensities and can not be measured directly. To levitate a colloidal particle, an electrostatic or polymeric repulsive force needs to balance the gravitational force, and Brownian motion will cause excursions around the position where the sum of the forces equals zero. The

equilibrium probability distributions of particle heights can be measured by TIRM, and particle-surface potential profiles can be calculated from distributions by using Boltzmann's equation. The minimum accurate force TIRM can measure is as low as 10^{-14} N with resolution of particle wall separations around 1nm.

Since it's invention, TIRM was widely used to measure different forces for both colloidal particle-particle and colloidal particle-surface, including electrostatic repulsions[28,29], van der Waals[30-32], polymeric[32], depletion,[33] and biological forces[34]. TIRM can also measure the hindered diffusion by measuring instantaneous separations.[31,32] The advantage of TIRM includes its higher resolution and flexibility; it can measure weaker interactions than AFM. The disadvantage of TIRM includes forces must be measure in solution; it lacks lateral excursion information; and it is necessary to calibrate scattering intensities of stuck particles to obtain absolute separations between particles and surfaces.

1.2.4 Video microscopy (VM)

In VM, a cool charged coupled device (CCD) camera is used to track the colloidal particles lateral trajectories and structure so dynamics properties can then be interpreted. The main application of VM includes the measurement of equilibrium distribution functions such as radial distribution $g(r)$ or interaction potentials in pseudo two-dimensional colloidal systems. For example, the effective particle-particle pair potential can be determined from the $g(r)$, directly observed from VM by solving the Ornstein-Zernike (OZ) equation[10,35] or inverse Mote Carlo simulations[36]. The resolution of VM is lower than that of TIRM.

1.2.5 Diffusing colloidal probe microscopy (DCPM)

Diffusing Colloidal Probe Microscopy (DCPM) is an emerging surface analysis technique currently being developed by M.A. Bevan.[7] In DCPM, an ensemble of freely diffusing nanoparticles are employed as ultra-sensitive probes of a nearby surface. Total internal reflection[5] and video[37] based optical microscopy techniques, which combine the scattering of an evanescent wave with standard image capture and analysis algorithms,

are used to monitor the three-dimensional Brownian excursions of the colloidal particles as they sample spatial positions over time. The particle trajectories may then be analyzed using statistical mechanical interpretations to yield the relative potential energy of a single colloidal particle as a function of *xyz* position near the surface.

Because DCPM takes advantage of nanoparticle Brownian motion as a natural gauge of potential energy landscapes, it is inherently capable of measuring energies and forces 10^3 times weaker[5] than the range accessible using "top down" methods employing external mechanical manipulation (i.e. scanning probes,[38] optical tweezers[39]). Preliminary work[7] has successfully implemented DCPM to perform ensemble measurements in model synthetic systems, and the technique is currently being extended to measure specific equilibrium protein interactions,[40] with protein binding pairs covalently attached to nanoparticles and flat surfaces.

1.2.6 Particle-based simulation

Simulation plays two pivotal roles in the current nano-scale research.[8,41] First, it can serve to test interaction potential models by comparing the properties from simulations with experimental results. Simulation, therefore, gives aid to guide the physical experiments. On the other hand, it can be used to test theories developed by theoreticians. In this case simulations can screen the theories and play the role of experiment. So some researchers call the process as a *computer experiment*.[41]

MC simulation is one of the basic techniques in the molecular simulation world. MC simulation is called so because it uses computer-generated random numbers.[41] Since it is a probabilistic way of calculating macroscopic properties, the use of MC is limited to the calculation of equilibrium properties.

1.2.7 Density functional theory (DFT)

DFT is based on the idea that the free energy of the inhomogeneous fluid can be expressed as a functional of particle distribution density $\rho(\mathbf{r})$ and all the relevant thermodynamic functions can be calculated based on this. Moreover, the microscopic structure of inhomogeneous fluids can be determined from this function.[42] One of the

key advantage of DFT is that there is unique functional between intrinsic Helmholtz free energy and interatomic or interparticle potential energy. Also, this free energy has the same dependence on $\rho(\mathbf{r})$ for all $\varphi_{ext}(\mathbf{r})$.[42] Another advantage of DFT is that it is able to describe the macroscopic system accurately but with much lower computational cost compared with molecular simulations such as MC. The final one is that DFT is applicable to both uniform and confined systems within a self-consistent theoretical framework.[11]

The major goal of DFT is to find suitable approximations for free energy functionals (for a given type of fluid) that are computationally tractable and that are sufficiently accurate for application in a wide range of problems (remain accurate for various choice of $\varphi_{ext}(\mathbf{r})$). There are many different ways of approximating the free energy functional,[42] such as the local density approximation (LDA), weighted density approximation (WDA), fundamental measure theory (FMT), and perturbative density functional theory (PDFT). The LDA uses a point-wise description of the free energy density and is not accurate enough to predict the rapid density oscillations typical of the first few layers of a confined fluid.[43] The WDA concept represents a major improvement by employing a weighted-average density over a local volume,[42] and Rosenfeld's FMT is a highly accurate geometry-based approach for the weighting functions of hard sphere systems.[44] The PDFT is based on a functional Taylor series expansion of the excess free energy around the homogeneous (bulk) fluid reference state; the coefficients are the direct correlation functions of the bulk fluid.[12] Zhou and Ruckenstein[45] provided a new approach to PDFT, recognizing that the sum of terms of order $n>2$ is equivalent to the bridge functional from Ornstein-Zernike (OZ) integral equation theory (IET); calculations by this approach require the second-order direct correlation function of the bulk fluid and a choice of closure in the sense of OZ theory.

DFT has been applied to a wide range of problems,[11,12] but in this dissertation we are primarily concerned with inhomogeneous colloidal fluid phases under different surface features. Several DFT-based studies on that particular topic have been carried

out using hard sphere,[46,47] hard sphere + Yukawa tail,[48,49] Derjaguin–Landau–Verwey–Overbeek (DLVO),[49,50] soft repulsion,[43] and depletion[51] interaction potentials.

1.2.8 Integral equation theory (IET)

IET, which predicts structural correlation functions in fluids, is a close relative of DFT and it describes a fluid with a somehow approximation but with coherence to the 'exact' molecular simulation techniques. As a result, the performance of IET, such as thermodynamic and structural properties predicted by IET should be checked with the corresponding molecular simulation systematically. IET is an irreplaceable tool of investigation of fluid state. The advantages of IET include that it is much faster than molecular simulation but with general good results; no sampling problems of very dilute phase as it happens in molecular simulations, which may fall into secondary energy minima and cause severe ergodicity problem.[13] The disadvantage of IET includes t it is not very accurate for the critical behavior of fluids in three dimensions.[13]

In IET, one solves the OZ equation with a suitable closure to obtain particle–particle correlations such as the radial distribution function $g(\mathbf{r}_1,\mathbf{r}_2)$ and the direct correlation function $c(\mathbf{r}_1,\mathbf{r}_2)$.[10] IET is used most often to predict properties of bulk fluids,[13] but it may be used directly to obtain the structure of inhomogeneous fluids as well.[14,15] In addition to numerous applications to atomistic liquids, IET has been applied to bulk colloids fluids using direct Coulombic,[52-54] hard sphere + Yukawa tail[55,56], DLVO,[54] and depletion[57,58] interaction potentials and to confined colloids with hard sphere,[59] adhesive sphere,[60] hard sphere + Yukawa tail,[61] and DLVO[62] potentials.

1.2.9 Forward and inverse analysis

MC and DFT are traditionally used in a "forward" fashion to predict density distribution $\rho(\boldsymbol{r})$ from particle-particle interaction potential $u(\boldsymbol{r})$ and external potential $\varphi_{ext}(\mathbf{r})$. Conversely, the inverse MC algorithm[8] employs iterative forward canonical MC simulations with different guesses for $\varphi_{ext}(\mathbf{r})$ until a simulated $\rho_s(\boldsymbol{r})$ is obtained in agreement with the measured $\rho(\boldsymbol{r})$; the inverse for DFT is simpler since the

unique relationship between the $\rho(\mathbf{r})$ and $\varphi_{ext}(\mathbf{r})$ in DFT. The main requirement for the inverse analysis is speed (i.e. to complete the surface potential calculation in minutes, not days, which is essential for the biotechnology application) and this precludes the use of inverse MC which requires millions of cycles to converge. Another advantage of DFT over inverse MC is the uniqueness of solution where it is possible to prove that solution of the inverse MC is unique, but until recently there were no practically realistic way to find it.

An analogous inverse problem arises for homogeneous fluids, and noting its parallel with the current problem is worthwhile. For homogeneous fluids of particles (either atomistic or colloidal), one would often like to deduce the pairwise particle-particle interaction potential from the experimentally determined radial distribution function $g(r)$ by fundamental-measure free-energy density functional for hard spheres.[63]

1.3 Summary

In this dissertation, we described forward and inverse DFT modeling for dense colloidal fluids at interfaces, which will be a great tool for colloidal microscopy experiments such as confocal scanning laser microscope (CSLM), Diffusing Colloidal Probe Microscopy (DCPM) and so on.

Our studies shows that forward DFT can successfully predict the particle-level structure through comparison with Monte Carlo simulations for different colloidal fluid interaction models (such as hard sphere, Derjaguin-Landau-Verwey-Overbeek (DLVO) screened electrostatic repulsion, retarded van der Waals (vdW) attraction, and Asakura-Oosawa (AO) depletion attraction) under confinement, sedimentation, self-assembling on chemically and physically patterned surfaces, self-assembling monolayer on physically patterned surface; the inverse DFT can quantitative predicted the particle-surface interaction for the systems described in forward DFT using the Monte Carlo simulation data as inputs. The accuracy of the inverse DFT predictions depended on the bulk particle density, potential well depth and the choice of DFT closure relationships. For colloidal fluids under confinement, it produces decent results ($< 0.1\ k_BT$ maximum

deviation from true potential) at low to moderate bulk densities ($\rho_b\sigma^3 < 0.3$) across the different colloidal interaction types. For colloidal sedimentation equilibrium, it produces good results (< 0.2 k_BT) at low total density ($\rho_{total}\sigma^3$=0.17, silica particles with k^{-1}=9.7nm, pre-factor=1554, and diameter=720nm). For colloidal self-assembling on chemically and physically patterned surfaces, it produces decent results (< 0.1 k_BT) at low density ($\rho_b\sigma^3$<0.3) across the different colloidal interaction types without gravity; while for colloidal self-assembly on patterned surface under gravity, it produces good results (< 0.3 k_BT) at $\rho_{total}\sigma^3$=0.1, k^{-1}=333nm, pre-factor=13728, and diameter=1.58μm, $(4/3)\pi a^3\Delta\rho g$=0.35 $k_BT/\mu m$. For colloidal self-assembling monolayer on physically patterned surface, it produces decent results (< 0.1 k_BT) from low to medium densities ($\rho_b\sigma^2$ <0.5) for hard surface and ($\rho_b\sigma^2$ <0.1) for certain external potential strength (< -4k_BT) at different particle-particle potential and surface energetic landscapes.

2. THEORY

2.1 Synopsis

In this section, we first briefly review the applications of integral equation theory for classical fluids, which involves the radial distribution function $g(\boldsymbol{r})$ and its relationship with thermodynamics, the Ornstein- Zernike (OZ) equation, and bridge functions to close integral equation theory. Next, we briefly review the different free energy approximations for density functional theory, namely weighted density approximations, position independent weighted density approximations, fundamental measure approach, perturbative density function theory, and closured based density functional theory. Finally, we demonstrate the forward and inverse analysis by closured based density functional theory.

2.2 Integral Equation Theory

2.2.1 Radial distribution function and its relationship with thermodynamics

In this section, some basic distribution functions and their relationships to thermodynamics are briefly reviewed. For more details, please see the book on statistical mechanics of fluids by Hansen and McDonald.[10]

The function $g(\boldsymbol{r})$ is known as the radial distribution function and it represents the relative probability of finding another particle at the distance $\boldsymbol{r}$ away from the particle at origin. For a translationally invariant and isotropic fluid, the vector $\boldsymbol{r}$ can be simplified to scalar r. This function may be used to calculate macroscopic thermodynamic properties. For example, the excess internal energy per particle is given by:

$$U^{ex} / N = 2\pi\rho_b \int g(r)u(r)r^2 dr \tag{2.1}$$

where ρ_b is the bulk density, $u(r)$ is particle-particle pair potential and N is the number of particles. The equation of state (EOS) can be written as:

$$\frac{\beta P}{\rho_b} = 1 - \frac{2}{3}\beta\pi\rho_b \int g(r) r^2 \left(r \frac{d}{dr} u(r) \right) dr. \tag{2.2}$$

Eq. (2.2) is well known as the 'virial' route to the EOS since the Pressure P is determined in terms of an average of the virial. Also, g(r) can be related to the isothermal compressibility by thermodynamic fluctuation theory:

$$\rho_b k_B T \kappa_T = 1 + \rho_b \int \{g(r) - 1\} dr \tag{2.3}$$

where κ_T is the isothermal compressibility of the system, k_B is the Boltzmann constant and T the absolute temperature. $\beta P/\rho_b$ can be determined by the isothermal compressibility also:

$$\kappa_T = -\frac{1}{V}\left(\frac{\partial V}{\partial P}\right)_T = \left[\rho_b \left(\frac{\partial P}{\partial \rho_b} \right)_T \right]^{-1} \tag{2.4}$$

where V is the volume of system. Combing Eq. (2.3) and (2.4), P can be calculated through the integration with respect with density along an isothermal path. Notation $(\beta P/\rho_b)_C$ was used to indicate the "compressibility" EOS so obtained.

Osmotic pressure (Π) is the pressure difference between a colloidal fluid and the particle-free liquid medium when they are separated by a membrane that is permeable to the liquid but not the particles. The osmotic pressure can also be related to interparticle interaction potential (as mediated by the liquid) and $g(r)$ by the virial equation of state:[64]

$$\Pi = \rho_b k_B T - \frac{2}{3}\pi\rho_b^{\,2} \int g(r) r^2 \left(r \frac{d}{dr} u(r) \right) dr \tag{2.5}$$

The reduced osmotic compressibility is:

$$\chi_T = \left(\frac{k_B T}{\frac{4}{3}\pi a^3} \right) \left(\frac{\partial \Pi}{\partial \eta} \right)_T^{-1} \tag{2.6}$$

where a is colloidal radius, $\eta = \frac{\pi}{6}\rho_b\sigma^3$ is the packing fraction of the system. Integrating Eq. (2.6) one can obtain the osmotic pressure out of compressibility.

For both the virial and compressibility routes, the pressure P *or* Π can be related to $g(r)$. If $g(r)$ is "exact", then the virial and the compressibility routes should give same value so that this is called *thermodynamic consistency*. When $g(r)$ is only an approximate, the two routes will give different values for the pressure at a given density and temperature; this is referred to as thermodynamic inconsistency. In Section 2.2.3.1 and 2.2.3.5 we will discusses more details about thermodynamic consistency for the PY and RY bridge function approximations respectively.

2.2.2 Ornstein- Zernike (OZ) equation

The Ornstein- Zernike (OZ) equation is an integral equation that defines the direct correlation function; it describes the how to calculate the correlation between two molecules (or particle) with its mainly application to fluids. The total correlation function is defined by:

$$h(r) = g(r) - 1 \tag{2.7}$$

Thus as $g(r) \to 1,\ h(r) \to 0.$ A new function direction correlation function $c(r)$ is defined from $h(r)$:

$$h(r) - c(r) = \rho_b \int d\mathbf{r}' c(|\mathbf{r}'|) h(|\mathbf{r} - \mathbf{r}'|) \tag{2.8}$$

Eq. (2.8) is the well-known Ornstein- Zernike equation[10]. By Fourier transform Eq.(2.8), one immediately obtains:

$$h(k) = \frac{c(k)}{1 - \rho_b c(k)} \tag{2.9}$$

where $h(k)$ and $c(k)$ are Fourier transform of $h(r)$ and $c(r)$. The OZ equation shows that the description of $h(r)$ can be considered as the sum of two different contributions: the first one, $c(r)$, arises from direct interaction between two particles and the rest amounting

to indirect correlations mediated by same $c(r)$ through many-body integrals over other particles. The indirect part can be expressed by a function called indirect correlation function $\gamma(r) = h(r) - c(r)$.

Besides the OZ equation, another equation describing the relationship for $h(r)$ and $c(r)$ to the particle-particle potential can be obtained from the cluster expansion of $g(r)$[10]. It can be shown as:

$$g(r) = \exp\{-\beta u(r) + \gamma(r) + B(r)\} \tag{2.10}$$

where $B(r)$ can be shown to be the sum of an infinite number of terms graphically represented by the so-called 'bridge diagrams'.[10]

2.2.3 Bridge function approximations

As we described in the last section, $B(r)$ is need to solve Eq. (2.10). However, the exact bridge function is not known to any system. A number of works has been done to get an estimate for $B(r)$ for different fluid models. In the following subsection, we will illustrate some commonly used bridge function approximation for fluids.

2.2.3.1 Percus-Yevick (PY) approximation

The Percus-Yevick (PY) approximation[65] for a general particle-particle potential $u(r)$ consists in assuming that:

$$c(r) = g(r)\left[1 - e^{\beta u(r)}\right] \tag{2.11}$$

The solution of Eq. (2.8) and (2.11) can in general be obtained through numerical methods, as for instance iterative procedures (numerical method are described in Section 3.2). For the hard sphere fluid the solution can be obtained analytically as the following equation by Wertheim:[66]

$$-c(r) = \lambda_1 + 6\eta\lambda_2 r + 0.5\eta\lambda_1 r^3 \tag{2.12}$$

$$\lambda_1 = \frac{(1+2\eta)^2}{(1-\eta)^4}$$

$$\lambda_2 = -\frac{(1+0.5\eta)^2}{(1-\eta)^4}$$

where $\eta = \frac{\pi}{6}\rho_b\sigma^3$ is the packing fraction of the system. The virial equation of state by Eq. (2.2) can then be obtained in an explicit analytic form:

$$\left(\frac{\beta P}{\rho_b}\right)_v = \frac{1+2\eta+3\eta^2}{(1-\eta)^2}. \tag{2.13}$$

The compressibility EOS can also be obtained in an explicit form:

$$\left(\frac{\beta P}{\rho_b}\right)_c = \frac{1+\eta+\eta^2}{(1-\eta)^3}, \tag{2.14}$$

Eqs. (2.13) and (2.14) show that PY is thermodynamically inconsistent; however, Eq. (2.13) and (2.14) each yield the exact second and third virial coefficients of hard spheres[10].

The solution of Eq. (2.8), (2.10), and (2.11) can give us the relationship between $B[\gamma(\mathbf{r})]$ and $\gamma(\mathbf{r})$ as following:

$$B[\gamma(\mathbf{r})] = \ln(1+\gamma(\mathbf{r})) - \gamma(\mathbf{r}) \tag{2.15}$$

The PY has been extensively applied to many other one-component model fluids such as the square well fluid, the Lennard-Jones fluid, adhesive hard sphere fluid and so on. It is well known that PY works for short range potential.

2.2.3.2 Hypernetted-chain (HNC) approximation

In HNC approximation, bridge function is omitted, thus:

$$B[\gamma(\mathbf{r})] = 0 \tag{2.16}$$

As PY approximation, HNC exactly predicts the second and third virial coefficients.[10] The HNC equation has extensively been applied to both simple and charged fluids and it is well known that HNC is better than PY for long range potential.

2.2.3.3 Verlet Modified (VM) approximation

A semi-phenomenological equation for the $g(\mathbf{r})$ was proposed by Verlet[67] for the case of hard spheres, on the basis of the following functional assumption for the bridge function:

$$B[\gamma(\mathbf{r})] = -\gamma(\mathbf{r})^2 / 2(1+\alpha\gamma(\mathbf{r})) \tag{2.17}$$

α is usually taken as 0.8. This approximation yields excellent results for both thermodynamic and structural properties VM has been used in a number of studies such as hard sphere fluids,[68] Lennard-Jones fluids,[69] and penetrable sphere fluids[70] with considerable success .

2.2.3.4 *Martynov and Sarkisov* (*MS*) *approximation*

Another approximation, which has been proposed by Martynov and Sarkisov[71] set:

$$B[\gamma(\mathbf{r})] = (1+2\gamma(\mathbf{r}))^{0.5} - \gamma(\mathbf{r}) - 1 \tag{2.18}$$

while for $g(r)$ is the following:

$$g(r) = \exp\{-\beta u(r) + [1+2\gamma(r)]^{0.5} - 1\} \tag{2.19}$$

There is no adjustable parameter in MS approximation and it has originally been applied to the hard sphere system in the high density.

2.2.3.5 Rogers-Young (RY) approximation

These basic observations have suggested (Rogers and Young[72]) to adopt a closure which allows to continuously interpolate between the PY and HNC:

$$g(r) = \exp[-\beta u(r)]\left[1 + \frac{\exp[\gamma(r) f(r)] - 1}{f(r)}\right] \tag{2.20}$$

$$g(r) = \exp[-\beta u(r)]\left[1 + \gamma(r)\right] \quad \text{(PY)} \tag{2.21}$$

$$g(r) = \exp\left[-\beta u(r)\right]\exp\left[\gamma(r)\right] \quad \text{(HNC)} \tag{2.22}$$

When r=0, $f(r)$=0. Eq. (2.20) reduces to Eq. (2.21); as r increase, $f(r)$ approach 1, Eq. (2.20) reduces to Eq. (2.22).The mixing function $f(r) = 1 - \exp(-\alpha r)$ and α is an adjustable parameter determined by thermodynamic consistency. Consistency is obtained when the bulk modulus calculated from the virial equation B_p is equal to that calculated from the compressibility equation B_c. The common approach is to calculate a value of α that satisfies this consistency criterion at a thermodynamic state point where the particle-particle correlations are particularly strong, such as the freezing point, and then use that value of α at other state points.[72] In this work we found that an alternative to enforcing B_p=B_c is to minimize the absolute error in $g(r)$ calculated from OZ equation with the RY closure (as compared to the "exact" result from MC simulation at the same state point); those two methods gave us the same α value within 10 percent. Once the value of α is fixed, a numerical relation between $B[\gamma(r)]$ and γ(r) may be obtained by solving the OZ equation and creating a parametric plot (see Fig. 4.1) using Eq. (2.10).[49]

The RY theory has been applied with satisfactory results to hard spheres, inverse-power potentials, [72] hard sphere+ attractive Yukawa tail,[49] DLVO screened electrostatic repulsive[49], van der Waals (vdW)[73] and Asakura-Oosawa (AO) depletion attraction.[73]

2.2.3.6 Zhou-Hong-Zhang (ZHZ) approximation

In 2003, Zhou, Hong and Zhang gave this approximation as following:

$$B[\gamma(\mathbf{r})] = -0.5\gamma(\mathbf{r})^2 \exp(-\alpha\gamma(\mathbf{r})) \tag{2.23}$$

The ZHZ closure is somewhat unique in that there is an adjustable parameter α directly in the $B[\gamma]$ expression. Zhou, Hong, and Zhang suggest that α should be determined by thermodynamic consistency,[74] which requires equality between the pressures calculated by the virial and compressibility routes. For hard spheres, they found that α is a somewhat strongly varying function of the volume fraction.[74] Interestingly, this contradicts the usual notion of developing OZ closures where B is a

universal function of γ, independent of potential type or thermodynamic state. In this paper, we calculated the α at 10 different densities enforcing bulk modulus calculated from the virial equation B_p is equal to that calculated from the compressibility equation B_c. Then standard interpolation procedure was applied to obtain the α at the right bulk density described in theory section bulk density choice in forward and inverse DFT equations part. This closure approximation has been successfully applied to hard sphere, hard sphere + attractive Yukawa tail.[74]

2.3 Density Functional Theory

In this section, formalism of DFT and its free energy approximations are briefly reviewed. For more details, please see the book on fundamentals of inhomogeneous fluids Chapter 3 density functionals in the theory of nonuniform fluids by R. Evans.[42]

2.3.1 Formalism

In DFT, the grand potential $\Omega[\rho]$of a many-particle system is a function of its single particle density distribution $\rho(\mathbf{r})$ and can be written as:

$$\Omega[\rho] = F[\rho] + \int dr \rho(\mathbf{r})\left[\varphi_{ext}(\mathbf{r}) - \mu\right] \tag{2.24}$$

where $\varphi_{ext}(\mathbf{r})$ is the external potential and μ the chemical potential of the inhomogeneous fluid. The intrinsic Helmholtz free energy $F[\rho]$ is a sum of two contributions, the ideal free energy $F_{id}[\rho]$ and excess free energy $F_{ex}[\rho]$, which is nonideal due to intermolecular interactions and it is only known approximately . The functional form of $F_{id}[\rho]$ is exactly known:

$$F_{id}[\rho(r)] = k_B T \int dr \rho(r)\{\ln[\rho(r)\Lambda^3] - 1 \tag{2.25}$$

where Λ is the thermal de Broglie wavelength. From the variational principle:

$$\frac{\delta\Omega[\rho(r)]}{\delta\rho(r)} = 0 \tag{2.26}$$

the equilibrium density of inhomogeneous fluids under a external potential $\varphi_{ext}(\mathbf{r})$ can be determined. Also direct correlation function can be related to excess free energy by:

$$c^{(1)}(\mathbf{r};[\rho]) = -\frac{\delta(\beta F_{ex}[\rho])}{\delta\rho(\mathbf{r})} \tag{2.27}$$

$$c^{(2)}(\mathbf{r}_1,\mathbf{r}_2;[\rho]) = \frac{\delta c^{(1)}(\mathbf{r}_1;[\rho])}{\delta\rho(\mathbf{r}_2)} = -\frac{\delta^2(\beta F_{ex}[\rho])}{\delta\rho(\mathbf{r}_2)\delta\rho(\mathbf{r}_1)} \tag{2.28}$$

With $C^{(1)}(\boldsymbol{r};[\rho])$ is the first order direct correlation function of the nonuniform fluid, $C^{(2)}(\boldsymbol{r_1},\boldsymbol{r_2};[\rho])$ the second order direction correlation function. Combining Eq. (2.24) to Eq. (2.27), one can obtain the following equation:

$$\Lambda^3\rho(\mathbf{r}) = \exp\left[\beta\mu - \beta\varphi_{ext}(\mathbf{r}) + C^{(1)}(\mathbf{r};[\rho])\right] \tag{2.29}$$

The final form of DFT can be obtained by equating the chemical potential of inhomogeneous fluid to that of the bulk fluid (where $\varphi_{ext}(\boldsymbol{r})=0$, $\rho(\boldsymbol{r})=\rho_b$), given by:

$$\rho(\mathbf{r}) = \rho_b \exp\left[-\beta\varphi_{ext}(\mathbf{r}) + C^{(1)}(\mathbf{r};[\rho]) - C_0^{(1)}(\rho_b)\right] \tag{2.30}$$

where $C_0^{(1)}(\rho_b)$ is the first order direct correlation function the corresponding quantity in the bulk fluid. The essence of the forward DFT problem is to develop an estimate for $C^{(1)}(\boldsymbol{r};[\rho])$ based on the imposed $\varphi_{ext}(\mathbf{r})$ and ρ_b, so that $\rho(\mathbf{r})$ may be obtained via Eq. (2.30).

2.3.2 Approximation for free energy functions

As in formalism section, the key issue for DFT is the free energy functional $F[\rho]$, or more precisely the excess free energy function $F_{ex}[\rho]$. Since there is not exact functional form available, thus one needs to make an explicit approximation for the function $F_{ex}[\rho]$ for a particular physical problem. After the approximation, the equilibrium $\rho(\boldsymbol{r})$ and grand potential Ω can be determined, via Eq. (2.24) and (2.26), for specific T, μ, and $\varphi_{ext}(\mathbf{r})$. However, the reliability and accuracy of the results are largely depend on the way approximation was constructed for particular model or system; some

models might need very crude approximations, while for some models or phenomena such as phase transitions[42] even very sophisticated approximations will not performs as well as molecular simulation.

In general, most of approximations fall into two categories: (1) perturbative DFT (PDFT), using Taylor expansion to the reference states (the corresponding bulk phase) and (2) non-perturbative methods which mainly use a weighted density function. In the following section, we briefly reviewed various approximations for $F_{ex}[\rho]$ that have been developed for simple fluids.

2.3.2.1 Weighted density approximations

Weighted density approximations (WDA) are modifications of local density approximation (LDA) for inhomogeneous system, where the free energy at some position $\boldsymbol{r}$ at density $\rho(\boldsymbol{r})$ can be valued by the free energy of homogeneous system. WDA uses the coarse-graining procedure to avoid the LDA's weakness for very strongly inhomogeneous systems where the local density may exceed that for close packing. A smoothed density $\overline{\rho}(r)$ is constructed as an average density profile $\rho(\boldsymbol{r})$ so that the highly oscillatory density profile of strong inhomogeneous system was smoothed out by coarse-grained $\overline{\rho}(r)$, which remedy the LDA's break down issue. The excess free energy functional forms follow that of LDA by:

$$F_{ex}[\rho] = \int d\mathbf{r}\rho(\mathbf{r})\psi_{ex}\left(\overline{\rho}(\mathbf{r})\right) \tag{2.31}$$

where $\psi_{ex}(\mathbf{r})$ is the excess, over ideal, free energy per atom. The different version of WDA correspond to different recipes for $\overline{\rho}(\mathbf{r})$.

2.3.2.1.1 Nordholm et al.

The recipe by Nordholm and co-workers[75] is almost the earliest one, for which:

$$\overline{\rho}(\mathbf{r}) = \int d\mathbf{r}' w_0(|\mathbf{r}-\mathbf{r}'|)\rho(\mathbf{r}') \tag{2.32}$$

$$w_0(\mathbf{r}) = \frac{3}{4\pi\sigma^3}\theta(\sigma - \mathbf{r})$$

where θ is the Heaviside step function, σ is atom diameter. The application of this recipe to hard sphere near hard wall gave oscillatory profiles but was not as good as molecular simulation.

2.3.2.1.2 Tarazona

In 1985, Tarazona[76] developed a more sophisticated version of WDA. The weighted function is given by:

$$\overline{\rho}(\mathbf{r}) = \int d\mathbf{r}' w\left(|\mathbf{r} - \mathbf{r}'|; \overline{\rho}(\mathbf{r})\right)\rho(\mathbf{r}') \tag{2.33}$$

$$w(\mathbf{r};\rho) = w_0(\mathbf{r}) + w_1(\mathbf{r})\rho + w_2(\mathbf{r})\rho^2$$

where the explicit formulas for w_0 and w_1 are given by Tarazona[77], the w_2 is obtained from a fit to the PY result. Tarazona showed a much better results than that of Nordholm et al. for density profile of hard sphere near hard wall, surface tension and bulk hard sphere freezing. After Tarazona's original work, there have been a number of applications of this WDA such as wetting transition,[78] capillary,[77] prewetting,[79] freezing,[77] adsorption.[80]

2.3.2.1.2 *Cutin-Ascroft*

Curtin and Ashcroft[81] proposed a version of WDA which is better than Tarazona's for mixture and pure fluid but with increased computational complexity. They used the same excess free-energy functional and the weighted density as Tarazona which are Eq. (2.31) and (2.32); but with more complex weighting function *w,* which can be determined by solving following equation:

$$-\beta^{-1}c_k^{(2)}(\rho) = 2\psi'_{ex}(\rho)w_k(\rho) + \rho\frac{\partial}{\partial\rho}\left[\psi'_{ex}(\rho)w_k{}^2(\rho)\right] \tag{2.34}$$

where $c_k^{(2)}(\rho)$ is the Fourier transform of $c^{(2)}(\mathbf{r};\rho)$, the prime represents differentiation with respect to density ρ. For hard sphere fluid, $c_k^{(2)}(\rho)$ and $\psi_{ex}(\rho)$ are given analytically by PY approximation and $w(r;\rho)$ can be numerically solved.

WDA of Cutin and Ashcorft was extensively applied with high success to hard sphere freezing[81],surface free energy of crystal-liquid interface[82,83], hard sphere near hard wall,[84] mixture,[85] Lennard-Jones fluids,[86] colloidal dispersion.[87]

2.3.2.2 Position independent weighted density approximations

In this section, we reviewed another class of WDA, which is simpler than last section's WDA and has successful applications in the study of freezing, liquid – solid interface.

2.3.2.2.1 MWDA

Denton and Ashcroft[88] proposed a modified WDA (MWDA) simplified the excess free energy to express it by per atom:

$$\frac{F_{ex}[\rho]}{N} = \psi_{ex}(\hat{\rho}) \tag{2.35}$$

where, the weighted density is given:

$$\hat{\rho} = \frac{1}{N}\int dr\rho(\mathbf{r})\int d\mathbf{r}' w(|\mathbf{r}-\mathbf{r}'|;\hat{\rho}) \tag{2.36}$$

with $N = \int d\mathbf{r}\rho(\mathbf{r})$. The new weighted function w can be achieved by:

$$w(r;\rho) = -\frac{1}{2\psi'_{ex}(\rho)}\left[\beta^{-1}c^{(2)}(\rho;r) + \frac{1}{V}\rho\psi''_{ex}(\rho)\right] \tag{2.37}$$

where V is the total volume of the fluid. The weighted function can be obtained immediately through Eq. (2.37), while WDA of Curtin and Ashcroft need to solve differential equation (2.34).

The MWDA's hard sphere freezing results were very close to Curtin and Ashcroft, but it can not describe the growth of wetting films or surface phase transitions. The MWDA has also been extended to mixtures,[85] surface melting at a crystal-gas interface,[89] and extensive investigation freezing of bulk fluid with soft repulsive potentials.[84]

2.3.2.2.1 PWDA

Marr and Gast[90] approached the interface by planar WDA (PWDA) following the spirit of MWDA. The excess free energy was given:

$$F_{ex}[\rho] = \int dz\, \hat{\rho}(z)\psi_{ex}(z) \tag{2.38}$$

$$\hat{\rho}(z) = \frac{1}{A}\int dxdy\,\rho(\mathbf{r})$$

They approximated free energy with that of a homogeneous fluid evaluated at the planar weighted density $\bar{\rho}(z)$:

$$F_{ex}^{PWDA}[\rho] = \int dr\, \hat{\rho}(z)\psi_0(\bar{\rho}(z)) \tag{2.39}$$

$$\bar{\rho}(z) = \frac{\int dxdy\,\rho(\mathbf{r})\int d\mathbf{r}'\,\rho(\mathbf{r}')w(\mathbf{r}-\mathbf{r}';\bar{\rho}(z))}{\int dxdy\,\rho(\mathbf{r})}$$

In Fourier space, the weighting function should follow:

$$-\beta c_0(k;\rho_0) = 2\psi'_0\, w(k;\rho_0) + \delta_{k_{\|},0}\rho_0 \frac{\partial}{\partial\rho_0}\left[\psi'_0\, w^2(k;\rho_0)\right] \tag{2.40}$$

when $k_{||}$=0, it reduce to WDA of Curtin and Aschsoft, when k|| is nonzero, it reduced to MWDA weighting function.

Marr and Gast have successfully applied the PWDA to solid-liquid interface of hard sphere, Lennard-Jones system[90], adhesive sphere[91], solid-liquid interfacial properties.[92]

2.3.2.3 Fundamental measure approach

Rosenfeld[93] introduced a very different approach (fundamental measure approach (FMA)) in several features. First this is geometry-based DFT and is made from mathematic and physical foundations instead of empirical approximation as others.[11] Second it does not need use hard sphere as reference as other WDA. It also provides an exact dimension crossover,[11] which make it very convenient to extend other dimensions. The weighted function was given by:

$$\beta F_{ex}[\{\rho_i(\mathbf{r})\}] = \int d\mathbf{r}\Phi(\{n_\alpha(\mathbf{r})\}) \tag{2.41}$$

where Φ is a function of linear averages:

$$n_\alpha(\mathbf{r}) = \sum_{i=1}^{v} \int dr' \rho_i(\mathbf{r}')\varpi_i^{(\alpha)}(\mathbf{r}-\mathbf{r}') \tag{2.42}$$

and $\varpi_i^{(\alpha)}(r)$, with α=1,2,...,*m*, are unknown but density-independent weight functions given as following:

$$\begin{aligned} \varpi^{(3)}(r) &= \Theta(|r|-R) \\ \varpi^{(2)}(r) &= \delta(|r|-R) \\ \varpi^{(1)}(r) &= \frac{\varpi^{(2)}(r)}{4\pi R} \\ \varpi^{(0)}(r) &= \frac{\varpi^{(2)}(r)}{4\pi R^2} \end{aligned} \tag{2.43}$$

FMA is originally developed for hard sphere mixtures,[93] then been extended to penetrable spheres,[44] colloidal-polymer mixtures,[44] fluids in porous media,[44] hard sphere near hard wall under gravity.[46] fluid and solid phase, and even non-spherical system such as liquid crystal.[11]

2.3.2.4 Perturbative density function theory

The simplest approximation in DFT is, however, the perturbative approach, based on a functional Taylor expansion of $C^{(1)}(\boldsymbol{r};[\rho])$ around $C_0^{(1)}(\rho_b)$ of bulk density ρ_b:

$$C^{(1)}(\mathbf{r};[\rho]) = C_0^{(1)}(\rho_b) + \int d\mathbf{r}_1(\rho(\mathbf{r}_1) - \rho_b)C_0^{(2)}(\mathbf{r},\mathbf{r}_1;\rho_b) + \sum_3^{\infty} \frac{1}{(n-1)!}\int d\mathbf{r}_1 \int d\mathbf{r}_2 \cdots \int d\mathbf{r}_{n-1} \times \prod_{m=1}^{n-1}[\rho(r_m) - \rho_b] \times C_0^{(n)}(r, r_1, \cdots r_{n-1};\rho_b) \tag{2.44}$$

where $C_0^{(n)}(\mathbf{r},\mathbf{r}_1,\cdots\mathbf{r}_{n-1};\rho_b)$ is nth order direct correlation function of homogeneous system of bulk density ρ_b. By using Percus identity[94] for the special case of an external field generated by a single particle of the fluid species placed at the origin:

$$\rho(\mathbf{r}) = \rho_b g(r) \tag{2.45}$$

equation (2.44) changes to the following form:

$$C^{(1)}(\mathbf{r};[\rho]) = C_0^{(1)}(\rho_b) + \int d\mathbf{r}_1(\rho(\mathbf{r}_1) - \rho_b)C_0^{(2)}(\mathbf{r},\mathbf{r}_1;\rho_b) + \sum_{n=3}^{\infty} \frac{1}{(n-1)!}\int d\mathbf{r}_1 \int d\mathbf{r}_2 \cdots \int d\mathbf{r}_{n-1} \times \prod_{m=1}^{n-1}[\rho(\mathbf{r}_m) - \rho_b] \times C_0^{(n)}(\mathbf{r},\mathbf{r}_1,\cdots\mathbf{r}_{n-1};\rho_b) \tag{2.46}$$

Perturbative approaches usually focus on truncating this expansion at some reasonable order and evaluating the remaining direct correlation functions,[95] and replace the truncated Eq. (2.46) into Eq. (2.30) to yield the following equation for the density profile:

$$\rho(\mathbf{r}) = \rho_b \exp\left\{-\beta\varphi_{ext}(\mathbf{r}) + \int d\mathbf{r}_1(\rho(\mathbf{r}_1) - \rho_b)C_0^{(2)}(\mathbf{r},\mathbf{r}_1;\rho_b)\right\} \tag{2.47}$$

This equation, along with closely related approximations based on HNC closures of the wall-particle OZ equation, has been used in many studies of the density profile of liquids and gases near wall. This theory is quite successful at describing the oscillatory profiles of hard spheres near hard wall; it is less successful when the fluid possesses an attractive, as well as a repulsive, component in the interatomic potential. One severe drawback of this theory is its inability to account for the presence of macroscopically thick wetting films at a wall-fluid interface or for critical adsorption.

2.3.2.5 Closured based density functional theory

Recently Zhou and Ruckenstein[45](ZR) invoked the universality of the Helmholtz free energy functional for systems with pairwise-additive interactions to show that Eq. (2.46) may be written much more concisely as:

$$C^{(1)}(\mathbf{r};[\rho]) = C_0^{(1)}(\rho_b) + \int d\mathbf{r}_1(\rho(\mathbf{r}_1) - \rho_b)C_0^{(2)}(\mathbf{r},\mathbf{r}_1;\rho_b) + B\left[\vartheta(\mathbf{r})\right] \qquad (2.48)$$

where the $n \geq 3$ terms are identified as the bridge function B of the fluid. (We note that the bridge function is the sum of the "elementary diagrams" in the integral equation theory literature.[10]) Here B is written as a functional of a yet-to-be-chosen structural correlation function $\vartheta(\mathbf{r})$; the functional relationship represents a closure in the sense of Ornstein-Zernike (OZ) integral equation theory. ZR[45] point out that a natural choice of $\vartheta(\mathbf{r})$ for confined fluids is the inhomogeneous analogue of the bulk indirect correlation function, $\gamma(\mathbf{r}) = \int d\mathbf{r}_1(\rho(\mathbf{r}_1) - \rho_b)C_0^{(2)}(\mathbf{r},\mathbf{r}_1;\rho_b)$. With these choices, Eq. (2.30) becomes:

$$\rho(\mathbf{r}) = \rho_b \exp\begin{Bmatrix} -\beta\varphi_{ext}(\mathbf{r}) + \int d\mathbf{r}_1(\rho(\mathbf{r}_1) - \rho_b)C_0^{(2)}(\mathbf{r},\mathbf{r}_1;\rho_b) \\ + B\left[\int d\mathbf{r}_1(\rho(\mathbf{r}_1) - \rho_b)C_0^{(2)}(\mathbf{r},\mathbf{r}_1;\rho_b)\right] \end{Bmatrix} \qquad (2.49)$$

Equation (2.49) is a novel formulation of DFT that predicts the density profile based purely on the bulk second-order direct correlation function and the choice of a closure relationship for the bridge function. Since the theory is perturbative, it requires no density weighting; unlike previous perturbative approaches, painstaking evaluation of higher order correlation functions is not needed. The accuracy of the theory has been tested in several cases and found to be similar to that of the best previous DFT formulations. Zhou and Ruckenstein[45] initially examined single-component hard sphere fluids confined to several different geometries and with different surface potentials. The theory has since been tested on different model fluids (*e.g.* Lennard-Jones,[96,97] Yukawa,[49] and penetrable spheres[98]), mixtures,[96,99] and polymers[100,101] with a high degree of success.

2.3.3 Forward and inverse analysis

For the forward analysis, we can use the Eq. (2.49) to predict the density using the particle-particle potential $u(\mathbf{r})$ and external particle-surface potential $\varphi_{ext}(\mathbf{r})$ as input.

For the inverse, we assume that we can measure the density profile $\rho(\mathbf{r})$ of a dense fluid (e.g. a colloid) in an inhomogeneous environment (e.g. near a surface), and we would like to use this information to predict the potential energy of a single colloidal particle at different locations in that environment, $\varphi_{ext}(\mathbf{r})$. Algebraic inversion of Eq. (2.49) provides an equation for this purpose:

$$\beta\varphi_{ext}(\mathbf{r}) = -\ln\left[\frac{\rho(\mathbf{r})}{\rho_b}\right] + \int d\mathbf{r}_1(\rho(\mathbf{r}_1)-\rho_b)C_0^{(2)}(\mathbf{r},\mathbf{r}_1;\rho_b) + B\left[\int d\mathbf{r}_1(\rho(\mathbf{r}_1)-\rho_b)C_0^{(2)}(\mathbf{r},\mathbf{r}_1;\rho_b)\right] \tag{2.50}$$

Every quantity on the right hand side of Eq. (2.50) may be considered an input. We assume that the density profile and bulk density will be measured in the experiment. We also assume that the bulk second order direct correlation function $C_0^{(2)}(\mathbf{r},\mathbf{r}_1;\rho_b)$ may be obtained "off-line" from a separate consideration of the bulk fluid. For example, a video microscopy experiment could be done to directly measure the radial distribution function $g(\mathbf{r})$, and $C_0^{(2)}(\mathbf{r},\mathbf{r}_1;\rho_b)$ would then be accessible as the only unknown in the bulk OZ equation. Alternatively, the pairwise potential of mean force between particles could be obtained from a combination of total internal reflectance microscopy and first principles calculation,[102,103] and the bulk OZ equation could be solved in an appropriate closure to yield $C_0^{(2)}(\mathbf{r},\mathbf{r}_1;\rho_b)$. In either case, the unknown $\varphi_{ext}(\mathbf{r})$ may be obtained by the straightforward numerical operations shown in Eq. (2.50).

An analogous inverse problem arises for homogeneous fluids, and noting its parallel with the current problem is worthwhile. For homogeneous fluids of particles (either atomistic or colloidal), one would often like to deduce the pairwise particle-particle interaction potential from the experimentally determined radial distribution function $g(r)$.[63] If we consider the inhomogenous potential $\varphi_{ext}(\mathbf{r})$ to be caused by a

single fluid particle located at the origin so that $\rho(\mathbf{r}) = \rho_b g(r)$, then Eq. (2.50) reduces exactly to the diagrammatic modified hypernetted-chain (MHNC) formulation of the fluid structure inversion problem presented by Rosenfeld and Kahl.[63] In fact, ZR[45] appeal to the concept of a single-particle inhomogeneity to derive Eq.(2.49).

The inversion of ZR's theory embodied in Eq. (2.50) is well-suited to our needs. We expect that the necessary bulk fluid direct correlation functions will be easily obtainable from the same type of imaging techniques that produce the density profiles. Since the mathematical formulation is analogous to that for structure-potential inversion problems in homogeneous fluids, we should be able to take advantage of techniques from that literature to improve the accuracy.[104,105]

3. NUMERICAL SOLUTIONS OF INTEGRAL AND DENSITY FUNCTIONAL EQUATIONS

3.1 Synposis

In this section, we first briefly review the numerical algorithm for integral equation theory by Lado[106,107] for two-dimensional system and Labik *et al.*[108] for three-dimensional system. Next, we describe six commonly used bridge functions. Then numerical integration method for DFT is given. Finally, we provided the Monte Carlo simulation details for the system we studied.

3.2 Numerical Algorithm for Integral Equation

To solve the OZ equation (2.8) numerically, we need the bridge function approximations described in Section 2.2.3.1 through 2.2.3.6. Rapid solutions of this convolution type integral equation are obtained from Fourier transform of Eq. (2.8), which is Eq. (2.9), by the method of Lado[109] and Labik.[108] In the following section, we briefly gave the algorithm for IET.

3.2.1 Two dimensional systems

Lado[106] introduced Mayer function and developed new functions to overcome numerical problem of $c(r)$ when particle-particle international potential $u(r)$ goes to infinity. The new functions were given:

$$h'(r) \equiv g(r)\exp\left[\beta u(r)\right] - 1 \tag{3.1}$$

$$P(r) \equiv h'(r) - \ln\left[1 + h'(r)\right] \tag{3.2}$$

$$c'(r) \equiv \left[1 + h'(r)\right] f(r) + \mu P(r) \tag{3.3}$$

where f is the Mayer function, $f = exp(-\beta u(r))-1$, μ is used to adjust between PY and HNC closure, when μ=0 Eq. (3.3) changes to PY and μ=1 leads to the PY and HNC equations, respectively. Fourier-Bessel transformation was applied to do the Fourier transform for 2D system, which was given:[107]

$$H(r_i) \equiv \frac{1}{\pi R^2} \sum_{j=1}^{N-1} h(k_j) \frac{J_0(k_j r_i)}{J_1^2(k_j R)} \tag{3.4}$$

$$h\left(k_j\right) \equiv \frac{4\pi}{K^2} \sum_{i=1}^{N-1} H\left(r_i\right) \frac{J_0\left(k_j r_i\right)}{J_1^2\left(K r_i\right)} \tag{3.5}$$

where $J_n(x)$ is Bessel function of first kind of order n with first N positive roots $\lambda_1, \lambda_2, \cdots, \lambda_N$ whre $J_n(x)=0$. While $r_i=\lambda_i/K$, $k_i=\lambda_i/R$ with $K=k_N$ and $R=r_N$ are range of r and k. After the Fourier transform, replace Eq. (3.3) into Eq. (2.9) then it becomes:

$$H'(k) = \mu p(k) + \left\{ \rho C'^2(k) / \left[1 - \rho C'(k)\right] \right\} \tag{3.6}$$

The solution must follow that the largest difference is less then 10^{-5} with definition by:

$$\max_j \left| r_j \left(H_j^{out} - H_j^{in} \right) \right| \le 10^{-5} \tag{3.7}$$

Then Broyles' mixing scheme was used to speed convergence:

$$H_{i+1}^{'in}(r) = (1-\alpha) H_i^{'out}(r) + \alpha H_{i-1}^{'out}(r) \tag{3.8}$$

where α ($0 \le \alpha < 1$) is the mixing parameter.

3.2.2 Three dimensional systems

In 1985, Labik et al.[108] proposed a new method for solving three-dimension OZ equation numerically. The combination between Newton-Raphson method and direct iterations was applied to speed up the convergence. Other advantages include low sensitivity to the initial estimate and a relative simple algorithm.[108]

Labik et al.[108] used the following Fourier transforms:

$$\Gamma_i = \frac{\Delta t}{2\pi^2} \sum_{j=1}^{N-1} \tilde{\Gamma}_j \sin\left(\frac{\pi}{N} ij \right) \tag{3.9}$$

$$\tilde{\Gamma}_j = 4\pi \Delta r \sum_{i=1}^{N-1} \Gamma_j \sin\left(\frac{\pi}{N} ij \right) \tag{3.10}$$

where Γ and $\tilde{\Gamma}$ is the function in real and Fourier spaces respectively. The details of computational algorithm is provided by Labik *et al.*[108] and Fig. 3.1 shows the flow chart based on their algorithm.

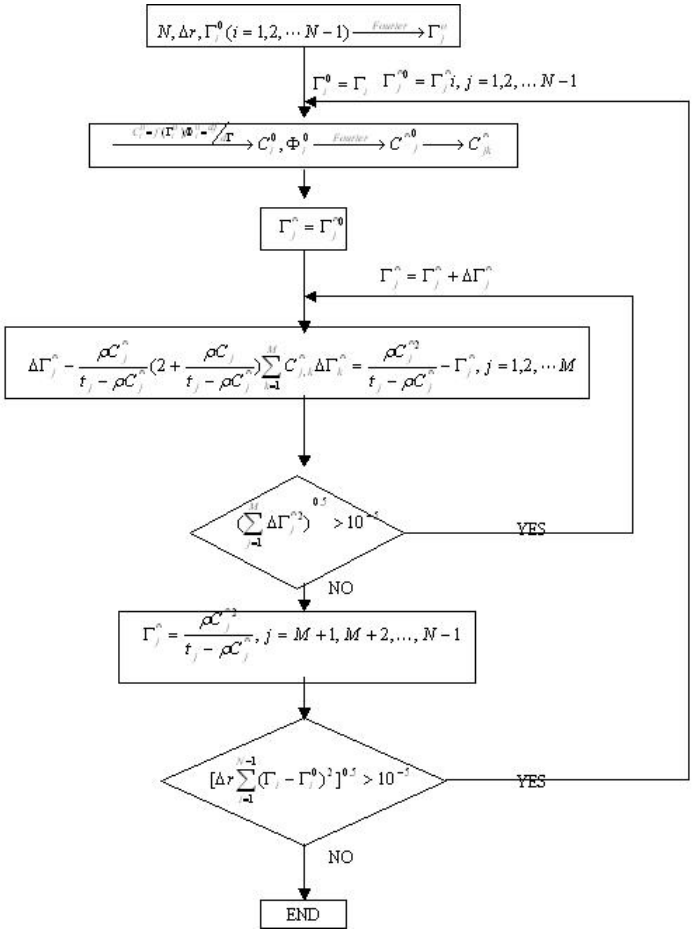

Fig. 3.1 Algorithm for solving 3D OZ equation by Labik *et al.*[108].

3.3 Bridge Function for Integral Equation

Although bridge function already been discussed in Section 2.2.3.1 through 2.2.3.6, we re-listed the bridge function together for convenience. Five of the closures employed in this dissertation have analytical expressions. They are

Percus-Yevick (PY)[65]: $$B\left[\gamma(\mathbf{r})\right] = \ln\left(1+\gamma(\mathbf{r})\right) - \gamma(\mathbf{r}) \tag{3.11}$$

Verlet-modified (VM)[67]: $$B[\gamma(\mathbf{r})] = -\gamma(\mathbf{r})^2 / 2(1+0.8\gamma(\mathbf{r})) \quad (3.12)$$

Hypernetted chain (HNC)[10]: $$B\left[\gamma(\mathbf{r})\right] = 0 \quad (3.13)$$

Martynov-Sarkisov (MS)[71]: $$B\left[\gamma(r)\right] = \left(1+2\gamma(r)\right)^{0.5} - \gamma(r) - 1 \quad (3.14)$$

Zhou-Hong-Zhang (ZHZ)[74]: $$B\left[\gamma(\mathbf{r})\right] = -0.5\gamma(\mathbf{r})^2 \exp\left(-\alpha\gamma(\mathbf{r})\right) \quad (3.15)$$

For α value in ZHZ closure calculation, please read Section 2.2.3.6. The other closure used in this dissertation has no analytical expression for $B[\gamma]$. The $g(r)$ from this closure is given by

Rogers-Young (RY)[72]: $$g(r) = \exp\left[-\beta u(r)\right]\left[1+\frac{\exp\left[\gamma(r)f(r)\right]-1}{f(r)}\right] \quad (3.16)$$

for α value in RY closure calculation, please read Section 2.2.3.5.

3.4 Multi-Dimensional Integration in Spherical and Polar Coordinates

For the forward and inverse analysis, i.e. Eq. (2.49) and (2.50), multi-dimensional integration is needed to calculate $\gamma(\mathbf{r}) = \int d\mathbf{r}_1(\rho(\mathbf{r}_1) - \rho_b)C_0^{(2)}(\mathbf{r},\mathbf{r}_1;\rho_b)$. 32 point Legendre-Gauss[110] method was applied for integration in this dissertation work. For colloidal particle interacting with homogeneous planer surface and patterned surface with or without gravity, spherical coordinate is used; while transform between Cartesian coordinate and spherical coordinate through the following equation:

$$\iiint_Q f(x,y,z)\,dzdydx = \iiint_Q f\left(\rho\cos\theta\sin\phi, \rho\sin\theta\sin\phi, \rho\cos\phi\right)\rho^2\sin\phi\, d\rho\, d\phi\, d\theta \quad (3.17)$$

where f is a continuous function on a solid Q. For monolayer colloidal self-assembly, polar coordinate is used for 2D DFT; the transform between Cartesian coordinate and polar coordinate through the following equation,

$$\iint_R f(x,y)\,dydx = \iint_R f\left(r\cos\theta, r\sin\theta\right)r\,dr\,d\theta \quad (3.18)$$

where f is a continuous function defined over a region R.

3.5 Canonical Monte Carlo Simulation

As we stated in the introduction section, MC has been extensively used for colloidal confined with different surface features and the results are treat as an "exact" for a given set of conditions. In this dissertation, we used Monte Carlo (MC) simulations to produce the density profiles to be used as the "experimental" input for inverse DFT. Canonical MC[8] was used to produce a set of appropriate equilibrium particle conFig.urations under different surface features for analysis.

For colloidal fluids at planar interfaces as in Section 4, we used a slit-pore type of geometry with two identical surfaces placed at z=0 and z=L, for convenience in the simulations. The separation L was always large enough so that the density decayed to the bulk value in a plateau region around the center of the pore, so we essentially had two replicates of a single-surface study in each simulation. Periodic boundary conditions were used in the x and y directions. The number of particles was chosen to produce the correct bulk density in each case and ranged from 300 to 13,500. The number of production MC cycles was at least 5 million in each case. The density profiles were obtained with bins of width from 0.005σ to 0.05σ in the z direction (σ is a measure of particle diameter).

We also used MC simulation of bulk fluids to test the radial distribution functions with that numerically obtained from the OZ equation (method described in Section 3.2). We studied bin widths ranging from $2.5\times10^{-4}\sigma$ to $0.05\ \sigma$ to ensure that our final results were not sensitive to the choice of bin width.

For colloidal sedimentation equilibrium as in Section 5, the starting number of particles were determined by experiment, and ranged from 500 to 3000 particles. The starting conFig.uration was a hexagonal lattice. The simulations were performed with an initial equilibration period consisting of 2 million particle steps. After equilibration, 5 million particle steps were used to generate statistically significant density distribution functions. All MC simulations employed a simulation box with confining walls on the top and bottom (normal to gravity) and periodic boundary conditions in the two

dimensions parallel to the confining walls. The step size normal to the wall was dynamically changed to give an equal number of unaccepted MC steps both normal and parallel to the wall, which ensured proper sampling of all thermodynamically accessible conFig.urations. The simulation box size was 5 μm x 5 μm (h) x 100 μm.

For colloidal self-assembly on chemically and physically patterned surfaces as in Section 6, we construct channel and patterned surface with proper potentials. Periodic boundary conditions were used in the x and y directions. The number of particles was chosen to produce the correct bulk density in each case and ranged from 120 to 3,000. The number of production MC cycles was at least 5 million in each case.

For monolayer colloidal self-assembly on patterned surfaces as in Section 7, 2D MC was applied with number of disks range from 40 to 800 with at least 50 million MC production cycles. Different surface model was constructed corresponding to different geometries as described in Section 7. The density profiles were obtained with bins of width 0.05σ.

4. DFT RESULTS FOR COLLOIDAL FLUIDS AT PLANAR INTERFACES

4.1 Synopsis

In this section, we use the DFT formulation of Zhou-Ruckenstein (ZR)[45] to study the colloidal particle interacting with homogeneous planar surface in both forward and inverse analysis (i.e. to make predictions of density profiles and particle-surface potentials for four common used colloidal potentials). We also implement MC simulation bulk fluids to compare the radial distribution functions with that numerically obtained from the OZ equation with different closures. Our results provide insight as to the quantitative limits on accuracy that one can expect from the DFT when comparing with, or interpreting, particle-scale density profiles using experimental data from techniques like CSLM.

4.2 Introduction

The structure of colloidal dispersions near surfaces is frequently important, particularly in applications such as coatings, where a given micro-structure is desired on a surface. Furthermore, colloidal structure under confinement is increasingly important to the assembly and function of nano- and micro-scale materials and devices. The structures of interfacial fluids, as well as crystalline, gel, and glassy states, have been studied for colloids with repulsive and attractive potentials.[111,112] CSLM has recently become an invaluable tool in these investigations that allows individual particles to be imaged within a three dimensional assembly in real space.[17] Several pioneering studies have been carried out to directly probe the structure and dynamics of colloidal crystals[18] and glasses[20] in bulk systems using CSLM.

DFT has been applied to a wide range of problems,[11,12] but in this section we are primarily concerned with inhomogeneous colloidal fluid phases. Several DFT-based studies on that particular topic have been carried out using hard sphere,[46,47] hard sphere + Yukawa tail,[48,49] DLVO,[49,113,114] soft repulsion,[43] and depletion[51] interaction potentials.

In addition to numerous applications to atomistic liquids, IET has been applied to bulk colloids fluids using direct Coulombic,[52-54] hard sphere + Yukawa tail[56,115], DLVO,[53,54] and depletion[57,58] interaction potentials and to confined colloids with hard sphere,[59] adhesive sphere,[60] hard sphere + Yukawa tail,[61] and DLVO[62] potentials.

In a previous paper,[116] we explored an inversion of DFT where we calculated the external potential field from a known density profile in an inhomogeneous fluid. The motivation was that CSLM and other imaging modalities can now provide such equilibrium density profiles on colloidal systems near interfaces, so one might employ that knowledge to measure the interaction potential of a single particle with the surface. The closure-based DFT of ZR[45] was employed. For hard sphere particles near hard or attractive planar surfaces, we found that the inversion procedure reproduced the true particle-surface potential energy to accuracies within 0.1 k_BT at low to moderate particle densities.

In this section, we studied colloidal systems near planar interfaces using potential models specifically relevant to such systems, namely hard sphere, hard sphere + screened electrostatic repulsion, hard sphere + van der Waals attraction, and hard sphere + depletion attraction. In particular we explore the accuracy of different bridge function closures in the DFT of ZR[116] over physically reasonable ranges of potential parameters, particle density, and temperature. We study both forward and inverse DFT calculations. Our results provide insight as to the quantitative limits on accuracy that one can expect from the DFT when comparing with, or interpreting, particle-scale density profiles using experimental data from techniques like CSLM.

4.3 Theory

4.3.1 Forward and inverse analysis

Here we gave the equations for the forward and inverse analysis, for details please check Section 2.3.3.

Forward analysis:

$$\rho(\mathbf{r}) = \rho_b \exp\begin{Bmatrix} -\beta\varphi_{ext}(\mathbf{r}) + \int d\mathbf{r}_1 \left(\rho(\mathbf{r}_1) - \rho_b\right) C_0^{(2)}(\mathbf{r}, \mathbf{r}_1; \rho_b) \\ + B\left[\int d\mathbf{r}_1 \left(\rho(\mathbf{r}_1) - \rho_b\right) C_0^{(2)}(\mathbf{r}, \mathbf{r}_1; \rho_b)\right] \end{Bmatrix} \tag{4.1}$$

Inverse analysis:

$$\begin{aligned} &\beta\varphi_{ext}(\mathbf{r}) = -\ln\left[\frac{\rho(\mathbf{r})}{\rho_b}\right] + \\ &\int d\mathbf{r}_1 \left(\rho(\mathbf{r}_1) - \rho_b\right) C_0^{(2)}(\mathbf{r}, \mathbf{r}_1; \rho_b) + B\left[\int d\mathbf{r}_1 \left(\rho(\mathbf{r}_1) - \rho_b\right) C_0^{(2)}(\mathbf{r}, \mathbf{r}_1; \rho_b)\right] \end{aligned} \tag{4.2}$$

4.3.2 Closures

Four of the closures employed in this work have analytical expressions for B[γ],

Percus-Yevick (PY):[65]

$$B\left[\gamma(\mathbf{r})\right] = \ln\left(1 + \gamma(\mathbf{r})\right) - \gamma(\mathbf{r}) \tag{4.3}$$

Verlet-modified (VM):[67]

$$B[\gamma(\mathbf{r})] = -\gamma(\mathbf{r})^2 / 2(1 + 0.8\gamma(\mathbf{r})) \tag{4.4}$$

Hypernetted chain (HNC):[10]

$$B\left[\gamma(\mathbf{r})\right] = 0 \tag{4.5}$$

Martynov-Sarkisov (MS):[71]

$$B\left[\gamma(r)\right] = \left(1 + 2\gamma(r)\right)^{0.5} - \gamma(r) - 1 \tag{4.6}$$

Another closure employed in this section is the Rogers-Young (RY) [72] which has no analytical expression for B[γ], they gave the equation for $g(r)$:

$$g(r) = \exp\left[-\beta u(r)\right]\left[1 + \frac{\exp\left[\gamma(r) f(r)\right] - 1}{f(r)}\right] \tag{4.7}$$

where $f(r)=1-exp(-\alpha r)$ and α is an adjustable parameter determined by thermodynamic consistency. For the calculation of α, please refer to Section 2.2.3.5. For the numerical function between $B[\gamma(r)]$ and $\gamma(r)$, please read Section 2.2.3.5 and Fig. 4.1

4.3.3 Model Potentials

In this section four different common colloidal potentials were investigated, namely hard spheres, Derjaguin-Landau-Verwey-Overbeek (DLVO) screened electrostatic repulsion, retarded van der Waals (vdW) attraction, and Asakura-Oosawa (AO) depletion attraction.[111] The latter three models each included a hard sphere core. These models are commonly used for interactions in colloidal fluids and span a range of relevant characteristics. The particle-particle and particle-surface potentials were always chosen from the same family for a given calculation. Details are given below.

4.3.3.1 Particle-particle potential models

The first model is hard spheres of diameter σ with a potential given by:

$$\beta u(r) = \begin{cases} \infty, & r < \sigma \\ 0, & r \geq \sigma \end{cases} \tag{4.8}$$

The densities we studied was $\rho\sigma^3$ =0.319, 0.523 and 0.813. Note that a freezing transition occurs at $\rho\sigma^3 = 0.943$ for this model colloid.[117]

The second model is a screened electrostatic potential:[111]

$$\beta u(r) = \begin{cases} \infty, & r < \sigma \\ B\exp\left[-\kappa\left(r-\sigma\right)\right], & r \geq \sigma \end{cases} \tag{4.9}$$

where B is a pre-factor that is a function of colloidal surface charge and κ^{-1} is the Debye length. In this work we chose $\kappa^{-1} = 100$ nm, which corresponds to ionic strengths between 10^{-5} - 10^{-6} M. This range is consistent with carbon dioxide saturated water with trace ionic contaminants and thus represents a relatively large Debye length with respect to practical experiments. We chose $B = 3130$ for this study, which

corresponds to silica colloids with -100 *mV* surface potentials in water at ambient temperature and represents a relatively strong repulsive force. The "effective" diameter of the particles due to the long-range repulsion, which can be found by equating the second virial coefficient to that of a hard sphere fluid, was approximately 2 times that of the hard core. The core density we studied was $\rho\sigma^3 = 0.1$, and thus the "effective" density $\rho_{\text{eff}}\sigma^3$ was about 0.8, which is much closer to the hard sphere freezing density of 0.943.

The third model was a vdW potential for polymer-coated particles:[24]

$$\beta u(r) = \begin{cases} \infty, & r < \sigma + 2\delta \\ -\dfrac{0.5A\sigma}{(r-\sigma)^2}, & r \geq \sigma + 2\delta \end{cases} \tag{4.10}$$

where A is effectively a Hamaker constant and δ is the thickness of an adsorbed layer, which could be adjusted based on the polymer's molecular weight or by changing solvent conditions.[30,32,103] Here we chose A=2.0σ to approximately represent the silica-silica or latex- latex interaction[30] and chose δ=12.5 nm to generate a particle-particle potential with a range of attraction equal to approximately 10% of the hard core diameter. The core density we studied was $\rho\sigma^3$= 0.3.

The last model is the AO depletion potential:[111]

$$\beta u(r) = \begin{cases} \infty, & r < \sigma \\ -\dfrac{4\pi}{3}(a+L)^3\left(1 - \dfrac{3r}{4(a+L)} + \dfrac{r^3}{16(a+L)^3}\right)\Pi, & r \geq \sigma \end{cases} \tag{4.11}$$

where a is the colloidal particle raidus, L is the depletant radius, and Π is the depletant osmotic pressure given in terms of the depletant concentration, ϕ, by $\Pi = \dfrac{6\phi}{\pi(2L)^3}$. In this work, we used $2a$ = 1.0 μm as the colloidal particle diameter, $2L$ = 125 nm as the depletant diameter, and ϕ=0.1 as the depletant concentration to produce an attractive

potential well with a range of 12.5% of the hard core diameter. The density was $\rho\sigma^3$= 0.3.

4.3.3.2 Particle-surface potential models

The external field was always created by a single planar surface, yielding inhomogeneity in the *z* direction only. Four different surface models, which paralleled the particle models, were used. The first was a hard wall:

$$\beta\varphi_{ext}(z)=\begin{cases}\infty, & z<\sigma/2\\ 0, & z\geq\sigma/2\end{cases} \tag{4.12}$$

The second was a screened electrostatic surface:

$$\beta\varphi_{ext}(z)=\begin{cases}\infty, & z<\sigma/2\\ 2B\exp\left[-\kappa\left(z-\sigma/2\right)\right], & z\geq\sigma/2\end{cases} \tag{4.13}$$

with the same parameters as described in the particle models, except that for the pre-factor we use 2*B* according to the Derjaguin approximation[111] for particles interacting with planar surfaces.

The third model was a vdW surface:

$$\beta\varphi_{ext}(z)=\begin{cases}\infty, & z<\sigma/2+2\delta\\ -\dfrac{A\sigma}{\left(z-\sigma/2\right)^2}, & z\geq\sigma/2+2\delta\end{cases} \tag{4.14}$$

with the same parameters as described in the particle models part. The final model is an AO depletion surface:[111]

$$\beta\varphi_{ext}(z)=\begin{cases}\infty, & z<\sigma/2\\ -\pi\left(4L^2\left(\dfrac{L}{3}+a\right)-4Lah+\left(a-L\right)h^2+\dfrac{h^3}{3}\right)\Pi, & z\geq\sigma/2\end{cases} \tag{4.15}$$

where $h=z-\sigma/2$, which is surface separation between colloidal particle and surface, and the other parameters were same as described in the particle models part.

4.4 Results and Discussions

For each model system, we initially solved the OZ equation with a chosen closure and compared the $g(r)$ against that from MC simulation of the homogeneous colloid with the bulk densities given in Section 4.3.3.1. (Note that these are not the bulk densities listed in Table 4.1, which were used to calculate the α value for the RY closure and are much higher than those in Section 4.3.3.1.) Next, we used the direct correlation function from the OZ solution to solve the forward DFT problem via Eq. (4.1) and compared the computed density profile with that obtained from our MC simulations. After that we applied the inverse DFT analysis of Eq. (4.2) to the same model systems using the direct correlation function from the OZ solution and the MC density profile data as "experimental" input. Since we have five different bridge function closures to explore, and two closures are required to solve the DFT problems as described in Section 4.3.2, we have a total of 25 different closure combinations to check for each model fluid.

For RY closure, (Eq. 2.18), we need to determine the α value for different interaction model by thermodynamics consistency. Consistency is obtained when the bulk modulus calculated from the virial equation B_p is equal to that calculated from the compressibility equation B_c. The common approach is to calculate a value of α that satisfies this consistency criterion at a thermodynamic state point where the particle-particle correlations are particularly strong, such as the freezing point, and then use that value of α at other state points.[72] In this work we found that an alternative to enforcing B_p=B_c is to minimize the absolute error in $g(r)$ calculated from OZ equation with the RY closure (as compared to the "exact" result from MC simulation at the same state point); those two methods gave us the same α value within 10 percent. Table 4.1 shows the α values calculated for different potential types and the bulk density at which they were evaluated. Once the value of α is fixed, a numerical relation between $B[\gamma(r)]$ and γ(r) may be obtained by solving the OZ equation and creating a parametric plot (see Fig. 4.1, to be discussed below) using Eq. (2.8).[49]

Table 4.1. Values of the α parameter for the RY closure and the bulk density at which they were evaluated.

potential type	density $\rho\sigma^3$	RY α
hard sphere	0.924	0.16
electrostatic repulsion	0.11	0.21
vdW attraction	0.73	0.42
AO depletion	0.73	0.22

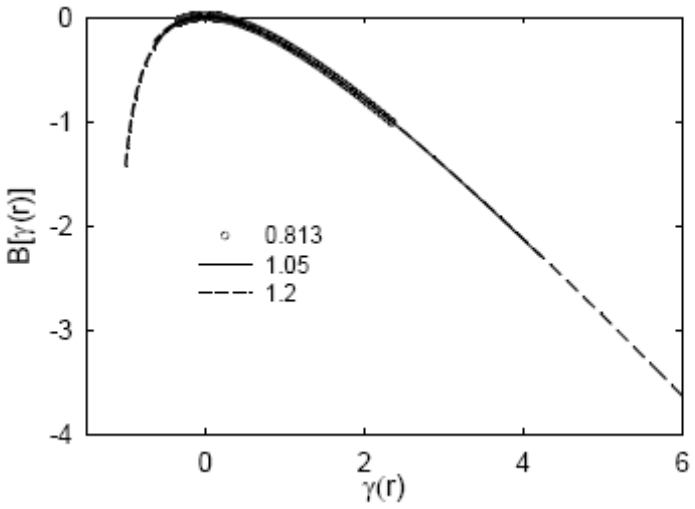

Figure 4.1. Parametric curves for the RY closure for bulk hard spheres. Different symbols represent different densities $\rho\sigma^3$ as given in the legend.

We can reduce the number of combinations by fixing the first closure choice. The goal of the first closure is simply to provide the most accurate bulk direct correlation function from the OZ equation, for use in the DFT formulations of Eqs. (4.1) and (4.2).

So a logical criterion for choosing the first closure is its accuracy in predicting $g(r)$ as compared to the "exact" result from Monte Carlo simulation. PY is typically good for short-ranged potentials while HNC works well for long-range potentials, and RY should be an improvement over both due to its use of an adjustable parameter to enforce thermodynamic consistency. Our OZ results in Fig. 4.2(a), 4.3(a), 4.4(a) and 4.5(a) tend to confirm this. From examination of these Figures, we see that HNC always overpredicts the first peak of $g(r)$. PY and VM are reasonably accurate except for the screened electrostatic potential, where we could not obtain numerical convergence for these closures (nor for MS) due to the long-ranged repulsive potential and high effective density; therefore in Fig. 4.3(a) we show only the HNC and RY results, and RY is seen to be in slightly better agreement with the MC simulation. For the other potentials, MS yields worse overpredictions at contact than HNC, while the PY, VM, and RY results are good and in fact appear quite similar on the plot scales shown. However, absolute error calculations using the MC results as the true values showed that RY always had the least error in $g(r)$. Overall, our results suggest that RY will be the best choice for the first closure. Therefore, for the forward and inverse DFT work, we test only five closure combinations: RY+PY, RY+VM, RY+HNC, RY+MS, and RY+RY.

We note here a problem that arises when implementing the RY+RY closure. The indirect correlation function for the non-homogeneous fluid $\gamma(\mathbf{r}) = \int d\mathbf{r}_1 (\rho(\mathbf{r}_1) - \rho_b) C_0^{(2)}(\mathbf{r}, \mathbf{r}_1; \rho_b)$ sometimes takes on values outside the natural range of the corresponding function for the homogeneous fluid $\gamma(r)$ at the specified bulk density, so we cannot obtain an interpolated value for $B[\gamma(\mathbf{r})]$. Zhou previously addressed this problem by numerically extrapolating the $B[\gamma(\mathbf{r})]$ data outside the natural range. We propose a different solution where $B[\gamma(\mathbf{r})]$ data at higher bulk densities are used to extrapolate the curve. If B is truly a universal functional of $\gamma(r)$, the relationship should not change with density. Figure 4.1 shows the results for hard spheres at three different bulk densities, $\rho_b\sigma^3 = 0.813$, 1.05, and 1.2. The higher-density curves clearly overlap the lowest-density curve in the middle region and smoothly extend it on each

end. We note that the highest density (1.2) is beyond the fluid-solid coexistence region and in fact approaches the random close packing limit. The physical significance of OZ structural correlation functions in this limit has been debated in the literature,[118,119] with the more recent opinion of Sarkisov being that they represent the structure of metastable phases with signatures of ordered domains.[119] For our purposes, the high-density OZ solution provides a smooth extrapolation of our $B[\gamma(\mathbf{r})]$ curve over a larger range.

4.4.1 Hard sphere particles near hard surface

For clarity, we show only the two best closure combinations in Fig. 4.2(b), 4.3(b), 4.4(b) 4.5(b). 4.6(b), and 4.7(b) for the forward DFT problem. Fig. 4.2(b), 4.3(b), and 4.4(b) for hard spheres show that the RY+VM and RY+RY results are quite similar and both tend to overpredict the density value at contact. The overall accuracy of the DFT predictions declines as the bulk particle density increases, and the worst agreement is typically seen at the point of contact with the surface.

Next, we applied the inverse analysis as described in Section II.D to the same systems just considered in Fig. 4.2(b), 4.3(b), and 4.4(b), using the Monte Carlo data as experimental input. We found there were clear parallels in accuracy between the forward and inverse calculations. The overall accuracy of the inversion process declines as the bulk density increases, and the worst results are typically seen near contact. At the lowest bulk density the maximum error is only 0.08 k_BT, but at the highest bulk density the maximum error exceeds 0.5 k_BT in all cases. The RY+VM closure is indeed the best near contact but predicts a deep (~ 0.7 k_BT) local minimum near $z/\sigma = 1$ at the highest bulk density. Fig. 4.2(c), 4.3(c), and 4.4(c) for hard spheres shows that Both RY+VM and RY+RY have similar behavior and magnitude of errors in predicting $\varphi_{ext}(\mathbf{r})$.

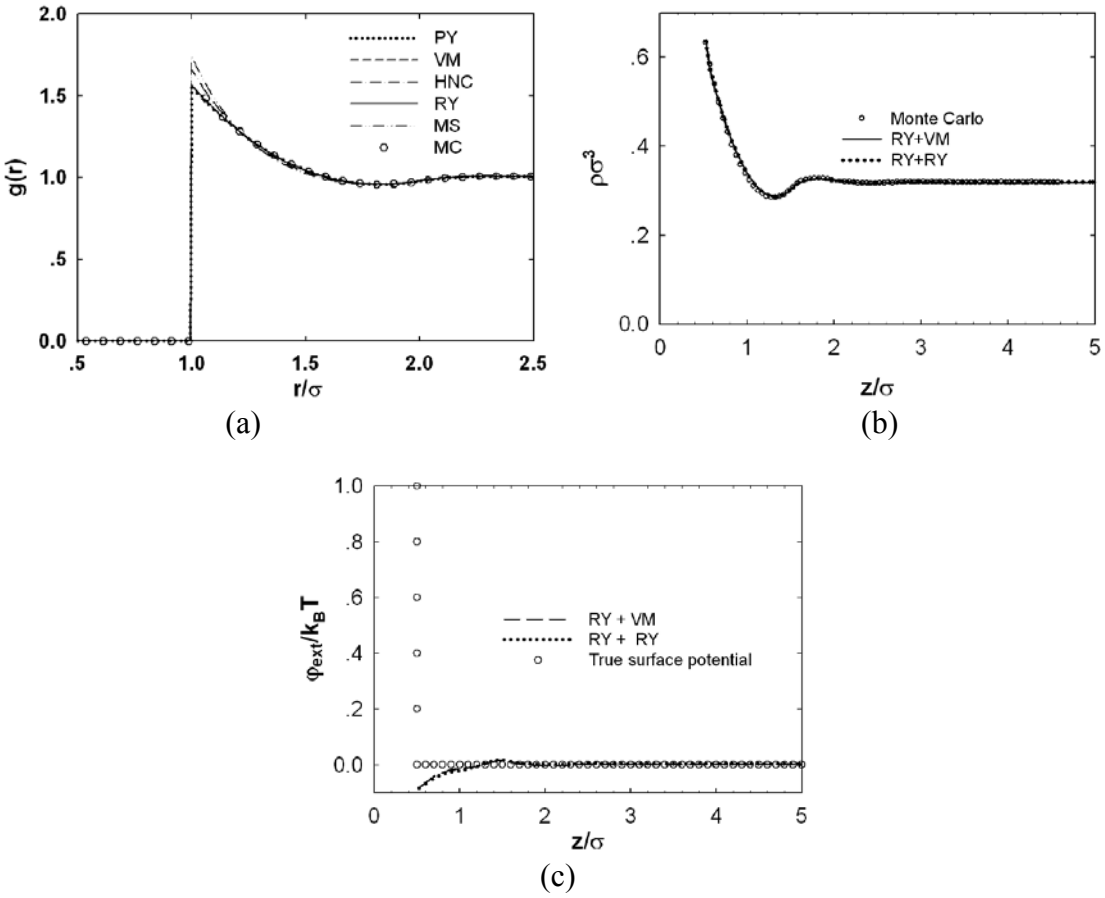

Figure 4.2. (a) Radial distribution functions of a homogeneous hard sphere fluid from the OZ equation in different closures at $\rho_b\sigma^3$=0.319. (b) Density profiles of an inhomogeneous hard sphere fluid near a hard surface at $\rho_b\sigma^3$=0.319 from forward DFT with different closure pairs, compared to MC simulation. (The notation "RY+VM" means that the RY closure was used to obtain the direct correlation function from the OZ equation and the VM form was chosen for $B[\gamma(r)]$ in Eq. (4.1).) (c) Potential energy of a hard sphere particle interacting with a hard surface at $\rho_b\sigma^3$=0.319 as obtained by inverse DFT, compared to the true potential. (Again the labels represent the two closures employed in the DFT.)

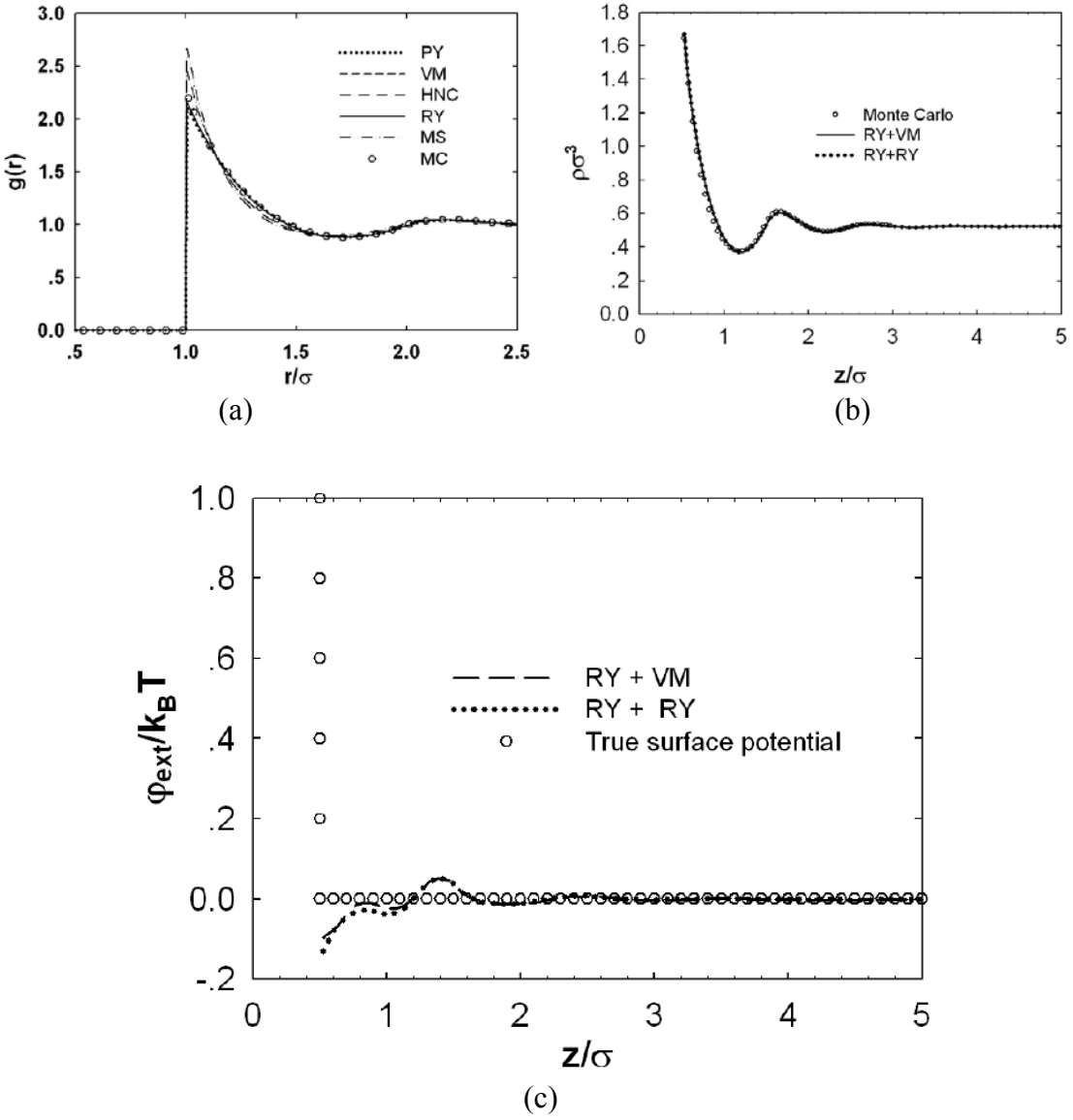

Figure 4.3. (a) Radial distribution functions of a homogeneous hard sphere fluid from the OZ equation in different closures at $\rho_b\sigma^3$=0.523. (b) Density profiles of an inhomogeneous hard sphere fluid near a hard surface at $\rho_b\sigma^3$=0.523 from forward DFT with different closure pairs, compared to MC simulation. (c) Potential energy of a hard sphere particle interacting with a hard surface at $\rho_b\sigma^3$=0.523 as obtained by inverse DFT, compared to the true potential.

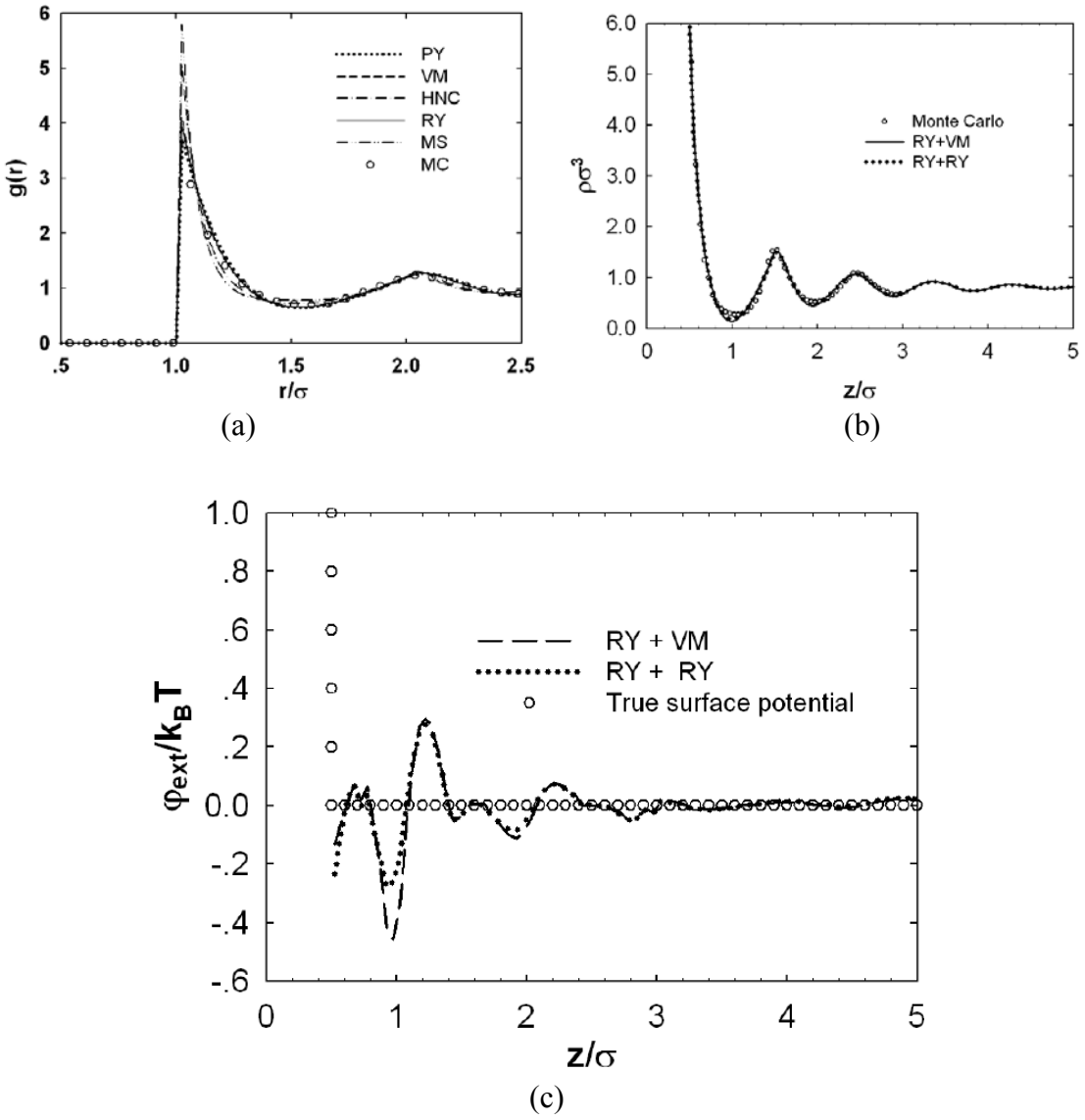

Figure 4.4. (a) Radial distribution functions of a homogeneous hard sphere fluid from the OZ equation in different closures at $\rho_b\sigma^3$=0.813. (b) Density profiles of an inhomogeneous hard sphere fluid near a hard surface at $\rho_b\sigma^3$=0.813 from forward DFT with different closure pairs, compared to MC simulation. (c) Potential energy of a hard sphere particle interacting with a hard surface at $\rho_b\sigma^3$=0.813 as obtained by inverse DFT, compared to the true potential.

4.4.2 Screened electrostatic particles near screened electrostatic surface

Fig. 4.5 (b) for the screened electrostatic potential shows that RY+VM underpredicts the density at the contact while RY+HNC overpredicts it. Fig. 4.5(c) for the screened electrostatic potential shows that the RY+VM and RY+HNC inversions are quite good with no more than 0.1 k_BT error along the steep repulsive part of the potential.

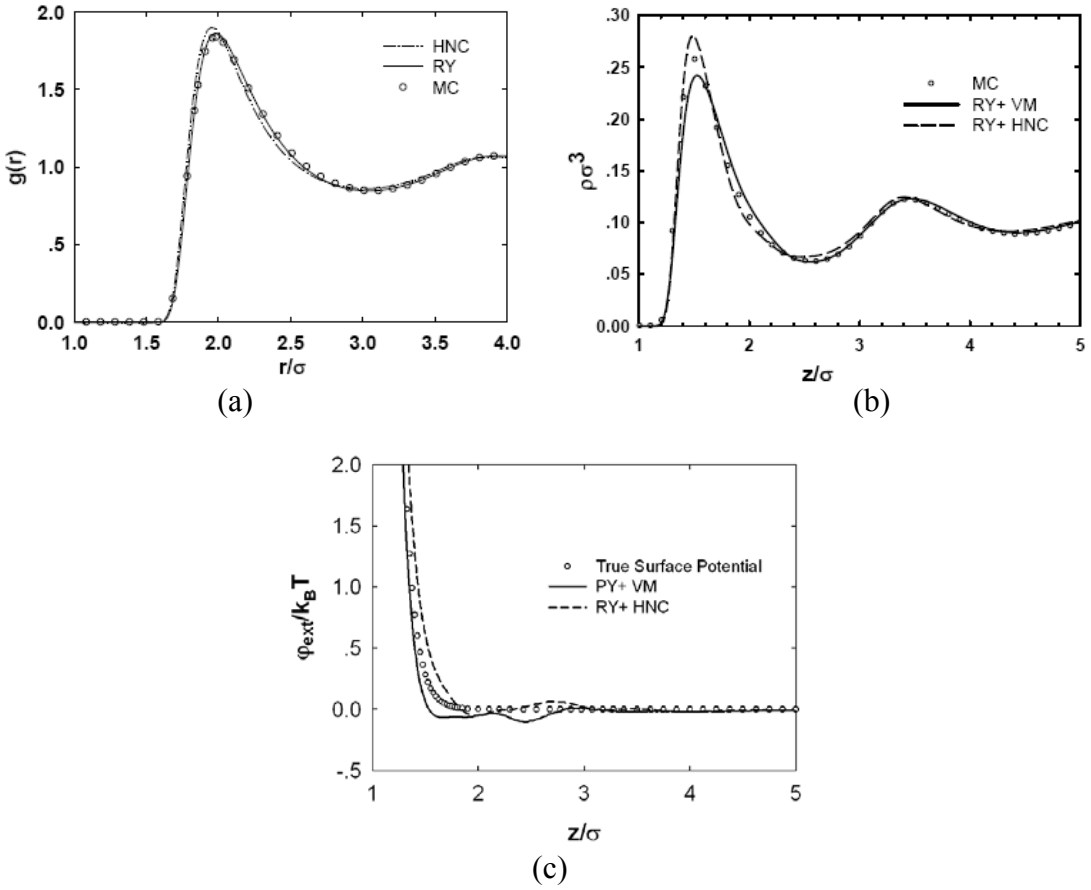

Figure 4.5. (a) Radial distribution functions of a homogeneous screened electrostatic fluid $\rho_b\sigma^3$=0.1. (b) Density profiles of an inhomogeneous screened electrostatic fluid near a screened electrostatic surface at $\rho_b\sigma^3$=0.1 from forward DFT compared to MC simulation. (c) Potential energy of a screened electrostatic particle interacting with a screened electrostatic surface at $\rho_b\sigma^3$=0.1 as obtained by inverse DFT, compared to the true potential. (For details on the potential parameters and bulk density, see Sections 4.3.3.1 and 4.3.3.2.)

4.4.3 Van der Waals particles near Van der Waals surface

Fig. 4.6(b) shows that RY+VM and RY+HNC both overpredict the density at contact, with RY+VM performing slightly better, for the vdW potential. Fig. 4.6(c) for vdW potential shows that RY+VM and RY+HNC are both quite good in the attractive wells, with errors less than 0.1 k_BT, but yield a significant overprediction of about 0.3 k_BT in the region just outside the wells; RY+VM is slightly better than RY+HNC in that region.

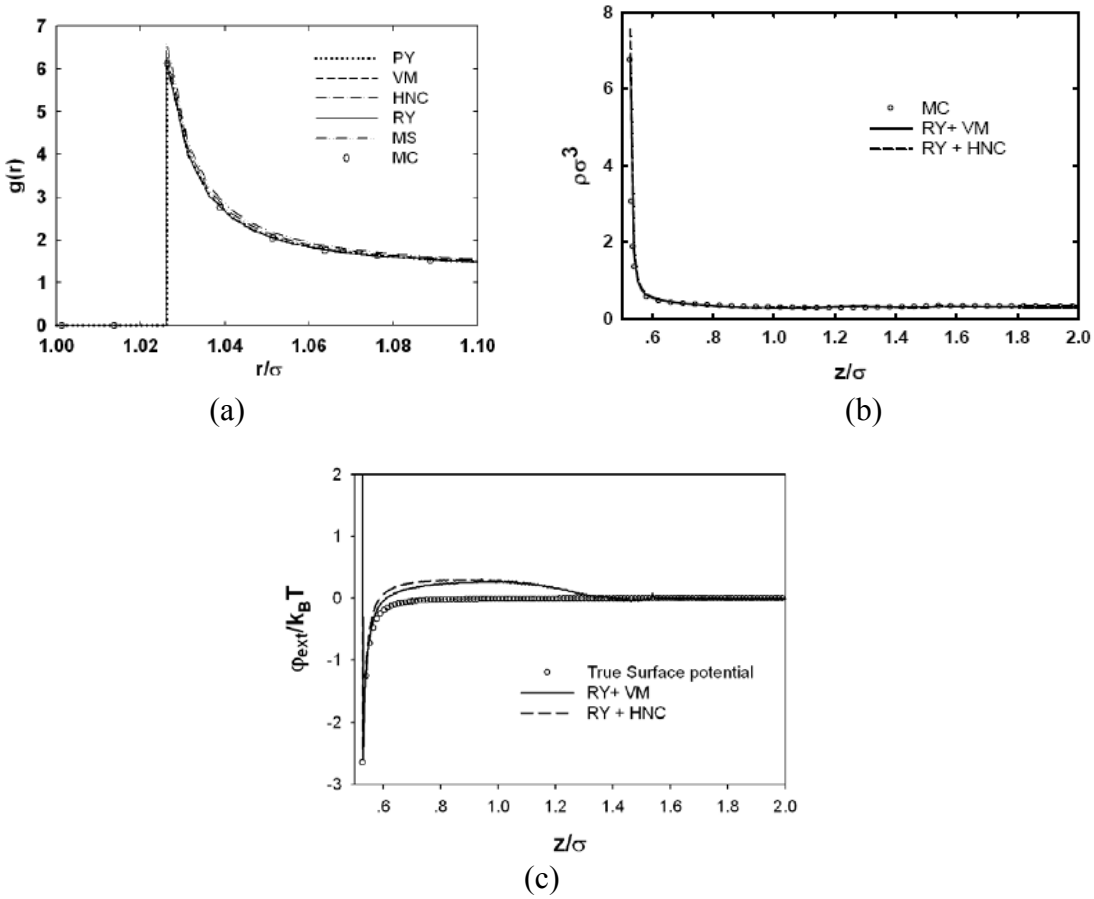

Figure 4.6. (a) Radial distribution functions of a homogeneous vdW fluid $\rho_b\sigma^3$=0.3. (b) Density profiles of an inhomogeneous vdW fluid near a vdW surface at $\rho_b\sigma^3$=0.3 from forward DFT compared to MC simulation. (c) Potential energy of a vdW particle interacting with a vdW surface at $\rho_b\sigma^3$=0.3 as obtained by inverse DFT, compared to the true potential. (For details on the potential parameters and bulk density, see Sections 4.3.3.1 and 4.3.3.2.)

4.4.4 Depletion particle near depletion surface

Fig. 4.7(b) shows that RY+VM and RY+HNC both overpredict the density at contact, with RY+VM performing slightly better, for the AO depletion potential. Fig. 4.7(c) for AO depletion potential shows that RY+VM and RY+HNC are both quite good in the attractive wells, with errors less than 0.1 k_BT, but yield a significant overprediction of about 0.3 k_BT in the region just outside the wells; RY+VM is slightly better than RY+HNC in that region.

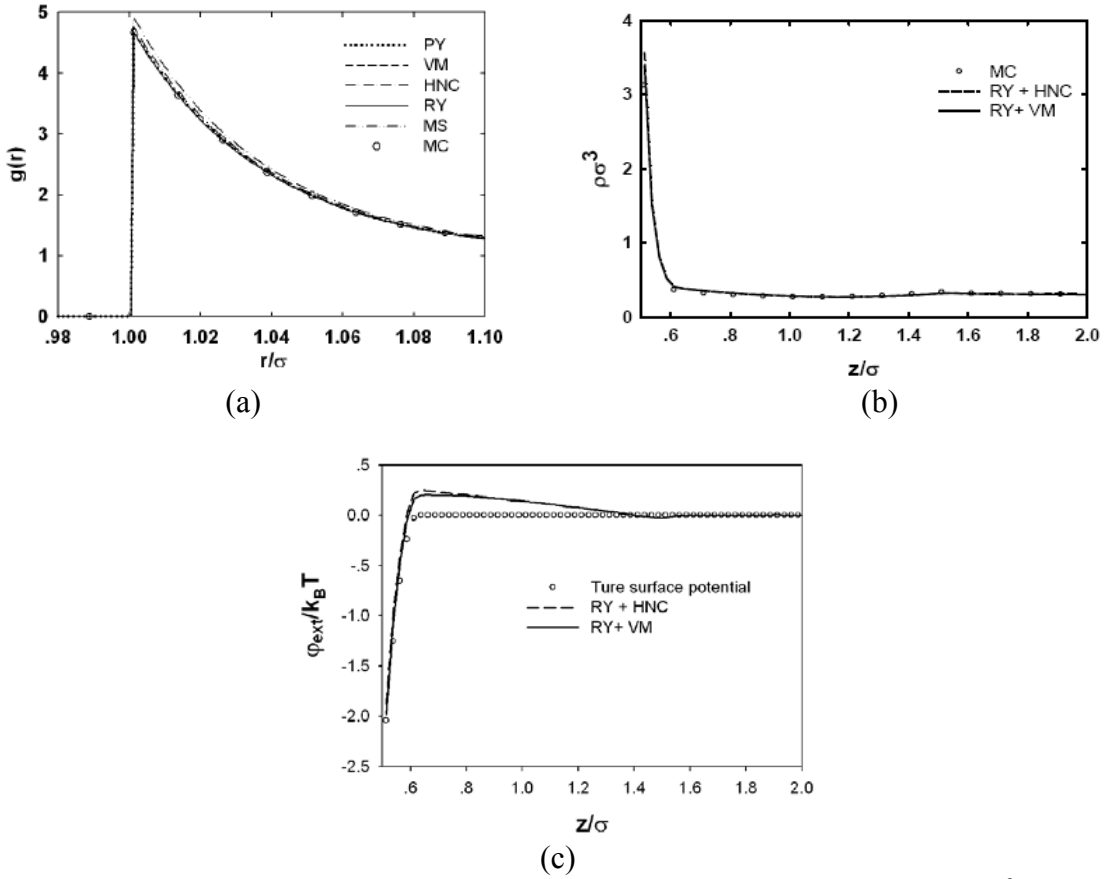

Figure 4.7. (a) Radial distribution functions of a homogeneous AO fluid $\rho_b\sigma^3$=0.3. (b) Density profiles of an inhomogeneous AO fluid near an AO surface at $\rho_b\sigma^3$=0.3 from forward DFT compared to MC simulation. (c) Potential energy of an AO particle interacting with an AO surface at $\rho_b\sigma^3$=0.3 as obtained by inverse DFT, compared to the true potential. (For details on the potential parameters and bulk density, see Sections 4.3.3.1 and 4.3.3.2.)

Table 4.2 is a qualitative summary of the "best" choice for the second closure in the ZR DFT for each colloidal potential type, as judged by the performance in both forward and inverse calculations. (Note that in all cases RY was used as the first closure to get the direct correlation function of the bulk fluid.) The dimensionless bulk density at which each inhomogeneous colloid was studied is also given in the table. The VM closure is the best, or among the best, for all four potential types. The HNC closure does well on the last three potential models, which is interesting because HNC closure does not do well with the bulk fluid OZ equation for these potentials (Fig.s 4.2(a), 4.3(a), 4.4(a), 4.5(a), 4.6(a),and 4.7(a)).

Table 4.2. A qualitative summary of the "best" choice for the second closure in the Zhou and Ruckenstein DFT.

potential type	densities ($\rho_b\sigma^3$)	best second closure
hard sphere	0.319, 0.523, 0.813	VM (RY is a close second)
electrostatic repulsion	0.1	VM or HNC
vdW attraction	0.3	VM (HNC is a close second)
AO depletion	0.3	VM (HNC is a close second)

From our previous work, we know that the accuracy of the DFT declines as bulk density increases.[116] As we can see from Fig. 4.2(c), 4.3(c), 4.5(c), 4.6(c), and 4.7(c), the errors in the inversion process for the best closure combinations are roughly 0.1 k_BT (slightly higher for the regions outside the attractive wells for vdW and AO). For practical reasons, this is about the best resolution that we could expect from a CSLM imaging experiment. Therefore, we can conclude that investigating inhomogeneous

colloidal fluids with bulk densities up to and including those listed in Table II would be satisfactory, but anything higher would likely contain unacceptable errors in the reported particle-surface potential.

4.5 Conclusions

The DFT formulation of ZR was used in forward and inverse modes to make predictions of density profiles and particle-surface potentials for several different colloidal potentials; we expect that such a process will be useful in the interpretation of microscopy measurements of inhomogeneous colloidal fluids near surfaces. The accuracy of the predictions depended on the bulk particle density, potential well depth and the choice of DFT closure relationships. Results from four different particle-particle and particle-surface potentials demonstrated that the RY+VM combination of closures is a good general choice. This closure combination should produce acceptable results (< 0.1 k_BT maximum deviation from true potential) at low to moderate bulk densities ($\rho_b\sigma^3$<0.319) across the different colloidal interaction types. Higher densities are still problematic and will be the focus of future work, as will application of the theory to actual experimental data.

5. RESULTS FOR COLLOIDAL SEDIMENTATION EQUILIBRIUM

5.1 Synopsis

In this section, we use a closure-based DFT formulation to predict the particle density profiles. The particle-particle and particle-surface interactions were modeled with screened electrostatic potentials using parameters taken directly from the CSLM experimental work. The DFT profiles were compared to the experimental and MC results from experiment work. Quantitative agreement was found for the systems with lower, fluid-like particle volume fractions). We also applied DFT in an inverse sense, using the measured particle density profile to extract the underlying particle-surface potential

5.2 Introduction

In Part I of this work,[120] Beckham and Bevan used confocal scanning laser microscopy (CSLM) to measure the equilibrium sedimentation profiles of sub-micron fluorescent core-shell silica colloids near planar surfaces. Solvent and surface conditions were chosen such that the particle-particle and particle-surface interactions were via screened electrostatic repulsion. The number of colloidal particles per unit surface area was varied to produce three types of sediment: shallow fluid (fluid-like colloid volume fractions everywhere), deep fluid (still fluid-like but on the verge of crystallization near the surface), and fluid/solid (having a crystal layer of significant thickness at the surface). The fluorescence intensity profiles from CSLM were used in combination with local density approximation (LDA) models and "density-to-intensity" convolution functions to yield coarse-grained density profiles. Particle-based Monte Carlo simulation, employing the known interaction potentials, provided density profiles with fine-scale resolution for comparison. The CSLM/LDA density profiles were in excellent agreement with the more detailed ones from simulation, allowing for the fact that they cannot capture the layering effects that occur within a few particle diameters of the surface.

As seen in Part I, the inhomogeneity of a colloidal suspension in a gravitational field acting in the z direction can be characterized by the density distribution profile $\rho(z)$. The density profile may reflect interesting phenomena such as layering or phase transition. The particle-particle and particle-surface energetic interactions, as well as the gravitational length scale k_BT/mg and the number of particles per unit surface area, are key variables in determining the equilibrium sedimentation density profile.

Before reviewing previous theoretical studies on sedimentation equilibrium, it is useful to denote two general categories, local and nonlocal, for the techniques applied. Local theories assume that the thermodynamic properties at any elevation z are equivalent to those of a homogeneous (field-free) colloidal fluid of density $\rho(z)$; this assumption is accurate if the density profile does not change significantly over the characteristic length scale of a particle. Completely neglecting the particle-particle interactions leads to the special case of an exponential density profile, which is the well-known Boltzmann or barometric distribution. The effects of particle-particle interactions may be introduced through osmotic equations of state (*e.g.* see Eq. 18 in Part I); the history of this approach goes back to pioneering work in 1914 by Perrin.[121] Nonlocal theories, typically based on some flavor of density functional theory (DFT) or Ornstein-Zernike (OZ) integral equation theory,[42] are capable of capturing the rapid oscillations in density that occur within a few particle diameters of an interface. Nonlocal theories, although more computationally expensive, are probably necessary to do the "nanoscale" interfacial engineering of interest today. Finally, we also have Monte Carlo (MC) simulation,[8,10,41] which yields essentially exact equilibrium results (within statistical and ergodic limitations) for a given model colloid and surface.

Next we briefly review the recent literature on sedimentation theory. About 15 years ago, Biben *et al.*[48] wrote a key paper on the statistical mechanics of sedimentation equilibrium wherein they applied LDA theory and MC simulation to hard-sphere and charge-stabilized colloidal particles near a hard planar surface. Far from the interface, the density profiles predicted from the LDA closely matched the monotonically declining MC profiles; near the interface, the LDA profiles passed smoothly through the

middle of the strongly oscillating (layered) regions of the MC profiles. In one case of hard spheres with a small gravitational length scale (*i.e*. strong gravity), the LDA results predicted density values near the interface that corresponded to the fluid-solid coexistence regime for bulk hard spheres; interestingly, the coarse-grained version of the MC density profile in this case showed significantly enhanced slope near the interface. Biben *et al*. concluded that this overall behavior was indicative of a crystal phase forming in the first few particle layers near the interface. Saksena and Woodcock[43] carried out an LDA study of the sedimentation of soft spheres (r^{-12} repulsion) on a hard surface, with complementary molecular dynamics (MD) simulations. Using literature equations of state for the fluid and solid phases of soft spheres, the LDA was able to accurately predict the density profile at a coarse-grained level, including the elevation at which a fluid-solid phase transition occurred. Interestingly, the MD simulations indicated the presence of some crystalline "mesophases" whose structures are not naturally observed in the bulk. Recently, Mori *et al.*[122] used a slow cooling MC algorithm to crystallize hard spheres under gravity at a hard planar interface; they observed the formation of a "defective (or less-ordered)" crystalline region between the dense crystal at the interface and the fluid phase above. Fluids of greater complexity exhibit interesting phase behavior even in local approximations. Savenko and Dijkstra[123] explored the sedimentation and multiphase equilibrium of hard rod suspensions, and Schmidt *et al.*[47] examined the effects of sedimentation on the phase behavior of mixtures of hard spheres and polymer coils.

Nonlocal theories have also been applied to equilibrium sedimentation problems. Rodriguez *et al.*[59] investigated the density profiles of hard sphere and Yukawa colloidal suspensions inside a planar slit pore under gravity, using inhomogeneous OZ integral equations in the Percus-Yevick closure. Jamnik[60] carried out a similar study with adhesive spheres and corresponding grand canonical MC simulations. Choudhury and Ghosh[124] developed a new DFT approximation, based on a splitting of the potential into repulsive and attractive components, to further study the confined adhesive sphere model. Zhou and Sun[125] investigated the sedimentation equilibrium of hard-core attractive

Yukawa particles by a parameter-free version of the Lagrangian theorem based DFT.[126] Recently, Chen and Ma[46] calculated the density profiles of hard spheres under gravity by fundamental measure[93] DFT and systematically compared the results with those from MC. As might be expected, quantitative agreement with simulation became worse as the gravitational strength or the number of particles per unit surface area was increased. With few exceptions, the nonlocal theoretical studies have focused on fluid-like sediments.

We can briefly summarize previous theoretical studies of colloidal sedimentation in this way. Local theories are satisfactory for predicting coarse-grained density profiles and the elevations at which transitions between expected phases should be observed (as seen in Part I of this work), but not at predicting detailed microstructure near the interface or the emergence of unexpected phases with no bulk analogues. With the appropriate choice of closure (OZ) or free energy functional (DFT), nonlocal theories can make reasonably accurate predictions of interfacial microstructure in fluid-like sediments. However, predicting the details of fluid-solid equilibrium in external fields is still a challenge for nonlocal theories;[127] perhaps this is not surprising, given that quantitative DFT of *bulk* fluid-solid equilibrium is still an outstanding problem.[128] Alternatively, computer power and MC algorithms have improved to the point where they can locate potentially new phases [43,122] and provide a point of comparison with theory.

In this section, we applied the nonlocal closure-based DFT of Zhou and Ruckenstein[45] to the colloidal sediments studied by CSLM experiment, LDA theory, and MC simulation in Part I.[120] Model parameters such as average density and particle-particle and particle-surface potentials were chosen to match the experimental work. These results of this study provide insight as to the quantitative limits on accuracy that one can expect from the DFT when comparing with, or interpreting, fine-scale experimental data from techniques like CSLM. This extends our previous DFT work on colloidal fluids near interfaces.[129,130]

5.3 Theory

5.3.1 Forward and inverse analysis

Here we gave the equations for the forward and inverse analysis, for details please check Section 2.3.3.

Forward analysis:

$$\rho(\mathbf{r}) = \rho_b \exp\begin{Bmatrix} -\beta\varphi_{ext}(\mathbf{r}) + \int d\mathbf{r}_1 \left(\rho(\mathbf{r}_1) - \rho_b\right) C_0^{(2)}(\mathbf{r}, \mathbf{r}_1; \rho_b) \\ + B\left[\int d\mathbf{r}_1 \left(\rho(\mathbf{r}_1) - \rho_b\right) C_0^{(2)}(\mathbf{r}, \mathbf{r}_1; \rho_b)\right] \end{Bmatrix} \tag{5.1}$$

Inverse analysis:

$$\begin{aligned} &\beta\varphi_{ext}(\mathbf{r}) = -\ln\left[\frac{\rho(\mathbf{r})}{\rho_b}\right] + \\ &\int d\mathbf{r}_1 \left(\rho(\mathbf{r}_1) - \rho_b\right) C_0^{(2)}(\mathbf{r}, \mathbf{r}_1; \rho_b) + B\left[\int d\mathbf{r}_1 \left(\rho(\mathbf{r}_1) - \rho_b\right) C_0^{(2)}(\mathbf{r}, \mathbf{r}_1; \rho_b)\right] \end{aligned} \tag{5.2}$$

5.3.2 Closures

Four of the closures employed in this work have analytical expressions for B[γ],

Verlet-modified (VM):[67]

$$B[\gamma(\mathbf{r})] = -\gamma(\mathbf{r})^2 / 2(1 + 0.8\gamma(\mathbf{r})) \tag{5.3}$$

Hypernetted chain (HNC):[10]

$$B\left[\gamma(\mathbf{r})\right] = 0 \tag{5.4}$$

and Zhou-Hong-Zhang (ZHZ):[131]

$$B\left[\gamma(\mathbf{r})\right] = -0.5\gamma(\mathbf{r})^2 \exp\left(-\alpha\gamma(\mathbf{r})\right) \tag{5.5}$$

For the calculation of α, please see Section 2.2.2.6. Another closure employed in this section is the Rogers-Young (RY) [72] which has no analytical expression for B[γ], they gave the equation of $g(r)$:

$$g(r)=\exp\left[-\beta u(r)\right]\left[1+\frac{\exp\left[\gamma(r)f(r)\right]-1}{f(r)}\right] \tag{5.6}$$

where $f(r)$=1-exp(-αr) and α is an adjustable parameter determined by thermodynamic consistency. For the calculation of α, please refer to Section 2.2.3.5. For the numerical function between $B[\gamma(r)]$ and $\gamma(r)$, please read Section 2.2.3.5 and Fig. 4.1

5.3.3 Model Potentials

In this section, screened electrostatic colloidal potential was investigated with parameters obtained from CLSM experiment, where particle- particle $u(\mathbf{r})$, particle-surface $\varphi_{ext}(\mathbf{r})$, and the gravitational potential energy $u_{grav}(h)$ are given as bellow:[111]

$$\beta u(r)=\begin{cases}\infty, & r<\sigma\\ B_{pp}\exp\left[-\kappa(r-\sigma)\right], & r\geq\sigma\end{cases} \tag{5.7}$$

$$\beta u(r)=\begin{cases}\infty, & r<\sigma+\delta\\ 0, & r\geq\sigma+\delta\end{cases} \tag{5.8}$$

$$u_{grav}(h)=Gh=mgh=(4/3)\pi a^3\Delta\rho gh \tag{5.9}$$

where r is center-to-center separation between colloids, a is colloidal radius, B_{pp} is a pre-factor that is a function of colloidal surface charge, κ^{-1} is the Debye length, δ the molecular layer thickness, m is the buoyant particle mass, g is acceleration due to gravity, and $\Delta\rho$=ρ_p-ρ_f where ρ_p and ρ_f are the particle and fluid densities. In this section, we choose κ^{-1}≒9.7 nm, B_{pp}=1554.4, (4/3)πa^3$\Delta\rho g$=0.4 $k_BT/\mu m$.

5.3.4 Bulk density choice in forward and inverse DFT equations

To compare the density profiles calculated by Eq. (5.1) with those from the MC simulations, or the external potential calculated by Eq. (5.2) with the actual external potential, we need to employ the correct bulk density ρ_b. For colloidal suspensions with negligible gravity, as in our previous work,[73,116] the choice of bulk density is simple; it is the constant value of density that is found at distances far from the surface. However, the density profiles of colloidal suspensions under gravity always decay to zero far from

the surface (which is assumed to be at the bottom of the container). In such cases it is helpful to realize that ρ_b is a proxy for the chemical potential of the colloidal fluid. We use the following methods to obtain the proper value of ρ_b.

Under normal experimental or canonical simulation conditions, the total number of particles in the suspension per unit surface area (N/A) is fixed and may be related to the density profile as:

$$\frac{N}{A} = \int_0^L \rho(z)dz \tag{5.10}$$

where L is the vertical height of the container. For the forward analysis using Eq. (5.1), we simply iterate on the variable ρ_b until we obtain an equilibrium density profile that satisfies Eq. (5.10). A similar procedure has been employed elsewhere.[46] At high elevations the contribution of the surface potential becomes negligible so that the total external potential is due to gravity only. For the inverse analysis using Eq. (5.2), we iterate on the variable ρ_b by enforcing the condition $\varphi_{ext}(z_h)=mgz_h$, where z_h is an elevation well outside the range of the surface potential; the values of m and g are assumed to be known. The error between two ρ_b in forward and inverse analysis is within 1%.

5.4 Results and Discussions

We initially solved the OZ equation with RY closure to get the direct correlation function $C_0^{(2)}(\mathbf{r};\rho_b)$ since we already RY is the best closure for homogenous colloidal fluid from our previous work[73]. Next plug $C_0^{(2)}(\mathbf{r};\rho_b)$ into Eq. (5.1) to solve the forward DFT problem with right bulk density (described in Section 5.3.4) and compared the computed density profile with that obtained from our MC simulations. After that we applied the inverse DFT analysis of Eq. (5.2) to the same model systems using $C_0^{(2)}(\mathbf{r};\rho_b)$ and the MC density profile data as "experimental" input. We reduce the number of combinations to four different bridge function closures since we already fix the first closure as RY. The four closure combinations for both forward and inverse DFT work are: RY+VM, RY+HNC, RY+RY, RY+ZHZ.

We note here a problem that arises when implementing the RY+RY closure. The numerical value of $\gamma(\mathbf{r}) = \int d\mathbf{r}_1(\rho(\mathbf{r}_1) - \rho_b)C_0^{(2)}(\mathbf{r},\mathbf{r}_1;\rho_b)$ for the non-homogeneous fluid sometimes takes on a value outside the natural range of $\gamma(r)$ for the corresponding homogeneous fluid at the specified bulk density, so we cannot obtain an interpolated value for $B[\gamma(r)]$. Zhou[49] previously addressed this problem by numerically extrapolating the $B[\gamma(r)]$ data outside the natural range. We proposed a different solution in our previous work[73] where $B[\gamma(r)]$ data at higher bulk densities are used to extrapolate the curve since the relation between B and $\gamma(r)$ does not change with density. If B is truly a universal functional of $\gamma(r)$, the relationship should not change with density.

The two closure combinations shown in Fig. 5.1, 5.2 and 5.3 were generally the best three out of the four combinations tried for solving the forward DFT problem for a colloid near a surface under gravity. Fig. 5.1(a), (b) show the forward DFT and MC for shallow fluid sediment in Part I (526 particles over a 5 μm x 5 μm area). As we can see from Fig. 5.1(a), RY+HNC is quite similar with RY+ZHZ in the top part and RY+HNC is better than RY+ZHZ for the bottom part from Fig. 5.1(b); where RY+ZHZ tends to underpredict the contact density, RY+HNC tends to overpredicts the contact density while both of them overpredict the top part. Fig. 5.1(b) also shows that although RY+VM is worse than RY+HNC at the contact part still RY+VM do an excellent work in the overall work and it can catch both bottom and top part perfectly; while LDA and Perturbation theory in Part I can not account for the structure of bottom part. The problem of VM closure is as we increase the number of colloidal particle, the $\gamma(\mathbf{r}) = \int d\mathbf{r}_1(\rho(\mathbf{r}_1) - \rho_b)C_0^{(2)}(\mathbf{r},\mathbf{r}_1;\rho_b)$ at the contact part will decrease and VM closure will fail as the $\gamma(r)$ getting close to -1.25, which leads $B[\gamma(r)]$ to infinity.

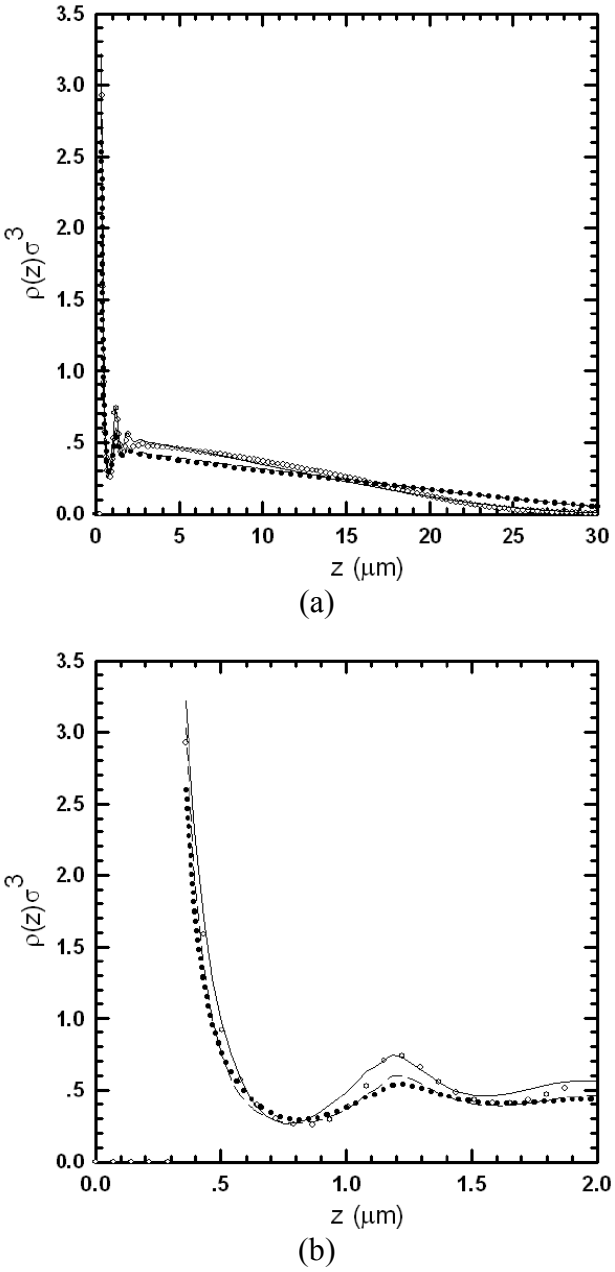

Figure 5.1 (a) Density profile of screened electrostatic colloidal particle (potential parameter in section 5.3.3 for shallow fluid sediment) in contact with a steric wall under gravity evaluated from DFT and MC simulation. RY+VM means $C_0^{(2)}(\boldsymbol{r};\rho_b)$ solved by OZ equation with RY approximation and VM as the bridge function. The solid (—), dash (--), and dotted (···) lines denote the RY+VM, RY+HNC, RY+ZHZ respectively. The open circles are MC simulation results. (b) Same as (a) but focus on contact part.

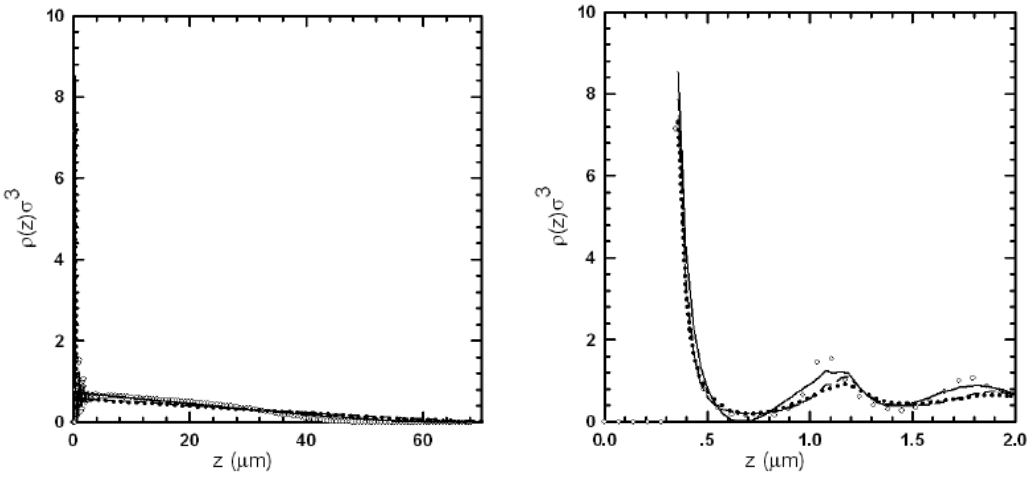

(a) (b)

Figure 5.2 (a) Density profile of screened electrostatic colloidal particle (potential parameter in section 5.3.3 for 1306 particles over a 5 μm x 5 μm) in contact with a steric wall under gravity evaluated from DFT and MC simulation. The solid (—), dash (--), and dotted (···) lines denote the RY+VM, RY+HNC, RY+ZHZ respectively. The open circles are MC simulation results. (b) Same as (a) but focus on contact part.

To test the breakdown of VM closures, we did several forward DFT calculations and found that when number of particles in MC simulation exceed 1306 over a 5 μm x 5 μm area will cause VM closure failure while other parameter keeping the same (see Part I). Fig. 5.2(a), (b) show the density profile by forward DFT and MC. Again RY+VM is still best closures combination, but overall accuracy declines which follows the same trend as our previous work[116]. RY+VM overpredicts top part a little bit and can not catch the first peak near the bottom part from Fig. 5.2(b). RY+HNC is better than RY+VM in contact density prediction from Fig. 5.2(b).

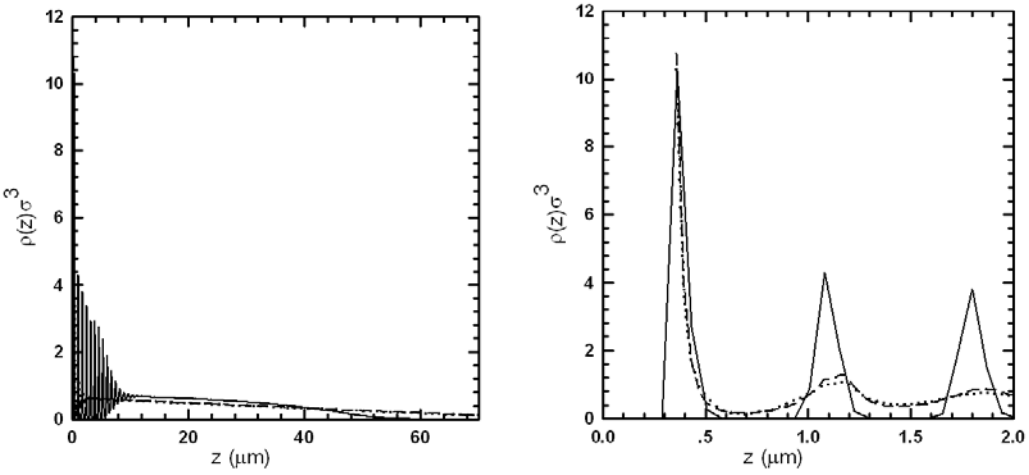

(a) (b)

Figure 5.3 (a) Density profile of screened electrostatic colloidal particle (potential parameter in section 5.3.3 for 1820 particles over a 5 μm x 5 μm) in contact with a steric wall under gravity evaluated from DFT and MC simulation. The dash (--) and dotted (¨) lines denote the RY+HNC, RY+ZHZ respectively. The open circles are MC simulation results. (b) Same as (a) but focus on contact part.

We also did forward DFT to the deep fluid sediment (1820 particles over a 5 μm x 5 μm area) as described in Part I. At this density RY+VM fails and RY+HNC and RY+ZHZ can not describe the system accurately. Both of them overpredict the top part and underpredict the bottom part. But for the contact density, both of them did a good job from Fig. 5.3(b). It is very clearly that there are crystallizing phenomena at the bottom from the MC density profile.

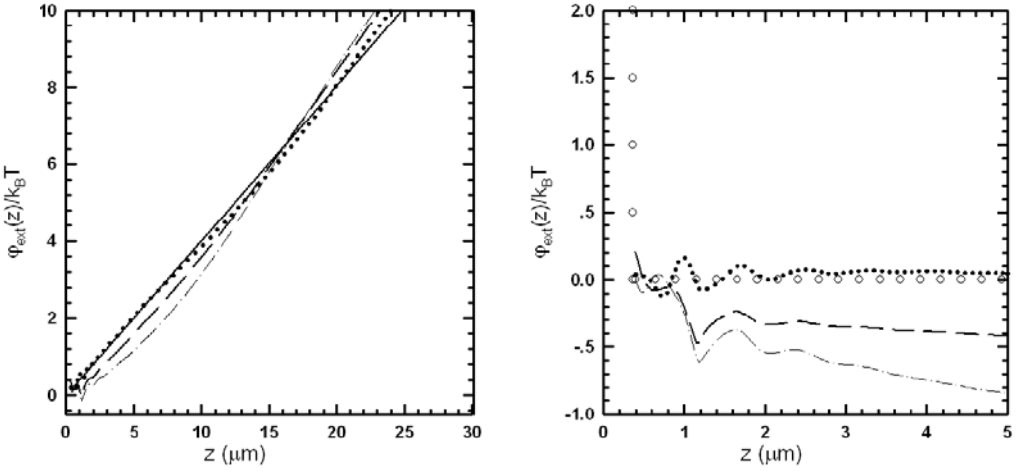

(a) (b)

Figure 5.4 (a) Potential energy of screened electrostatic colloidal particle in contact with a hard wall under gravity solved by DFT using MC simulation result as input. (b) same as (a) but subtract gravitational potential. The dotted (···), dash (--), and dash-dot (- · -) lines denote the RY+VM , RY+HNC, RY+ZHZ respectively. The solid (—) line shows the exact potential energy.

Next we did inverse work for the three density shows above. From our previous paper,[116] we found for $\varphi_{ext}^{pred}(\mathbf{r})$ results, there were clearly parallels in accuracy between the forward and inverse calculations. The overall accuracy of the inversion process declines as the bulk density increases, and the worst results are typically seen near contact. For shallow fluid sediment in Part I, Fig. 5.4(a) shows the RY+VM closure is indeed the best for both bottom and top part with maximum error less than 0.2 k_BT. While for RY+HNC and RY+ZHZ closure predicts a deep (~0.6 k_BT) local minimum near the first peak where z=1.2 μm from Fig. 5.4(b). For the bottom and top part, the maximum error predicted by RY+HNC is around 1.5 k_BT. As we can see from Fig. 5.1(a) and 5.1(b), the RY+HNC and RY+ZHZ underpredict the density profile from z=2μm to z=12.5μm and them overpredict the density from z=20μm for mass balance. This cause the inverse anslysis of RY+HNC and RY+ZHZ very poor from z=2.0μm (Fig. 5.4(b)). But for RY+VM since it did an excellent job for overall forward prediction, it also did an

excellent job in inverse analysis. Inverse DFT results for breakdown density for VM closure case and deep fluid sediment were carried out, but that the results were extremely poor, with errors on the order of more than 2 k_BT. So we did not list those results in this paper.

5.5 Conclusions

DFT formulation of Zhou and Ruckenstein was used to obtain the equilibrium density profile and predict the particle-surface potentials from the density profile information. Different choices of DFT also have been tested, RY+VM combination of closures still the best among reduced 5 available closures combinations after the screen process for bulk colloidal particles. Results shows that the RY+VM combination of closures would produce acceptable results (< 0.2 k_BT maximum deviation from true potential) for low total particle density ($\rho_{total}\sigma^3$=0.17, silica particles with k^{-1}=9.7nm, pre-factor=1554, and diameter=720nm). The accuracy of the predicted potential depended on the total particle density and gravitational potential. The prediction declines as the particle density increase and RY+VM closures will fails at some particle density due to this instinct forms. Future work will focus on the performance of closures at higher particle density and strong gravitational potential. We will compare the forward analysis with CLSM experiment and we expect the inverse analysis can be a very useful tool in predicting the particle-surface potential from CLSM measurements.

6. COLLOIDAL SELF-ASSEMBLY ON CHEMICALLY AND PHYSICALLY PATTERNED SURFACES

6.1 Synopsis

In this section, we extend our work in Section 4 and 5 to the colloidal self-assembly on chemically and physically patterned surfaces. Three cases have been studied, which are hard sphere particle near hard channel, hard sphere particles near electrostatic repulsive patterned surface under gravity and silica colloidal particle near gold-glass and gold-gold patterned surface without gravity respectively. Our results shows high accuracy for templated colloidal self-assembly.

6.2 Introduction

Understanding of fundamental mechanisms that drive the assembly of particles on patterned surfaces (chemical or physical heterogeneous surface or microfabricated patterned surface) provides the strategies to fabricate colloidal microstructures. Integrating colloidal particles into more complex structures is now a key challenge for modern technology especially for nano and micro scaled devices. However, the templated colloidal self assembly into two and three dimensional structures have been demonstrated at length scales from several nanometers up to millimeters.[132] Most of those published "templated colloidal self assembly" rely on shape complementarily of the objects, the surface tension at the interface of an auxiliary liquid and the object surfaces, specific molecular interactions between the individual objects, and external fields such as electric or magnetic fields. These processes are typical irreversible and form disorder microstructures such as gels and aggregates instead of ordered microstructures such as crystal.

The state of art technique to measure directly measure physical and chemical surface heterogeneity includes spectroscopic techniques (surface plasmon resonance,[133] total internal reflection fluorescence,[134] etc.) and scanning probe techniques (atomic force microscopy,[21] chemical force microscopy,[135] etc.). Spectroscopic techniques detect

surface heterogeneity at k_BT scaled thermal energy fluctuation using appropriate adsorption models to interpret the equilibrium adsorption via changes in interfacial optical properties.[136] Scanning probe techniques directly measure physical and chemical surface heterogeneity at scale of *pN* forces via the mechanical deflection of cantilevers at different normal and lateral positions near surfaces due to cantilever's spring constant and the reliable smallest deflection.[136] The advantage of scanning probe method over spectroscopic method is that it direct measure the surface landscape; on the other hand, the disadvantage is that it can not measure the weak equilibrium interaction at order of thermal energy k_BT, which is essential to templated colloid self assembly reversibly and autonomously, and it can not measure large surface areas and ensembles, which lacks the statistical significance.

Despite the successful work for spectroscopic and scanning probe methods in atomic and molecular interactions on heterogeneous surfaces, very few works have been reported to study colloidal self assembly on heterogeneous or patterned surfaces.[136] Although numbers of studies have been reported claimed as "templated colloidal self-assembly", they involve the irreversible deposition or complete depletion of colloids on surface pattern features.[137] Wu *et al*.[136] mentioned that no measurements of equilibrium interactions at nanometer or k_BT scale between colloids and physical or chemical patterns have yet been reported. They proposed a new technique so called Diffusing Colloidal Probe Microscopy (DCPM), which is the integration and extension of single-particle Total Internal Reflection Microscopy (TIRM)[5] and multi-particle Video Microscopy (VM)[37] methods, to measure colloidal particle interacting with patterned surface by inverse the tracked three dimensional colloidal trajectories near surface via Boltzmann equation. The resolution of DCPM is order of nanometer in direction normal to surface and half pixel of lateral particle center coordinates.[136] Their measurements indicated the average equilibrium interactions of levitated colloidal particles with different pattern surface features.

However, the multi-body and multi-dimension interaction between particles will invalidate the Boltzman equation for dense colloidal fluids. The objective of this section

is to develop a successful numerical tool to correctly image the patterned surface energetic landscapes at high colloids density. Density Functional Theory (DFT) is a good option for this study and it has been a useful tool for studying confined colloidal fluids with homogeneous surface.[42] A major advantage of DFT is that it predicts equilibrium density profiles and associated thermodynamic properties at a computational cost significantly lower than that required for direct simulation methods. However, very few studies have investigated the colloidal self assembly with physically or chemically patterned surfaces. Frink and Salinger[138] studied wetting of a chemically heterogeneous surface by nonlocal DFT, which is related to this work. In their work, two dimension (2D) implementation of fundamental measure theory (FMT) was used for a striped surface model to study the consequence of chemical heterogeneity on wetting with Lennard-Jones particle-particle potential.

In Section 4 and 5, we explored an inversion of DFT where we calculated the external potential field from a known density profile in an inhomogeneous fluid interacting planar surface with or without gravity. The closure-based DFT of Zhou and Ruckenstein(ZR) [45] was employed. In those sections, we studied colloidal systems near planar interfaces using potential models namely hard sphere, hard sphere + screened electrostatic repulsion, hard sphere + van der Waals attraction, and hard sphere + depletion attraction. In particular we explore the accuracy of different bridge function closures in the DFT of ZR[116] over physically reasonable ranges of potential parameters, particle density, and temperature.

In this section, we extended the nonlocal closure-based DFT of ZR[45] to the colloidal self assembly on chemically or physically patterned surface using the hard sphere, hard sphere + screened electrostatic repulsion, hard sphere + van der Waals attraction models. As stated in Section 4, the combination of Rogers-Young and modified-Verlet closures consistently performed well across the different potential models. In this section, we also test those for different particle and surface features.

6.3 Theory

6.3.1 Forward and inverse analysis

Here we gave the equations for the forward and inverse analysis, for details please check Section 2.3.3.

Forward analysis:

$$\rho(\mathbf{r}) = \rho_b \exp\begin{Bmatrix} -\beta\varphi_{ext}(\mathbf{r}) + \int d\mathbf{r}_1 \left(\rho(\mathbf{r}_1) - \rho_b\right) C_0^{(2)}(\mathbf{r}, \mathbf{r}_1; \rho_b) \\ + B\left[\int d\mathbf{r}_1 \left(\rho(\mathbf{r}_1) - \rho_b\right) C_0^{(2)}(\mathbf{r}, \mathbf{r}_1; \rho_b)\right] \end{Bmatrix} \tag{6.1}$$

Inverse analysis:

$$\begin{aligned} &\beta\varphi_{ext}(\mathbf{r}) = -\ln\left[\frac{\rho(\mathbf{r})}{\rho_b}\right] + \\ &\int d\mathbf{r}_1 \left(\rho(\mathbf{r}_1) - \rho_b\right) C_0^{(2)}(\mathbf{r}, \mathbf{r}_1; \rho_b) + B\left[\int d\mathbf{r}_1 \left(\rho(\mathbf{r}_1) - \rho_b\right) C_0^{(2)}(\mathbf{r}, \mathbf{r}_1; \rho_b)\right] \end{aligned} \tag{6.2}$$

6.3.2 Closures

Three of the closures employed in this work have analytical expressions for B[γ], Verlet-modified (VM):[67]

$$B[\gamma(\mathbf{r})] = -\gamma(\mathbf{r})^2 / 2(1 + 0.8\gamma(\mathbf{r})) \tag{6.3}$$

Hypernetted chain (HNC):[10]

$$B\left[\gamma(\mathbf{r})\right] = 0 \tag{6.4}$$

and Zhou-Hong-Zhang (ZHZ):[131]

$$B\left[\gamma(\mathbf{r})\right] = -0.5\gamma(\mathbf{r})^2 \exp\left(-\alpha\gamma(\mathbf{r})\right) \tag{6.5}$$

For the calculation of α, please check section 2.2.3.6. Another closure employed in this section is the Rogers-Young (RY) [72] which has no analytical expression for B[γ], they gave the equation of $g(r)$

$$g(r)=\exp\left[-\beta u(r)\right]\left[1+\frac{\exp\left[\gamma(r)f(r)\right]-1}{f(r)}\right] \tag{6.6}$$

where $f(r)$=1-exp(-αr) and α is an adjustable parameter determined by thermodynamic consistency. For the calculation of α, please refer to Section 2.2.3.5. For the numerical function between $B[\gamma(r)]$ and $\gamma(r)$, please read Section 2.2.3.5 and Fig. 4.1

6.3.3 Model Potentials

In this section, three different cases have been studied with different colloidal potentials under different surface features. The fist case is hard sphere particles near hard channel, where particle- particle $u(\mathbf{r})$ and particle- surface $\varphi_{ext}(\mathbf{r})$ are given as bellow:

$$\beta u(r)=\begin{cases}\infty, & r<\sigma\\ 0, & r\geq\sigma\end{cases} \tag{6.7}$$

$$\beta\varphi_{ext}(\mathbf{r})=\begin{cases}\infty, & \mathbf{r}<\sigma/2\\ 0, & \mathbf{r}\geq\sigma/2\end{cases} \tag{6.8}$$

The densities we studied was $\rho\sigma^3$ =0.3. Note that a freezing transition occurs at $\rho\sigma^3=0.943$ for this model colloid.[117]

The second case is hard sphere particles near screened electrostatic patterned surface under gravity, where particle- particle $u(\mathbf{r})$, particle- surface $\varphi_{ext}(\mathbf{r})$, and the gravitational potential energy $u_{grav}(h)$ are given as bellow:[111]

$$\beta u(r)=\begin{cases}\infty, & r<\sigma\\ 0, & r\geq\sigma\end{cases} \tag{6.9}$$

$$\beta\varphi_{ext}(\mathbf{r})=\begin{cases}\infty, & \mathbf{r}<\sigma/2\\ B_{pw}\exp\left[-\kappa\left(\mathbf{r}-\sigma/2\right)\right], & \mathbf{r}\geq\sigma/2\end{cases} \tag{6.10}$$

$$u_{grav}(h)=Gh=mgh=(4/3)\pi a^3\Delta\rho gh \tag{6.11}$$

where B_{pw} are a pre-factor that is a function of colloidal surface charge and κ is the

Debye length, h is the height above the wall, m is the buoyant particle mass, g is acceleration due to gravity, and $\Delta\rho=\rho_p-\rho_f$ where ρ_p and ρ_f are the particle and fluid densities. To model chemically or physically patterned surface, we divided the surface into two part in the y direction with same width = 5σ, (σ is colloidal particle diameter) but different potential energy e.g. different B_{pw1}, B_{pw2}. The parameters for particle-particle and particle-surface potential energy are listed in table 6.1.

Table 6.1. Particle-particle and particle-surface potential energy profile parameters

	Hard Sphere	
$\sigma(\mu m)$	1.58	
κ^{-1}/nm	0.0	
$\Delta\rho(kg/cm^3)$	38.4	
$\rho_{total}\sigma^3$	0.1	
B_{pw}/k_BT	5941	27456

The last case is screened electrostatic colloids on a gold-glass and gold-gold pattern surface with thickness δ_{Au} given by table 6.2. Where particle-particle potential is DLVO screened electrostatic repulsion; particle-surface is DLVO screened electrostatic repulsion + retarded van der Waals (vdW) attraction[111] given as following:

$$\beta u(r)=\begin{cases}\infty, & r<\sigma\\ B\exp\left[-\kappa\left(r-\sigma\right)\right], & r\geq\sigma\end{cases} \tag{6.12}$$

$$\beta\varphi_{ext}(\mathbf{r})=\begin{cases}\infty, & \mathbf{r}<\sigma/2\\ 2B\exp\left[-\kappa\left(\mathbf{r}-\sigma/2\right)\right]-\dfrac{A\sigma}{\left(\mathbf{r}-\sigma/2\right)^p}, & \mathbf{r}\geq\sigma/2\end{cases} \tag{6.13}$$

where A is effectively a Hamaker constant, p is power law expression for retarded vdW determined by Lifshitz theory and Derjaguin Approximation[111]. The parameters for patterned surface are given by table 6.2.[136]

Table 6.2. Particle-surface potential energy parameters

	gold-glass		gold-gold	
δ_{Au}/nm	0	10	9	18
κ^{-1}/nm	9.58	9.58	9.64	9.64
B'/J nm^{-1}	5.53	1.21	1.77	1.64
A/k_BTnm^{p-1}	2.10	8.44	8.29	8.97
p	2.15	2.04	2.04	2.03

6.4 Results and Discussions

6.4.1 Hard sphere particles near hard channel

Fig. 6.1 and 6.2 shows the forward and inverse result for hard sphere particle near hard channel. Channel patterned surface is a common used template and can be obtained through Microcontact printing technique.[139,140] Fig. 6.1a shows the MC simulation result at bulk density $\rho_b\sigma^3$=0.13 with channel depth=3σ in z direction and width 10σ:10σ:10σ in y direction respectively (10σ:10σ:10σ means the total width 30σ is divided into three parts with 10σ each to represent top-bottom-top of channel features). Fig. 6.1b shows the DFT result with RY+VM closure combination solved by Eq.(6.1), which has a perfect match with MC result. Fig. 6.1c shows the predicted the external potential energy $\varphi_{ext}(\mathbf{r})$ through Eq. (6.2) using Fig. 6.1a as input. As we seen form Fig. 6.1a, the result is overall quite good with error < 0.05 k_BT. For DFT calculation in colloidal self assembly on patterned surface, the major challenging is the

computational time, which is still faster than molecular simulation such as MC. In this case, it took about 16 hours on regular PC for the forward analysis, i.e. to generate Fig. 6.1b. However it only took about 2 minutes for the inverse analysis, i.e. to generate Fig. 6.1c. The inverse analysis by ZR[45] is extremely efficient and is well-suited to our objective as we stated in Section 1. We may use the experimental result such as CLSM and DCPM to measure the three dimension density profile to predict the particle-surface potential very quickly and accurately.

One interesting behavior about the density profile is that both MC and DFT show that the density at the concave corner is higher than the center of channel bottom due to well known entropy effect[141] as we stated in the Section 1. In nature, the non-covalent interaction competing with entropy will leads to a rich variety of structures and phases. So we narrowed the channel width in the bottom from 10σ to 1.5σ and performed the forward and inverse analysis at bulk density $\rho_b\sigma^3$=0.15. Again, Fig. 6.2a and 6.2b show the perfect match and Fig. 6.2c shows the error is less than 0.05 k_BT. At this width, only one particle can fit into the bottom of channel and particles prefer to stay there due to the entropy effect. As we turn on the attraction between particles, nanowire may forms at the bottom of channel. Lin *et al.*[142] did some experiment somehow related to this calculation on investigating entropically driven colloidal with depletion potential crystallization on pattern surface.

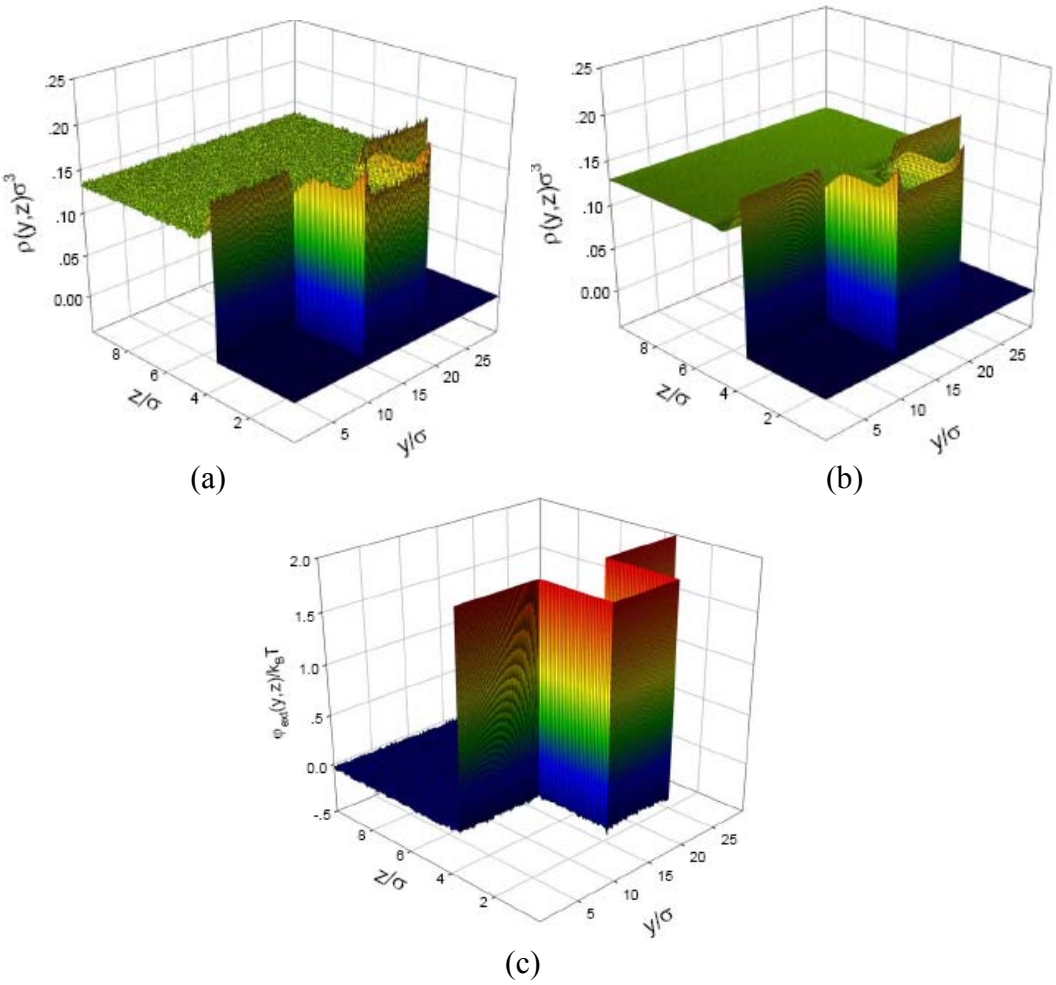

Figure 6.1. (a) Density profiles of an inhomogeneous hard sphere fluid near a hard channel with depth=3σ, with width 10σ:10σ:10σ in y direction at $\rho_b\sigma^3$=0.13 from MC simulation. (b) Same as (a) but got from Eq. (6.1) with RY+VM closure combination. (c) Potential energy of a hard sphere particle near a hard channel with depth=3σ, with width in y direction 10σ:10σ:10σ at $\rho_b\sigma^3$=0.13 as obtained by inverse DFT (Eq. (6.2)) using (a) as input.

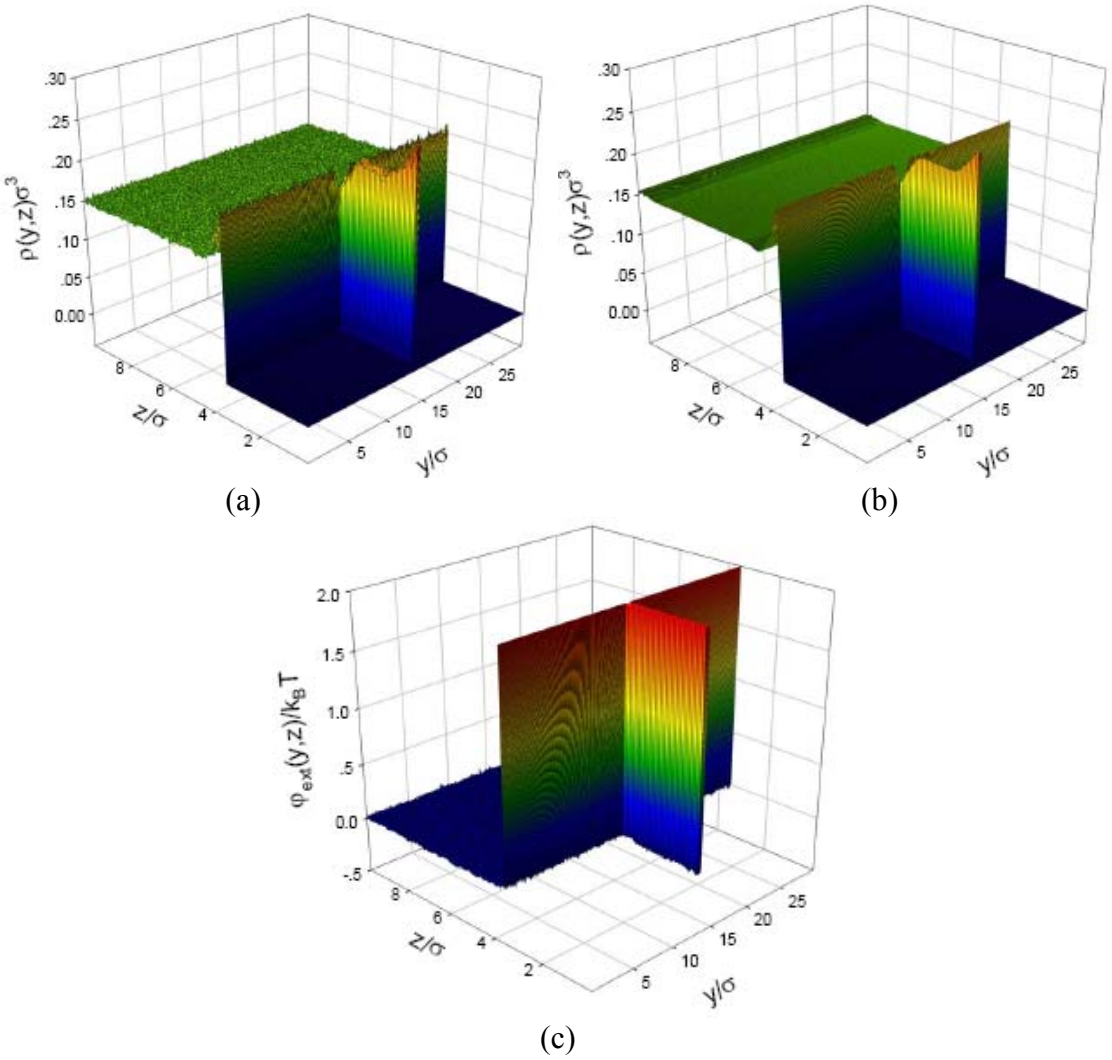

Figure 6.2. (a) Density profiles of an inhomogeneous hard sphere fluid near a hard channel with depth=3σ, with width 14.3σ:1.5σ:14.2σ in y direction at $\rho_b\sigma^3$=0.15 from MC simulation. (b) Same as (a) but got from Eq. (6.1) with RY+VM closure combination. (c) Potential energy of a hard sphere particle near a hard channel with depth=3σ, with width in y direction 14.3σ:1.5σ:14.2σ at $\rho_b\sigma^3$=0.15 as obtained by inverse DFT (Eq. (6.2)) using (a) as input.

6.4.2 Colloidal particles near screened electrostatic patterned surface under gravity

For a suspension of large colloidal particles with a size on the order of several hundred nanometers, the gravitational potential exerted on the fluid particles may be comparable to the thermal energy k_BT; therefore, the effect of the gravitational potential should not be ignored[125]. As in Section 5, DFT have been extensively used to study the sedimentation problem using different particle-particle potential. However, quite a few works has been done for colloidal particles near patterned surface under gravity. In this section, we first study the hard sphere particle near long range screened electrostatic repulsion patterned surface under gravity. Later, we studied the short range screened electrostatic silica particle near short range screened electrostatic patterned surface.

For the bulk density choice in forward and inverse analysis, we use the same method described in Section 5. In short, we iterate the bulk density ρ_b until we obtain the total number of particle integrated form density profile math with MC or experiment for forward analysis; we iterate the bulk density ρ_b until we can obtain the right known gravitational potential at some elevation far from the surface bottom. The error between two ρ_b in forward and inverse analysis is within 1%. Fig. 6.3a and 6.3b show the density profiles for hard sphere particle near screened electrostatic repulsion patterned surface by MC and DFT with very good agreement. Fig. 6.3c shows the inverse potential energy and error of prediction can be seen in Fig. 6.3d is less than $0.3k_BT$ for long range electrostatic repulsive potential energy.

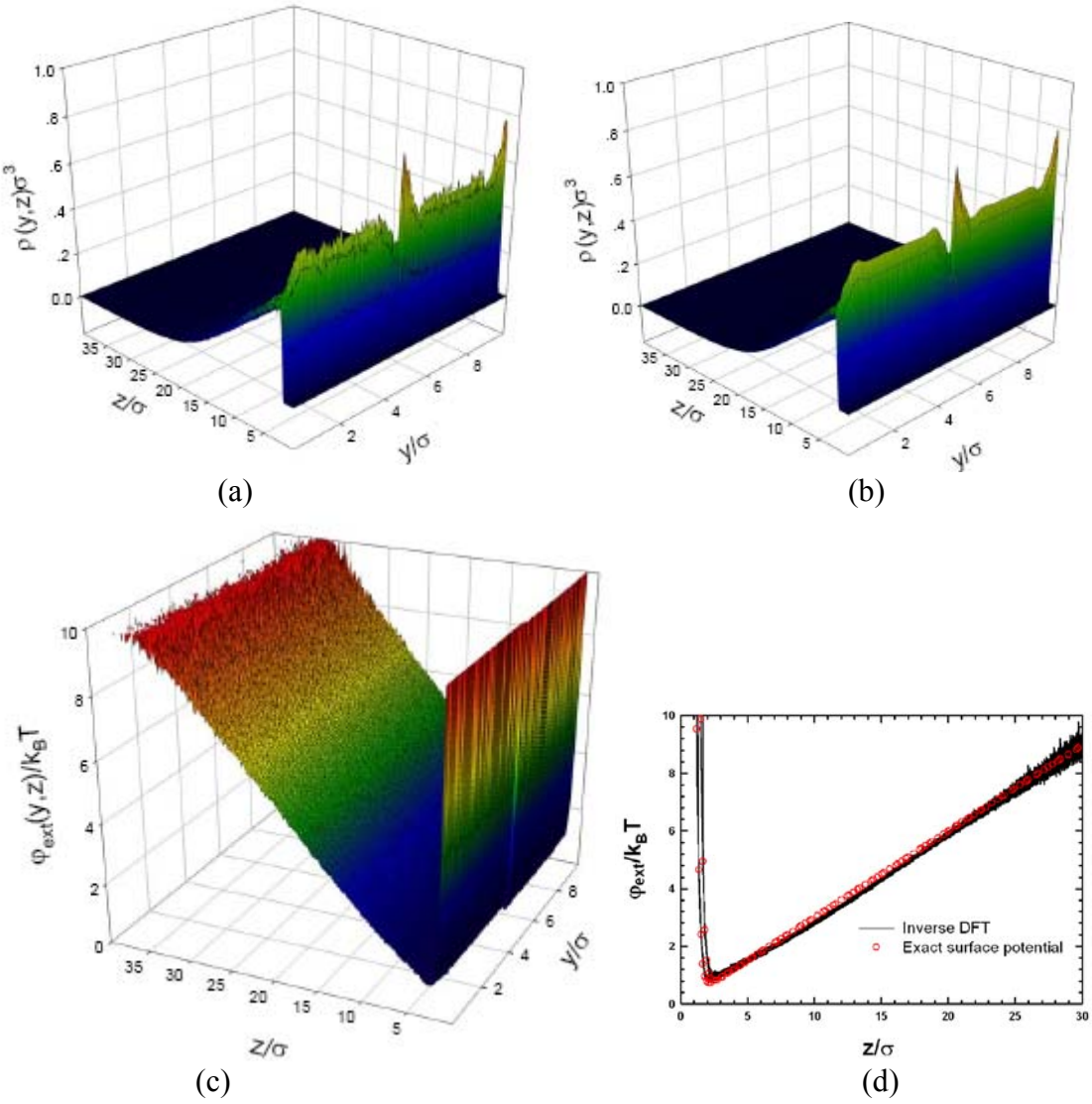

Figure 6.3. (a) Density profiles of hard particle near a screened electrostatic repulsive patterned surface with width 5σ:5σ from MC simulation. (For details on the potential parameters, see section 6.2.3) (b) Same as (a) but got from Eq. (6.1) with RY+VM closure combination. (c) Potential energy of a hard sphere particle near a screened electrostatic repulsive patterned surface with width 5σ:5σ, as obtained by inverse DFT (Eq. 6.2) using (a) as input. (d) Side view in z direction only for inverse DFT potential compared with exact surface potential. The open circles (O) are exact surface potential, while the solid lines (—) are inverse DFT result.

6.4.3 Screened electrostatic colloids on a gold-glass and gold-gold pattern surface

Fig. 6.4a shows an example of silica colloids diffusing over a glass surface with gold patterns by Wu *et al*.[136] Fig. 6.4b shows potential energy profile without gravity part in Fig. 6.4a though Eq. (6.13) with parameters described in Table 6.2.

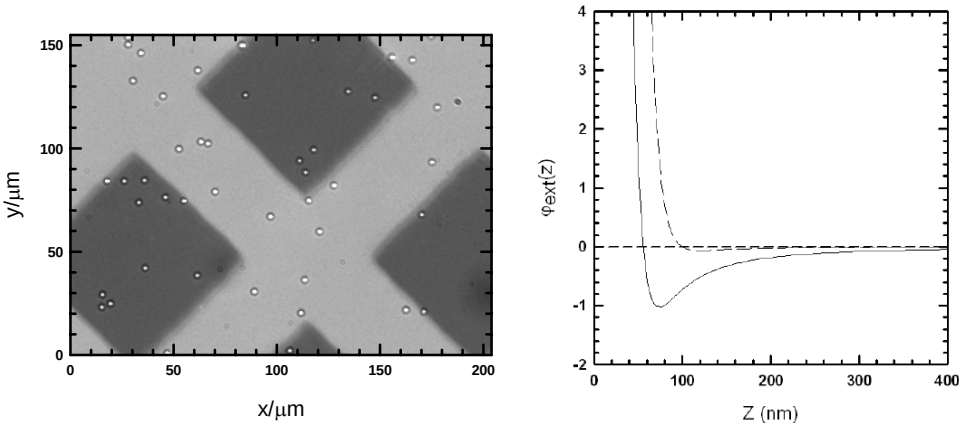

(a) (b)

Figure 6.4.[136] (a) Transmitted light CCD image of 2.34 μm silica colloids electrostatically levitated in aqueous 1mM NaCl above 75 μm x 75 μm x 10 nm (*l* x *w* x *h*) Au square films separated by 40 μm bare glass regions. Au films appear darker than uncoated glass. (b) Average potential energy profiles for 2.34 μm silica colloids interacting with bare glass (--) and 10 nm Au films (—) in aqueous 1mM NaCl (a). Main plot shows particle-surface potentials without gravitational potential.

Before the study of silica colloidal particles self-assembly on patterned gold surface by DFT, we first did forward analysis for silica particles on planar homogeneous gold surface (using the solid line in Fig. 6.4b for surface potential) as what we did in Section 4, since we did not study DLVO screened electrostatic repulsion + retarded van der Waals (vdW) attraction surface potential before. To test the bin width effect to both MC and DFT density profiles due to the short range vdW attraction, we range the bin width form 0.05σ to 0.005σ for both MC simulation and DFT calculation. As we seen

from Fig. 6.5a, DFT does a quite good job in predicting the density profile compared with MC even for the contact part as in Fig. 6.5b. Fig. 6.5b shows the contact density increase as the bin width decrease from 0.05σ to 0.005σ for both MC and DFT. To determine the maximum bin width for density profile, we performed the highest peak predictions. We picked up three points that closest to the point, where the minimum external potential energy $\varphi_{ext}(\boldsymbol{r})$ happens; applied linear fit and extrapolated to get the highest peak. We will not stop the decrease of the bin width until the predicted highest peaks by two bin widths are very close to each other (less than 2% difference). Then we can conclude that the larger bin width between the two bin widths is small enough to represent the highest peak of density profile. In this work, we found bin width 0.01σ is good enough for both MC and DFT. Then we use this bin width 0.01σ to study silica self assembly on gold-glass patterned surface.

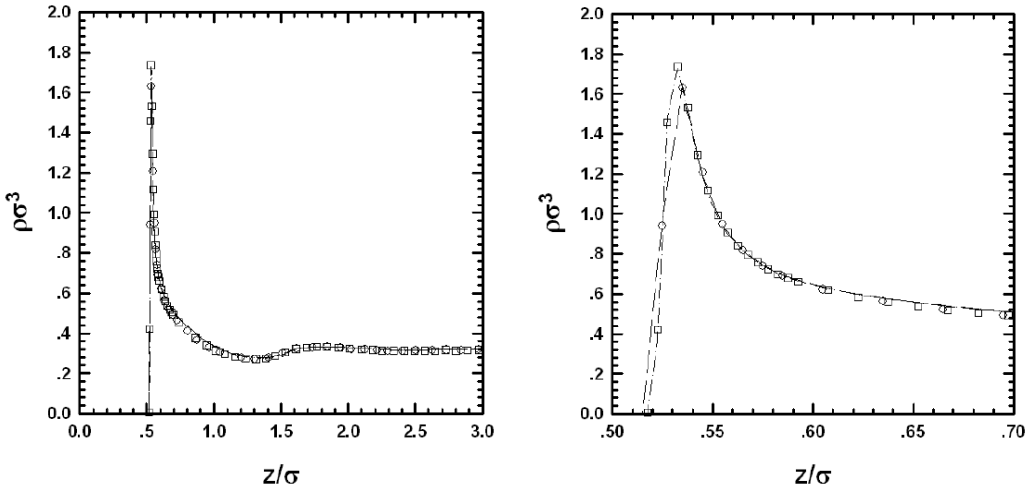

(a) (b)

Figure 6.5. (a) Density profile of silica particle near gold planar surface by MC and DFT (RY+VM closures) at $\rho_b\sigma^2$=0.32. The open circles (O) and squares (□) are MC simulation results with bin width 0.01σ and $0.005\ \sigma$ respectively. The dash (--) and dash-dot (- · -) are DFT results with bin width $0.01\ \sigma$ and $0.005\ \sigma$ respectively. (b) Same as (a) but focus on contact part.

Fig. 6.6a and 6.6b also show the very good agreement between MC and DFT. Fig. 6.6c shows the inverse potential energy and error of prediction can also be seen in Fig. 6.6d is less than $0.1k_BT$ for silica particle on gold-glass patterned surface.

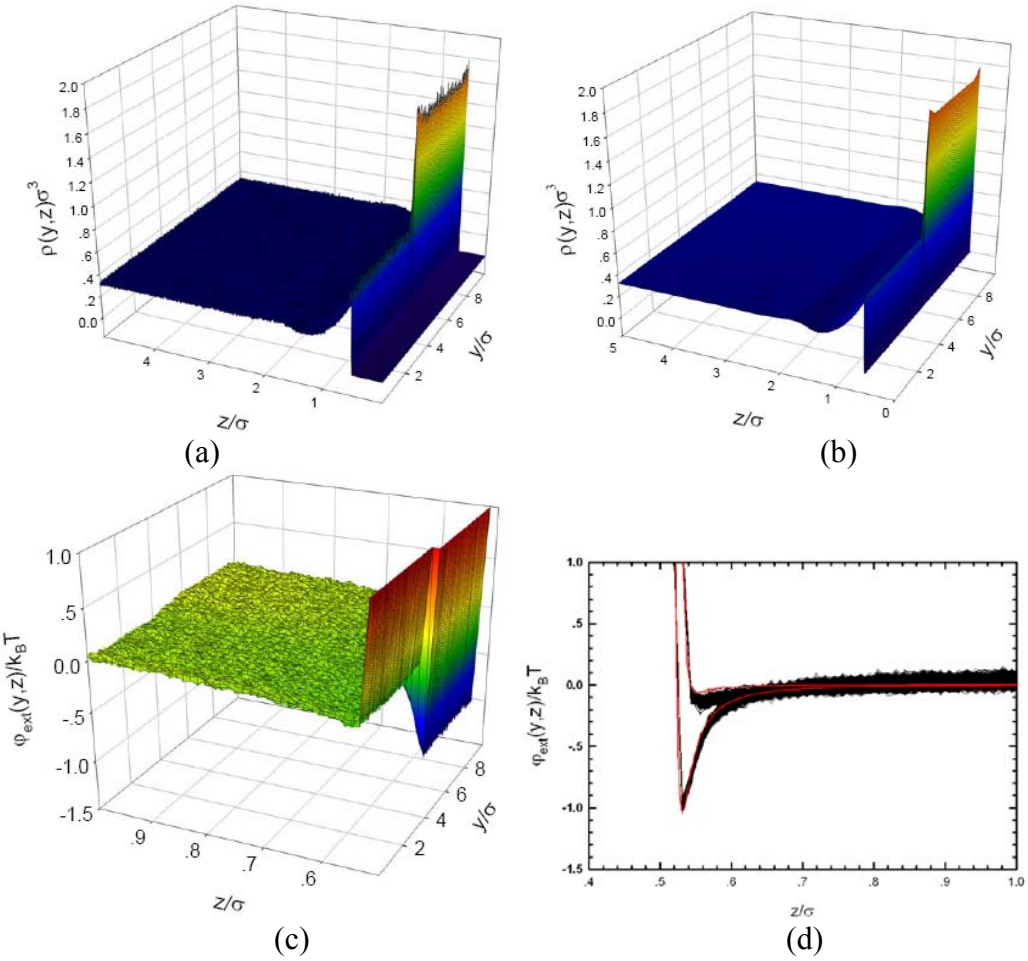

Figure 6.6. (a) Density profile of silica particle with DLVO screened electrostatic repulsive near gold patterned surface width 5σ:5σ in y direction by MC at $\rho_b\sigma^2$=0.32. (b) Same as (a) but got from DFT with RY+VM closure combination. (c) Potential energy of silica particle with DLVO screened electrostatic repulsive near gold patterned surface width 5σ:5σ in y direction by inverse DFT. (d) Side view in z direction only for inverse DFT potential compared with exact surface potential. The red solid are exact surface potential, while the black solid lines are inverse DFT result.

Fig. 6.7a and 6.7b also show the very good agreement between MC and DFT. Fig. 6.7c shows the inverse potential energy and error of prediction can also be seen in Fig. 6.7d is less than $0.2k_BT$ for silica particle on gold-gold patterned surface.

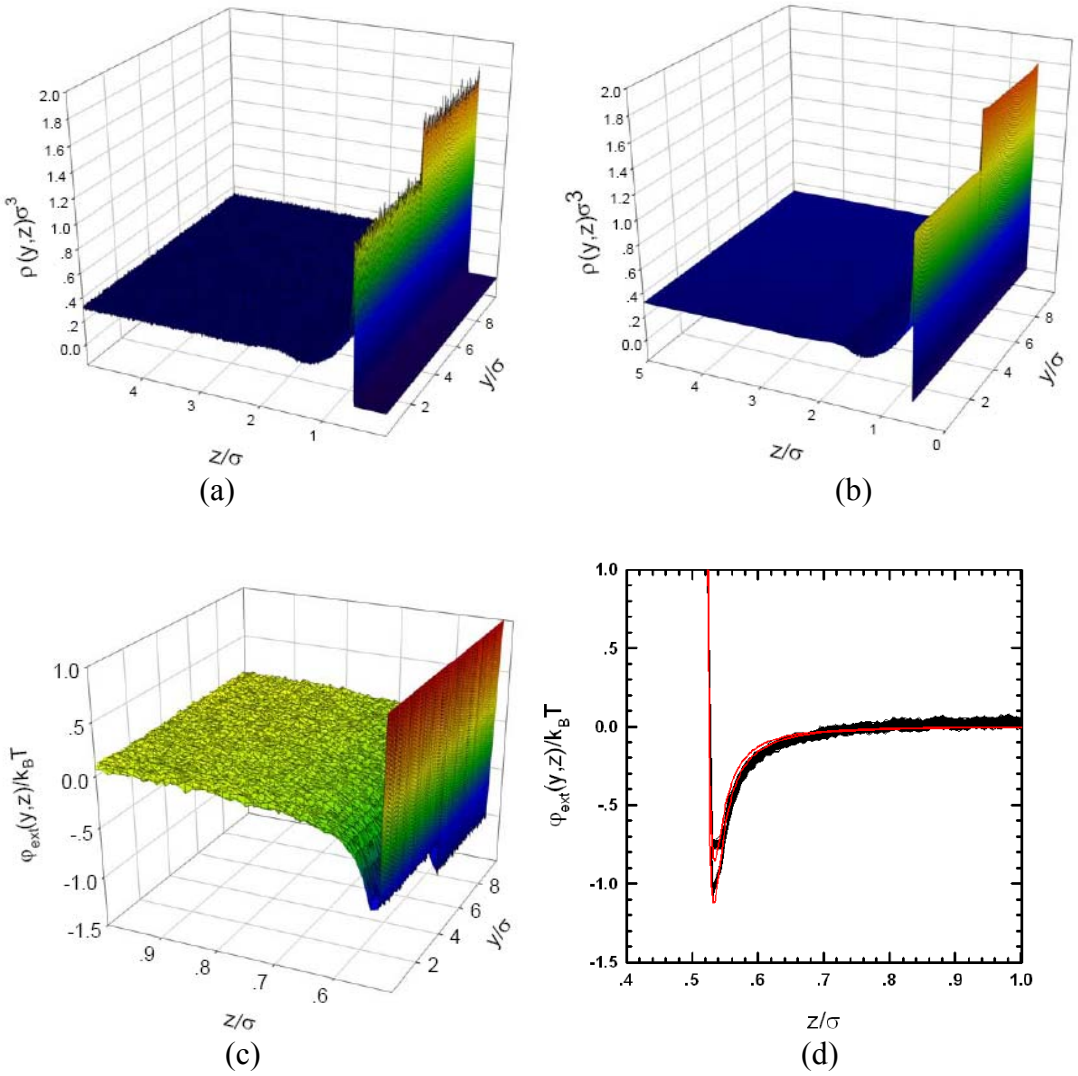

Figure 6.7. (a) Density profile of silica particle with DLVO screened electrostatic repulsive near gold-gold patterned surface width 5σ:5σ by MC at $\rho_b\sigma^2$=0.32. (b) Same as (a) but got from DFT with RY+VM closure combination. (c) Potential energy of silica particle with DLVO screened electrostatic repulsive near gold-gold patterned surface width 5σ:5σ by inverse DFT. (d) Side view in z direction only for inverse DFT potential compared with exact surface potential. The red solid are exact surface potential, while the black solid lines are inverse DFT result.

6.5 Conclusions

The DFT formulation of ZR was extended into colloidal self-assembly on patterned surface to obtain equilibrium density profile and particle-surface potentials with high accuracy. We found the entropy effect for equilibrium density profile and this may lead to various interesting and dynamic microstructure formation such as nanowire; we expect the inverse analysis should be useful for microscopy experiment such as confocal scanning laser microscope (CSLM) or Diffusing Colloidal Probes Microscopy (DCPM) to measure colloidal particle interaction with patterned surface such as biomolecular (e.g. DNA, proteins) arrays. The inverse analysis is much faster than forward analysis and can be done within several minutes on regular PC. The accuracy of the predictions depended on the bulk particle density, potential well depth and the choice of DFT closure relationships. Results for different cases we studied demonstrated the RY+VM combination of closures is a good general choice. This closure combination should produce acceptable results (< 0.1 k_BT maximum deviation from true potential) at low densities ($\rho_b\sigma^3$<0.3) across the different colloidal interaction types without gravity; while for colloidal self-assembly on patterned surface under gravity, RY+VM combination of closures produce acceptable results (< 0.3 k_BT maximum deviation from true potential) at $\rho_{\text{total}}\sigma^3$=0.1, k^{-1}=333nm, pre-factor=1554, and diameter=1.58μm, $(4/3)\pi a^3\Delta\rho g$=0.35 $k_BT/\mu m$. Higher densities are still problematic and will be the focus of future work, as will application of the theory to actual experimental data. High gravitational potential on both chemically and physically pattern will cause DFT failure and we extend 3D DFT to 2D DFT to solve this issue in next section because we simplify sphere shaped colloidal particles to disk shaped colloidal particles.

7. INTERFACIAL COLLOIDAL SELF-ASSEMBLY ON PATTERNED SURFACES

7.1 Synopsis

In this section we continue our work on templated colloidal self assembly but specific to sub-monolayer interfacial concentrations, which cannot be accurately described by three-dimension DFT due to very strong gravity. We successfully simplified the three-dimension DFT to two-dimension DFT and our results for different cases studied show very high accuracy in both forward and inverse analysis with Monte Carlo simulation and exact external potential respectively.

7.2 Introduction

Integrating nano- and micro- scale components into more complex structure autonomously and reversibly is a key challenge for current biotechnology and is consider promising as an enabling process to numerous emerging technologies.[143] Thus, the fundamental understanding of thermal motion, particle interactions, and template features and so on provide the strategies to fabricate equilibrium and dynamic colloidal microstructures on energetic templates. Although a numbers of studies have been reported claimed as “templated colloidal self-assembly”, it is not always true since the process of templated colloidal self-assembly should be autonomous and reversible for colloids to form equilibrium and dynamic structures on energetic patterned surfaces without the external control such as electric and magnetic fields. The competition between entropy and potential energy should lead to the formation of various ordered structures such as crystal.[142] Thus, the random Brownian motions for colloidal particle should not only provide the understandable motivation that involve assembly but also as the natural motion essential to dynamic self-assembly processes.[144]

The state-of-the-art for "imaging" physical,[4,38] and chemical[135,145] patterned surfaces is Scanning probe techniques, which can not resolve weak interaction due to mechanical limitations that involve monitoring the deflection of a cantilever tip.

Therefore, it cannot measure the weak forces that are essential for colloidal assembly. Bahukudumbi and Bevan[144] proposed a method using called Brownian Colloidal Probes (BCP) to image energy landscapes on physically patterned surface. The advantage of BCP over scanning probe techniques is that it exploits Brownian motion as a natural gauge of k_BT-scale energy landscape features.[144] The significance of BCP is that it intended to use very same colloidal particle to be both imaging probes and build blocks in templated self-assembly on patterns.[144]

As far as we know, only quite a few studies investigated the truly templated self-assembly, i.e. without external control, until now. The studies about truly thermodynamically reversible colloidal self-assembly are even less. Reversible means the self-assembly process can be repeated by different initially disorganized colloidal particles and completely disassembled tuning a thermodynamic variable. For example, the strong attractive interactions used in current templated colloid assembly to irreversibly deposit the colloid on surfaces are clearly not reversible; those generally form disordered aggregates or gels instead of organized structures – crystals.

Bahukudumbi and Bevan[144] investigated inhomogeneous quasi-2D colloidal fluids on patterned surface with k_BT-scale energy landscapes. Inverse Monte Carlo simulations were applied to "image" three dimensional energy landscapes using optical microcopy measured two dimensional Brownian colloidal probe trajectories of colloidal probes Brownian motion. Their results showed an excellent agreement with Atomic Force Microscopy measured surface topographies. As a result, they provide a new imaging paradigm in addition to providing equilibrium and dynamic information important to the design and control of colloidal self-assembly on patterns.[144]

Although density function theory (DFT) has been applied with success to understand the phase and properties of interfacial fluids and soft materials such as surface tension, gas adsorption, wetting transition, freezing and melting transition, phase behavior of liquid crystal, properties of polymers and composites,[11] the application of DFT to inhomogeneous fluids and phase transitions of such fluids next to patterned surfaces is still in its infancy. In Section 4 and 5, we explored an inversion of DFT where

we calculated the external potential field from a known density profile in an inhomogeneous fluid interacting with a planar surface with or without gravity. In Section 6, we studied the 3 dimensional colloidal self-assembly on patterned surface with or without gravity.

In this section, we investigated the nonlocal closure-based 2 dimensional DFT of ZR[45] to image energy landscape features associated with physically patterned substrates. To ensure the successful application of this 2D DFT framework to analyze inhomogeneous qusi 2D colloidal fluids, we study, we studied the following cases: hard disk particles near a hard wal, hard disk particles inside a hard cavity, hard disk particles around a hard disk object, screened electrostatic particles interacting with a parabolic potential well, screened electrostatic particles on a square well, screened electrostatic particles on patterned parabolic potential wells, and equilibrium partitioning number for Polystyrene (PS) colloidal self-assembly on gold patterned. Also we proposed a new closure inspired by the work of Zhou *et al.*[74] and demonstrate it's successful applications for the cases we studied.

7.3 Theory

7.3.1 Forward and inverse analysis

Here we gave the equations for the forward and inverse analysis for DFT. For details about forward and inverse analysis, please see Section 2.3.3.

Forward analysis:

$$\rho(\mathbf{r}) = \rho_b \exp\left\{\begin{array}{l} -\beta\varphi_{ext}(\mathbf{r}) + \int d\mathbf{r}_1 \left(\rho(\mathbf{r}_1) - \rho_b\right) C_0^{(2)}(\mathbf{r}, \mathbf{r}_1; \rho_b) \\ +B\left[\int d\mathbf{r}_1 \left(\rho(\mathbf{r}_1) - \rho_b\right) C_0^{(2)}(\mathbf{r}, \mathbf{r}_1; \rho_b)\right] \end{array}\right\} \tag{7.1}$$

Inverse analysis:

$$\begin{aligned} &\beta\varphi_{ext}(\mathbf{r}) = -\ln\left[\frac{\rho(\mathbf{r})}{\rho_b}\right] + \\ &\int d\mathbf{r}_1 \left(\rho(\mathbf{r}_1) - \rho_b\right) C_0^{(2)}(\mathbf{r}, \mathbf{r}_1; \rho_b) + B\left[\int d\mathbf{r}_1 \left(\rho(\mathbf{r}_1) - \rho_b\right) C_0^{(2)}(\mathbf{r}, \mathbf{r}_1; \rho_b)\right] \end{aligned} \tag{7.2}$$

7.3.2 3D density function theory simplified to 2D density functional theory

In our previous sections, all the DFT calculations are three dimensional, and were applied to spherical colloidal particles. For those calculations, spherical coordinates were used as described in Section 3.3. For interfacial colloidal assembly on patterned surface, we simply transform the spherical shaped colloids to hard discs. Equations (7.1) and (7.2) are applicable for 2D disk system; ***r*** is now a position vector in the polar coordinate system.

7.3.3 Closures

Five of the closures employed in this work have analytical expressions for B[γ],

Percus-Yevick (PY):[65]

$$B[\gamma(\mathbf{r})] = \ln(1+\gamma(\mathbf{r})) - \gamma(\mathbf{r}) \tag{7.3}$$

Verlet-modified (VM):[67]

$$B[\gamma(\mathbf{r})] = -\gamma(\mathbf{r})^2 / 2\left[1 + 0.8\gamma(\mathbf{r})\right] \tag{7.4}$$

Hypernetted chain (HNC):[10]

$$B\left[\gamma(\mathbf{r})\right] = 0 \tag{7.5}$$

and Zhou-Hong-Zhang (ZHZ):[131]

$$B\left[\gamma(\mathbf{r})\right] = -0.5\gamma(\mathbf{r})^2 \exp\left(-\alpha\gamma(\mathbf{r})\right) \tag{7.6}$$

For the calculation of α, please see Section 2.2.3.6. We modify the ZHZ closure as follows:

$$B\left[\gamma(\mathbf{r})\right] = -0.5\alpha\gamma(\mathbf{r})^2 \exp\left(-0.05\gamma(\mathbf{r})\right) \tag{7.7}$$

where α can be obtained by thermodynamics consistency, thus bulk modulus calculated from the virial equation B_p is equal to that calculated from the compressibility equation B_c. This is referred to as the LBF closure in this dissertation. Similar to the ZHZ closure,

α is a function of bulk density ρ_b. We use the same method as in that of ZHZ closure to obtain α, as in Section 2.2.3.6.

Another closure employed in this section is the Rogers-Young (RY) [72] which has no analytical expression for B[γ], they gave the equation of $g(r)$

$$g(r) = \exp\left[-\beta u(r)\right]\left[1 + \frac{\exp\left[\gamma(r) f(r)\right] - 1}{f(r)}\right] \tag{7.8}$$

where $f(r)$=1-exp(-αr) and α is an adjustable parameter determined by thermodynamic consistency. For the calculation of α, please refer to Section 2.2.3.5. For the numerical function between $B[\gamma(r)]$ and $\gamma(r)$, please read Section 2.2.3.5 and Fig. 4.1

7.3.4 Model Potentials

In this section, two different common colloidal potentials were investigated, namely hard disks, hard disk core repulsion and Derjaguin-Landau-Verwey-Overbeek (DLVO) screened electrostatic repulsion for particle and particle interaction $u(\mathbf{r})$. Four different potentials were used for particle-surface potential $\varphi_{ext}(\mathbf{r})$, namely hard wall, hard cavity, parabolic well potential, and square well potential.

7.3.4.1 Particle-particle potential models

The first model is hard disks of diameter σ with a potential given by:

$$\beta u(r) = \begin{cases} \infty, & r < \sigma \\ 0, & r \geq \sigma \end{cases} \tag{7.9}$$

The second model is a hard disk core repulsion and DLVO screened electrostatic potential:[111]

$$\beta u(r) = \begin{cases} \infty, & r < \sigma \\ B_{pp} \exp\left[-\kappa\left(r - \sigma\right)\right], & r \geq \sigma \end{cases} \tag{7.10}$$

where B_{pp} is a pre-factor that is a function of colloidal surface charge and κ^{-1} is the Debye length. In this section, B_{pp} =2583.2 k_BT and κ^{-1}=89nm.

7.3.4.2 Particle-surface potential models

The first was a hard wall:

$$\beta\varphi_{ext}(z)=\begin{cases}\infty, & z<\sigma/2\\ 0, & z\geq\sigma/2\end{cases} \tag{7.11}$$

This external field was created by a single planar surface, yielding inhomogeneity in the *z* direction only.

The second was a hard cavity:

$$\beta\varphi_{ext}(\mathbf{r})=\begin{cases}0, & \mathbf{r}<R\\ \infty, & \mathbf{r}\geq R\end{cases} \tag{7.12}$$

where R is the diameter of hard cavity. The third model was a parabolic potential well:

$$\beta\varphi_{ext}(\mathbf{r})=\begin{cases}a\mathbf{r}^2-b, & \mathbf{r}<\sqrt{b/a}\\ 0, & \mathbf{r}\geq\sqrt{b/a}\end{cases} \tag{7.13}$$

where *a* can *b* are potential parameters to determine the potential well depth and shape.

The final model is a square well potential:

$$\beta\varphi_{ext}(\mathbf{r})=\begin{cases}\varepsilon, & \mathbf{r}<\lambda\sigma\\ 0, & \mathbf{r}\geq\lambda\sigma\end{cases} \tag{7.14}$$

where ε is the potential depth and λ is the reduced range of potential width.

7.4 Results and Discussions

For each model, we initially solve OZ equation with a chosen closure using the numerical method described in Section 3.2.1. Following the general approach described in Section 4, we first determine the best closure from the list of different closures for the bulk system by comparing the $g(r)$ with that of MC simulations. This reduces the number of closure combinations for DFT. Out calculations show that the RY is still the best closure for 2D bulk system, similar to our observations with 3D colloidal systems..

Therefore, for the forward and inverse DFT work, we test only six closure combinations: RY+PY, RY+VM, RY+HNC, RY+RY, RY+ZHZ, and RY+LBF. In the following results part, we listed the best two closures combinations out of six.

7.4.1 Hard disk particles near hard wall

Fig. 7.1a shows density profiles of hard disk particles near hard wall at bulk density $\rho_b\sigma^2$=0.52 from MC and DFT with very good agreement with each other. RY+VM slightly overpredicts the contact density while RY+LBF underpredicts; RY+LBF and RY+VM have similar good behaviors compared with MC results besides the contact part. For the inverse DFT, RY+VM and RY+LBF are quite good with error less than $0.05k_BT$.

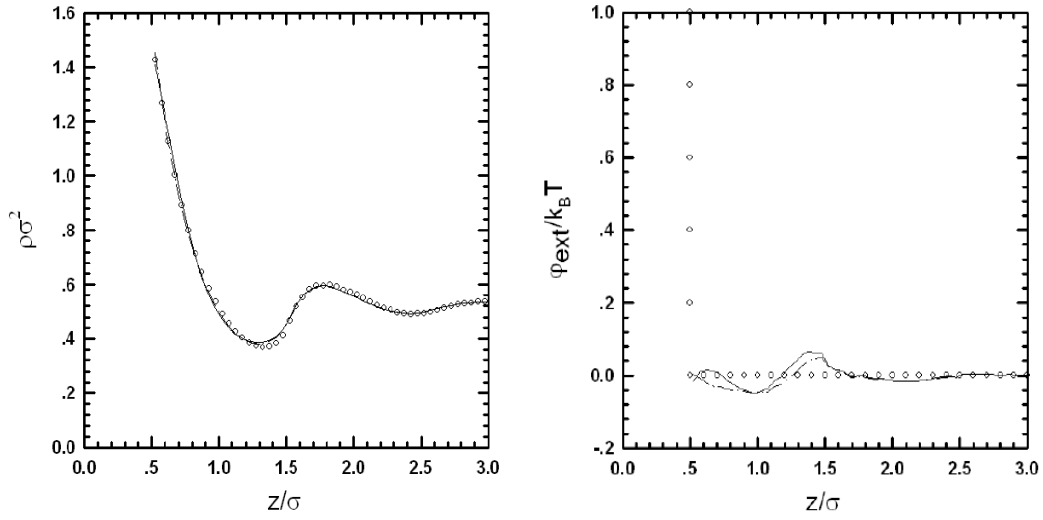

(a) (b)

Figure 7.1. (a) Density profile of hard disk particles near hard wall by MC and forward DFT at $\rho_b\sigma^2$=0.52. The open circles (O) are MC simulation result. The solid (—) and dash-dot (- · -) are RY+LBF and RY+VM closures combination respectively. (b) Potential energy of hard disk particles interacting with a hard wall at $\rho_b\sigma^2$=0.52 as obtained by inverse DFT, compared to the true potential denoted by open circles (O). The solid (—) and dash-dot (- · -) are RY+LBF and RY+VM closures combination respectively.

7.4.2 Hard disk particles inside hard cavity

Fig. 7.2a shows density profiles of hard disk particles inside hard cavity at bulk density $\rho_b\sigma^2$=0.6 from MC and DFT with cavity diameter R=5σ. RY+VM and RY+LBF show very similar density profile except for the contact part, where RY+LBF is better than RY+VM with less overpredicted errors. For the inverse DFT, the maximum errors cause by RY+VM and RY+LBF are less than 0.2k_BT with a local minimum near z/σ= 3.5. RY+LBF is better than RY+VM in predicting the contact potential energy, which is consistent with forward calculation.

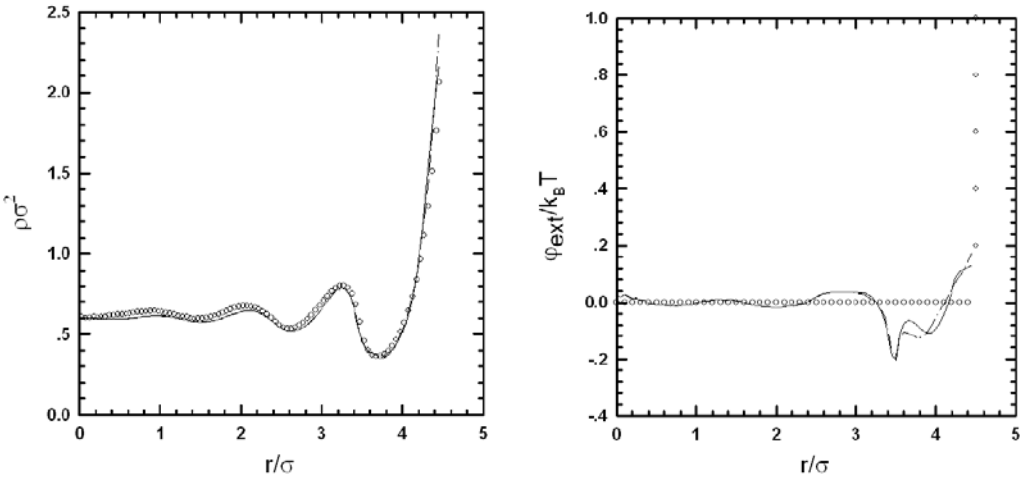

(a) (b)

Figure 7.2. (a) Density profile of hard disk particles inside hard cavity by MC and forward DFT at $\rho_b\sigma^2$=0.6. The open circles (O) are MC simulation result. The solid (—) and dash-dot (- · -) are RY+LBF and RY+VM closures combination respectively. (b) Potential energy of hard disk particles inside hard cavity at $\rho_b\sigma^2$=0.6 as obtained by inverse DFT, compared to the true potential denoted by open circles (O). The solid (—) and dash-dot (- · -) are RY+LBF and RY+VM closures combination respectively.

7.4.3 Hard disk particles around hard disk object

In this case, a stationary hard disk with different size sits in the middle of simulation box. Fig. 7.3a shows density profiles of hard disk particles around stationary hard disk object (diameter=1.0σ) at bulk density $\rho_b\sigma^2$=0.6 from MC and DFT. RY+VM and RY+LBF show very similar density profile except for the contact part, where RY+LBF is better than RY+VM with less overpredicted errors. For the inverse DFT, RY+VM and RY+LBF are quite good with error less than 0.1k_BT. RY+LBF is better than RY+VM in contacting region, while RY+VM is better than RY+LBF in overall.

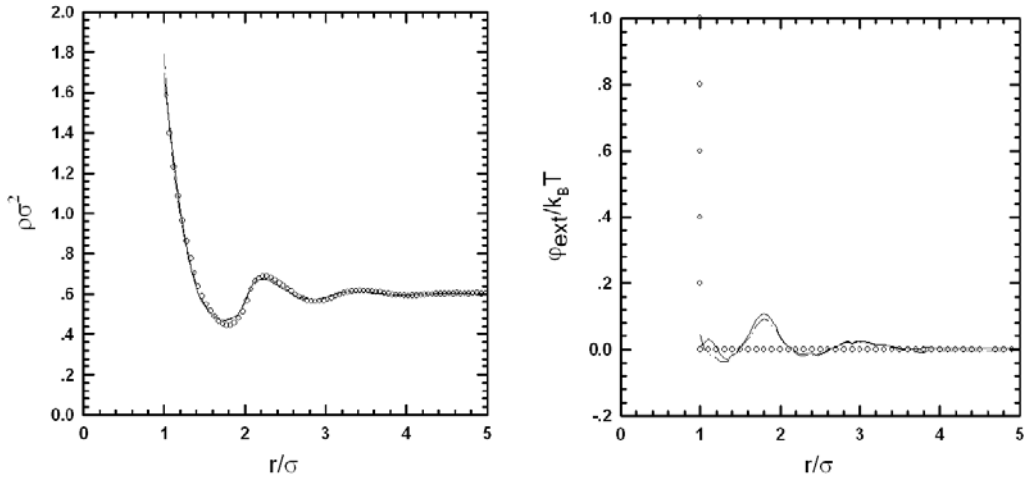

(a) (b)

Figure 7.3. (a) Density profile of hard disk particles around hard disk object by MC and forward DFT at $\rho_b\sigma^2$=0.6. The open circles (O) are MC simulation result. The solid (—) and dash-dot (- · -) are RY+LBF and RY+VM closures combination respectively. (b) Potential energy of hard disk particles around hard disk object at $\rho_b\sigma^2$=0.6 as obtained by inverse DFT, compared to the true potential denoted by open circles (O). The solid (—) and dash-dot (- · -) are RY+LBF and RY+VM closures combination respectively.

Percus identity[94] for the special case of an external field generated by a single particle of the fluid species placed at the origin gives $\rho(r)=\rho_b g(r)$. So if the stationary hard disk object diameter is equal the hard disk, the $\rho(r)$ and $g(r)$ should follow Percus

identity. Fig. 7.4a shows the density profiles divided by bulk density ρ_b of hard disk around stationary disk objects by MC and DFT and g(r) by MC simulation of bulk hard disk at same ρ_b. As we seen form Fig. 7.4a, two MC simulation are identical to each other, which follows the Percus identity. RY+VM result is good agreement except slightly overpredicts the first peak of g(r).

For the stationary disk objects, its diameter is adjustable. So when we increase it so large that it can be simplified to planar wall. In Fig. 7.4a, we study how large is it enough to make such a simplification. Fig. 7.4b shows that density profile of hard disk particles around the hard disk objects is getting close to that of hard disk near hard wall as we increase the disk object diameter. From Fig. 7.4b we can conclude that 5σ is a good diameter to make such simplification.

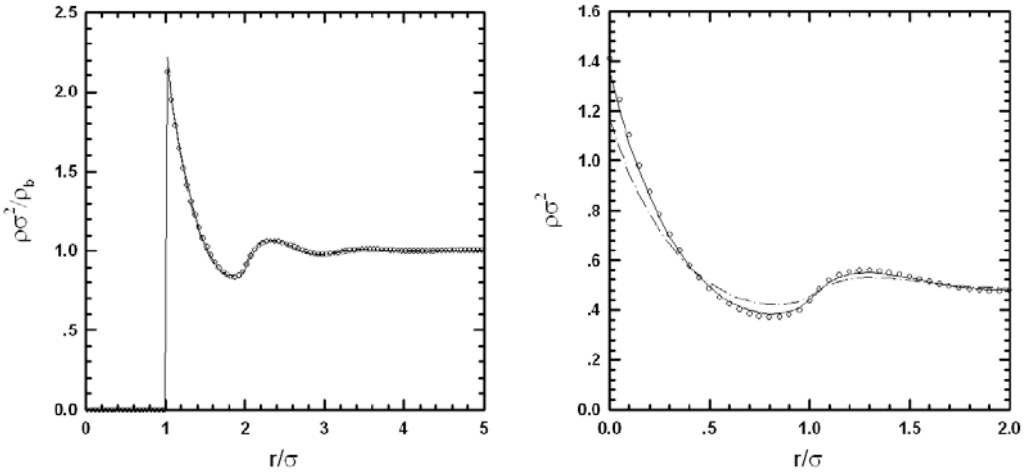

(a) (b)

Figure 7.4. (a) Density profiles divided by bulk density of hard disk particle around hard disk object by MC and forward DFT at $\rho_b\sigma^2$=0.5 and MC $g(r)$ result. The open circles (O) are MC $g(r)$. The solid (—) and dash-dot (- · -) are MC and RY+VM closure combination respectively. (b) Density profile of hard disks particle around hard disk object at $\rho_b\sigma^2$=0.5 comparing with density profile of hard disk particles near hard wall denoted by open circles (O). The solid (—) and dash-dot (- · -) are RY+VM closures combination with hard disk objects diameter=5σ and 1σ respectively.

7.4.4 Screened electrostatic particles on a parabolic potential well

As we stated in the introduction, the objective of this section is to "image" the three dimensional energy landscape of physically patterned surface by inverse DFT instead of inverse MC.[144] The inverse MC simulations are computationally more expensive when compared to an integral equation theory based framework method like inverse DFT. This provides the motivation to use inverse DFT to interpret experimentally measured distribution functions as potential energy landscape features Fig. 7.5 shows silica colloid self assembly on physically pattern by Bahukudumbi and Bevan.[144] While Fig. 7.5a shows silica colloid self assembly on physically patterned surface by Fig. 7.5b[144] shows the height image of patterned surface by inverse MC; Fig. 7.5c[144] shows energy landscape cross section from 7.5b.

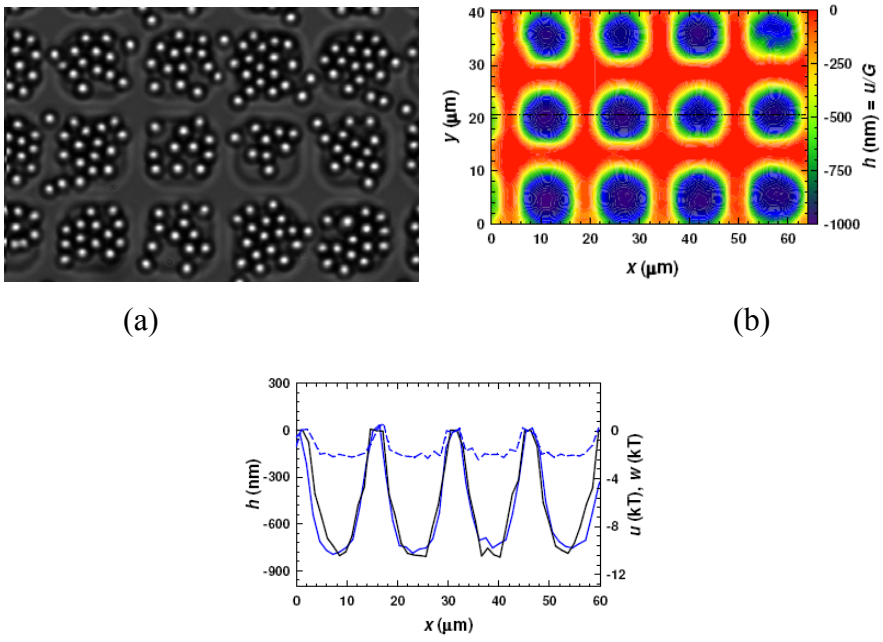

(a) (b)

(c)

Figure 7.5.[144] (a) Transmitted light CCD image of 2.20μm silica colloids above 13μm x 13μm x 800nm (*l* x *w* x *h*) features separated by 4μm. (b) The height image of patterned surface measure by inverse MC. (c) Energy landscape cross section from (b). Solid back, solid blue and dash blue line denote the measurement by AFM, calculation by inverse MC, and Boltzmann equation inversion respectively.

Before the study of multiple patterned surfaces, we investigated the single well, which was placed into the center of simulation box with same potential as solid black line in Fig. 7.5(c) but with less attraction strength. Fig. 7.6a shows density profile of hard disk core repulsion and screened electrostatic repulsion particles around square well (with $\varphi_{ext}(\mathbf{r})=0.4616\mathbf{r}^2-4$ as in Eq. (7.13)) at bulk density $\rho_b\sigma^2=0.11$ from MC and DFT. RY+HNC can not correctly describe the structure inside potential well; while RY+LBF does a quite good job in predicting the density profile. As we seen from Fig. 7.6b for the inverse DFT, RY+LBF is quite good as well as in forward DFT with maximum error less than $0.1k_BT$. RY+HNC can not predict the potential profile correctly for well depth great than $-2k_BT$.

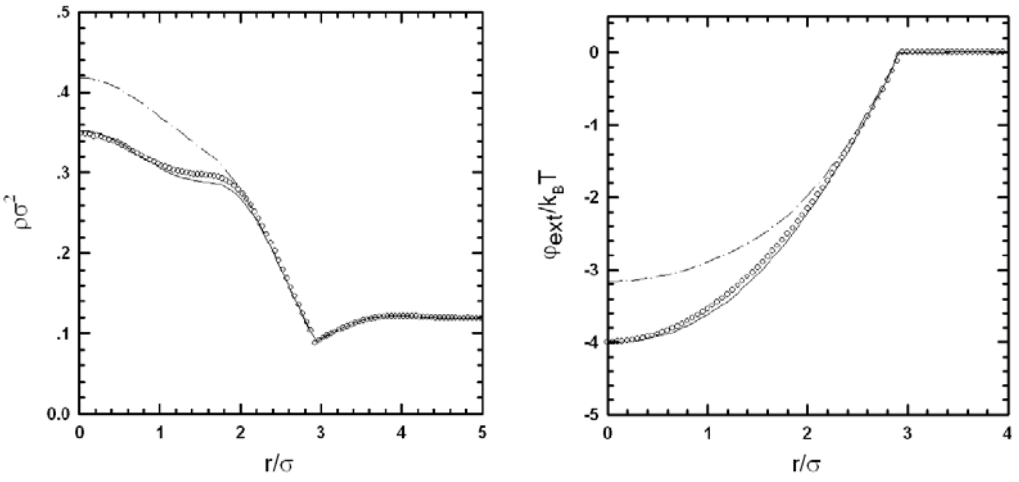

(a) (b)

Figure 7.6. (a) Density profiles of hard disk core repulsion and screened electrostatic repulsion particles around parabolic potential well (well depth = $-4k_BT$) by MC and forward DFT at $\rho_b\sigma^2=0.12$. The open circles (O) are MC results. The solid (—) and dash-dot (- · -) are RY+LBF and RY+HNC closure combination respectively. (b) Potential energy of hard disk core repulsion and screened electrostatic repulsion particles interacting with parabolic potential well at $\rho_b\sigma^2=0.12$ as obtained by inverse DFT, compared to the true potential denoted by open circles (O). The solid (—) and dash-dot (- · -) are RY+LBF and RY+VM closures combination respectively.

7.4.5 Screened electrostatic particles on a square well

Next we change the well potential type form parabolic to square well. Fig. 7.7a shows density profile of hard disk core repulsion and screened electrostatic repulsion particles around parabolic potential well (with λ=2.9 ε=-4 in Eq. (7.14)) at bulk density $\rho_b\sigma^2$=0.12 from MC and DFT. RY+HNC can not correctly describe the structure inside potential well; while RY+LBF does a quite good job in predict the density profile. As we seen from Fig. 7.7b for the inverse DFT, RY+LBF is quite good as well as in forward DFT with maximum error less than $0.1k_BT$. RY+HNC can not predict the potential profile correctly. We found that more particles stayed inside the patterned for square well potential than that of parabolic potential well after we integrating the density profile. This is consistence with potential type behind the physical structure. V shaped structure should hold less particles compared with square shaped well since there is more room for particle to move.

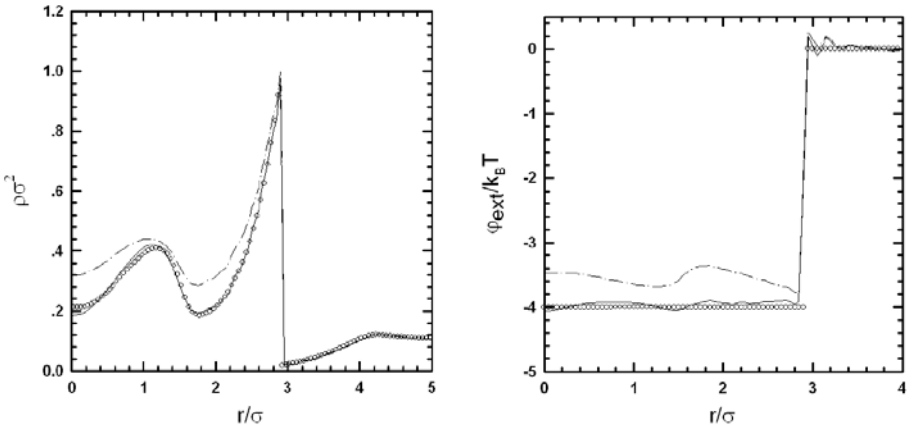

(a) (b)

Figure 7.7. (a) Density profile of hard disk core repulsion and screened electrostatic repulsion particles around square well (well depth = $-4k_BT$) by MC and forward DFT at $\rho_b\sigma^2$=0.11. The open circles (O) are MC results. The solid (—) and dash-dot (- · -) are RY+LBF and RY+HNC closure combination respectively. (b) Potential energy of hard disk core repulsion and screened electrostatic repulsion particles interacting with square well at $\rho_b\sigma^2$=0.11 as obtained by inverse DFT, compared to the true potential denoted by open circles (O). The solid (—) and dash-dot (- · -) are RY+LBF and RY+VM closures combination respectively.

7.4.6 Screened electrostatic particles on patterned parabolic and square well potential wells

After the successful work of single patterned surface with two types of surface potentials, we extend the work to patterned parabolic and square well potential wells. Fig. 7.8a and 7.8b show the 2d contour plot for density profile of hard disk core repulsion and screened electrostatic repulsion particles around patterned parabolic potential well by MC and DFT respectively at $\rho_b\sigma^2$=0.096. Fig. 7.8c shows the potential landscape of patterned parabolic potential. As we seen from 7.8d, inverse DFT is quite good comparing wit exact surface potential with error less than 0.1 k_BT. The issue of multiple-pattern surface is the interaction between patterns with each other. As we can see from Fig. 7.8a, 7.8b, 7.9a, and 7.9b, the density between two patterns are higher than bulk density due to the interaction between patterns. However, the inverse DFT can still correctly predicted the particle-surface potential for multi-pattern surfaces.

Next we studied similar work but using square well potential. Fig. 7.9a and 7.9b show the 2d contour plot for density profile of hard disk core repulsion and screened electrostatic repulsion particles around patterned parabolic potential well by MC and DFT respectively. Fig. 7.9c shows the potential landscape of patterned parabolic potential. As we seen from Fig. 7.9d, inverse DFT is good comparing with exact surface potential with error less than 0.4 k_BT.

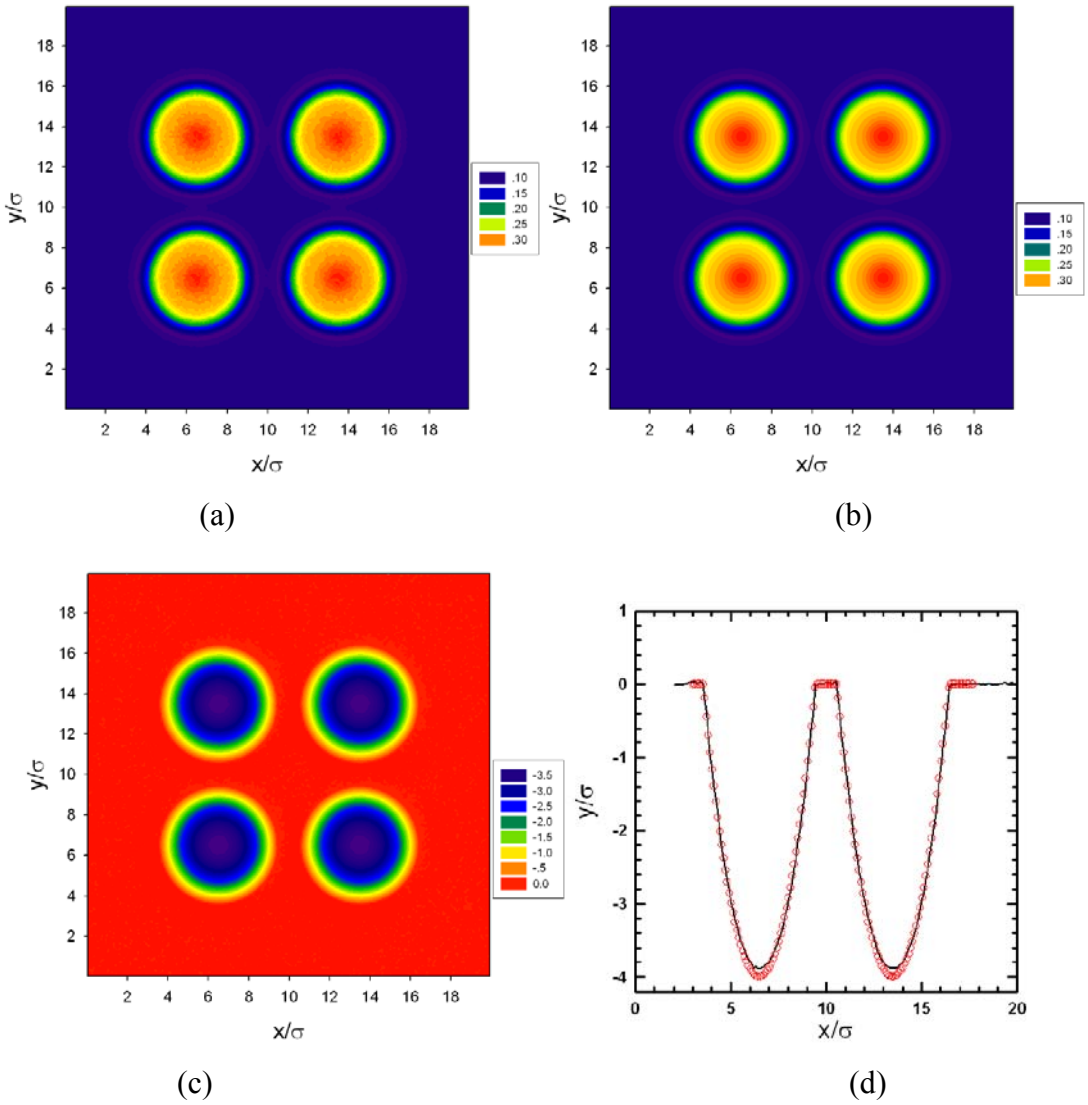

Figure 7.8. (a) Density profile of hard disk core repulsion and screened electrostatic repulsion particles around patterned parabolic potential well (well depth = $-4k_BT$) by MC at $\rho_b\sigma^2$=0.096. (b) Same as (b) but obtained by DFT. (c) Potential energy of hard disk core repulsion and screened electrostatic repulsion particles around patterned parabolic potential well (well depth = $-4k_BT$) by inverse DFT (Eq. 7.2) at $\rho_b\sigma^2$=0.096. (d) Energy landscape cross sections from (c). The open circles (O) are exact surface potential, while the solid lines (—) are inverse DFT result.

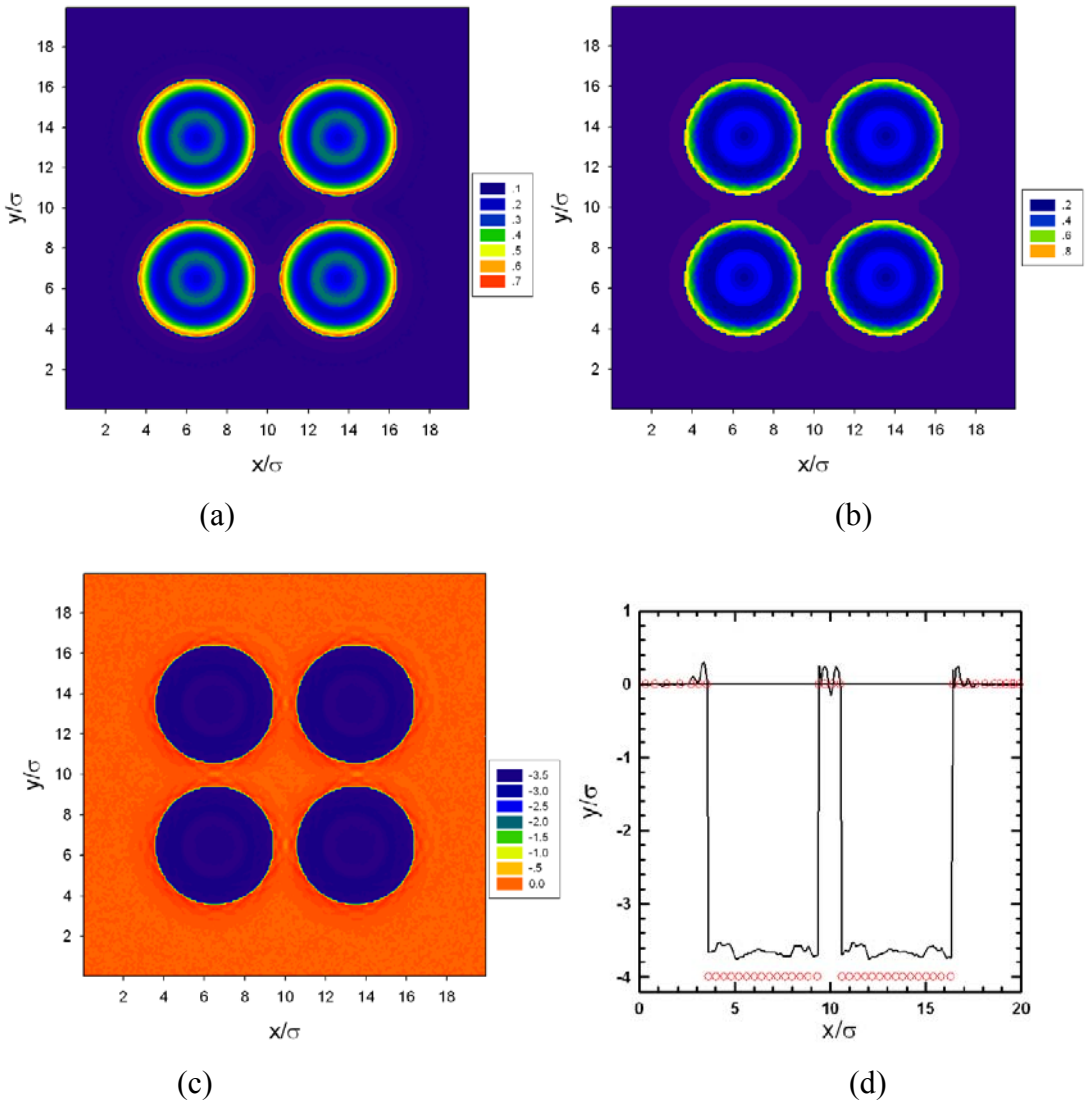

Figure 7.9. (a) Density profile of hard disk core repulsion and screened electrostatic repulsion particles around patterned square well potential well (well depth = $-4k_BT$) by MC at $\rho_b\sigma^2$=0.057. (b) Same as (b) but obtained by DFT. (c) Potential energy of hard disk core repulsion and screened electrostatic repulsion particles around patterned square well potential well (well depth = $-4k_BT$) by inverse DFT (Eq. 7.2) at $\rho_b\sigma^2$=0.057. (d) Energy landscape cross sections from (c). The open circles (O) are exact surface potential, while the solid lines (—) are inverse DFT result.

7.4.7 Equilibrium partitioning number of interfacial PS colloids over chemical patterns

Equilibrium partitioning number is defined by the average particles area fraction outside the pattern to that of inside pattern (the darker area in Fig. 7.10a). Due to the homogeneity of gold layer thickness, the potential landscape is a constant across the pattern such as darker area. Thus we can use the square well potential as in Eq. (7.14) to describe the potential difference ε between two gold layers with different.

We implement both MC and DFT to calculate the Equilibrium partitioning number for silica colloidal on patterned as a function of total particle area fraction ϕ and potential difference ε. Since the pattern is a square and density is uniform across the pattern except for the interface part as we seen from Fig. 7.10c, we can simply the calculation to one dimension. DFT, thus we calculate the density of center of pattern in either one of the direction.

Fig. 7.10b shows the density profile on pattern gold with well depth $-2k_BT$ and bulk density $\rho_b\sigma^2$=0.3 at thinner gold pattern. As we seen form 7.10b, RY+HHC tends to overpredict the density profile inside the darker pattern, while RY+ZHZ underpredicts the density profile. Since the equilibrium partitioning number is defined by average area fraction of lighter pattern to that of darker pattern, the equilibrium partitioning number will less than 1 unless the potential difference between two patterns equals zero. Thus, RY+HNC will underpreditcs the equilibrium partitioning number and RY+ZHZ will overpredicts. While RY+LBF can correctly predict the equilibrium partitioning number compared with MC.

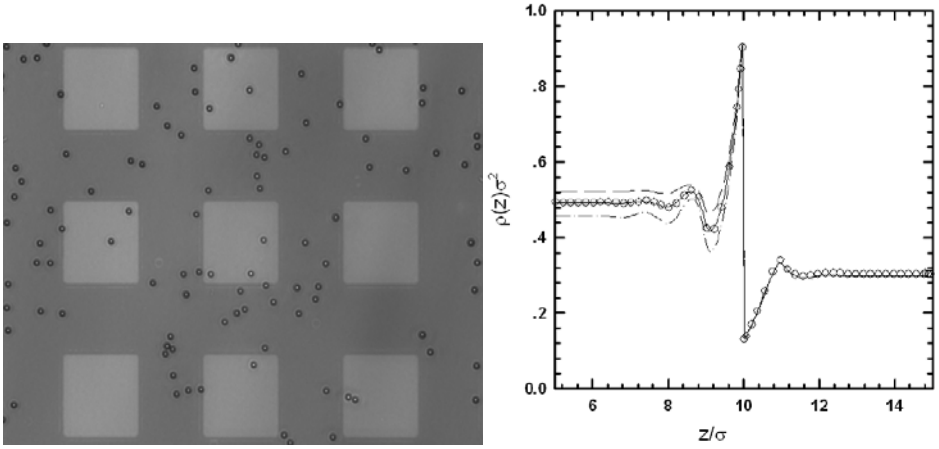

(a) (b)

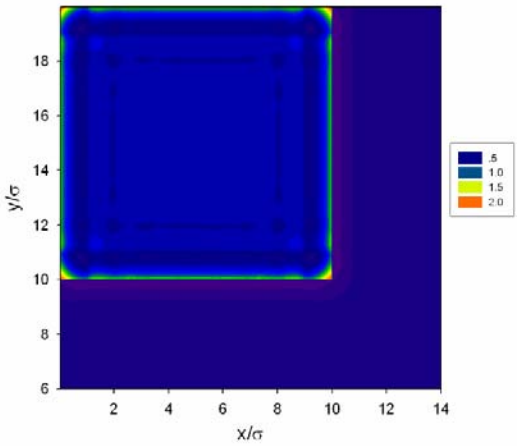

(c)

Figure 7.10. (a) Transmitted light CCD image of 4 μm PS colloids coated with F108 pluronic (PEO-PPO-PEO) levitated in aqueous 0.2M NaCl above 50 μm x 50 μm x 4 nm (l x w x h) Au square films separated by 50 μm regions with 10 nm Au films (all on glass substrate). 10 nm Au films appear darker than 4 nm Au films. (b) Density profile of hard disk particles around square well (well depth = $-2k_BT$) by MC and forward DFT at $\rho_b\sigma^2$=0.3. The open circles (O) are MC results. The solid (—), dash (--), and dash-dot (- -) are RY+LBF, RY+HNC and RY+ZHZ closure combination respectively. (c) 2d contour plot for density profile hard disk particles around square well (well depth = $-3.2k_BT$) by MC at $\rho_b\sigma^2$=0.06.

Fig. 7.11a and 7.11b show the equilibrium partitioning number of hard disk near square well at different depth (ε) and different ϕ from MC and DFT. As we seen from Fig. 7.11a and 7.11b, RY+LBF shows better prediction than RY+HNC in equilibrium partitioning number calculation. The accuracy of prediction declines as the ε or ϕ increasing.

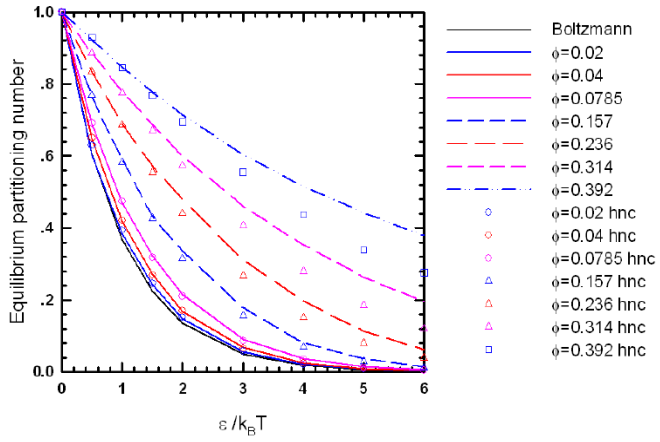

(a)

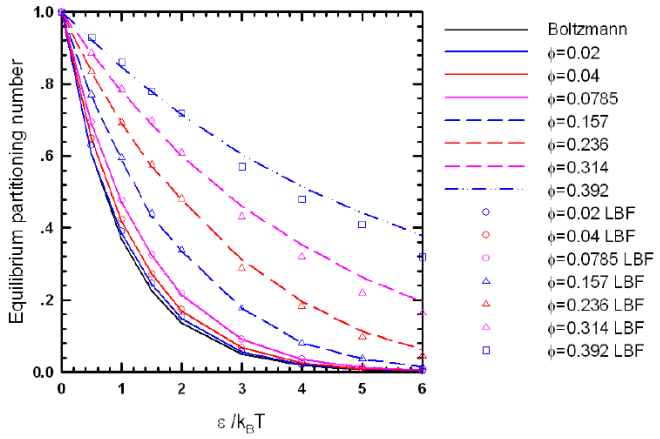

(b)

Figure 7.11. (a) Equilibrium partitioning number of hard disk around square well at different ε and ϕ by MC and forward DFT RY+HNC closures combination. Different symbols and lines represent different ϕ as given in the legend. (b) Same as (a) except using RY+LBF closures combination.

7.5 Conclusions

We successfully implement the DFT formulation of ZR to the colloidal monolayer self-assembly on patterned surfaces in both forward and inverse analysis. The accuracy of the predictions depended on the bulk particle density, potential well depth and the choice of DFT closure relationships. The new closure we modified from Zhou shows high accuracy in all the cases we studied. Results from different particle-particle and particle-surface potentials under different surface topographies demonstrated that the RY+LBF combination of closures is a good general choice. This closure combination should produce acceptable results (< 0.1 k_BT maximum deviation from true potential) at certain density ($\rho_b\sigma^2$ <0.5) for hard surface and ($\rho_b\sigma^2$ <0.1) for certain external potential strength (<4k_BT) at different particle-particle, particle-surface and surface landscapes. The RY+LBF is a very useful tool to 'imaging' the three dimensional energy landscape of patterned surface very accurately and quickly (less than 1 minutes by typical PC with bin dimension 400×400). Higher densities and strong potential strengths are still problematic and will be the focus of future work, as will application of the theory to actual experimental data.

8. CONCLUSIONS

The goal of this research was to present density function theory (DFT) as a useful numerical tool for the microscopy experiment techniques such as confocal scanning laser microscope (CSLM), and so called "Diffusing Colloidal Probes Microscopy" (DCPM) and son on to interpret the particle-surface interactions in colloidal interfacial systems from experimentally monitored three dimensional trajectories of colloidal particles levitated next to a surface. To achieve the goal of this research, we studied four particular problems in this dissertation, we studied four particular problems in this dissertation: (1) measuring colloidal particle-surface interactions on homogeneous planar surface; (2) obtaining colloidal particle-surface interaction on homogeneous planar surface under gravity; (3) studying colloidal self-assembly on chemically and physically patterned surfaces; (4) investigating monolayer colloidal self-assembly on patterned surfaces.

Initially, we implement the DFT formulation of Zhou and Ruckenstein (ZR) to make predictions of density profiles and particle-surface potentials for several different colloidal hard sphere potentials: Derjaguin-Landau-Verwey-Overbeek (DLVO) screened electrostatic repulsion; retarded van der Waals (vdW) attraction; and Asakura-Oosawa (AO) depletion attraction. We expect that such a process will be useful in the interpretation of microscopy measurements of inhomogeneous colloidal fluids near homogeneous surfaces. Different choices of DFT were tested for the bulk and inhomogeneous colloidal fluid. The best closure combination, RY+VM, demonstrated good results in predicting density profile for different colloidal potentials compared with Monte Carlo simulation results. The RY+VM closure combination produces good results for predicting particle-surface interaction potential (< 0.1 k_BT maximum deviation from the true potential) at low to moderate bulk densities ($\rho_b\sigma^3 < 0.3$) across the different colloidal interaction types. As bulk particle density and potential well depth increase the accuracy of the forward and inverse predictions decreases. Higher densities and stronger

potential well depths are still problematic and the application of the theory to experimental data will be the focus of future work.

After the successful application of DFT to an inhomogeneous colloidal fluid, we studied the sedimentation equilibrium of a colloidal fluid since the effect of the gravitational potential cannot be ignored for typical colloidal particle sizes on the order of several hundred nanometers when compared with the thermal energy $k_B T$. The DFT formulation of ZR was used to obtain the equilibrium density profile and predict the particle-surface potentials from the density profile information using Monte Carlo results as input. Different versions of DFT tested the RY+VM combination of closures is still the best among the five available closure combinations after the screening process for bulk colloidal particles. Results shows that the RY+VM combination of closures would produce decent agreement (< 0.2 $k_B T$ maximum deviation from true potential) for low total particle density ($\rho_{total}\sigma^3$=0.17, silica particles with k^{-1}=9.7nm, pre-factor=1554, and diameter=720nm). The accuracy of the predicted potential depended on the total particle density and gravitational potential and declines as the particle density increases. The RY+VM closures combinations fail at certain particle density and external potential well depth because of its inherent form. Future work will focus on the performance of closures at higher particle density and stronger gravitational potential. As well as we will compare forward analysis result with CLSM experiment and we expect the inverse analysis can be a very useful tool in predicting the particle-surface potential from CLSM measurements.

The ZR DFT formulation was extended into colloidal self-assembly on patterned surface to equilibrium density profile and particle-surface potentials with high accuracy. We found that the entropy effect for equilibrium density profile may lead to various interesting and dynamic microstructure formation such as nanowires. We expect the inverse analysis to be useful for microscopic measurement of colloidal particle interactions with patterned surfaces such as bimolecular (e.g. DNA, proteins) arrays. The inverse analysis is much faster than the forward analysis and can be done within several minutes on a regular PC. The accuracy of the predictions depended on the bulk particle

density, potential well depth and the choice of DFT closure relationship. Results for different cases we studied demonstrate that the RY+VM combination of closures is a good general choice. This closure combination should produce acceptable results (< 0.1 k_BT maximum deviation from true potential) at low density ($\rho_b\sigma^3$<0.3) across the different colloidal interaction types without gravity; while for colloidal self-assembly on a patterned surface under gravity, RY+VM combination of closures produce decent agreement (< 0.3 k_BT maximum deviation from true potential) at $\rho_{total}\sigma^3$=0.1, k^{-1}=333nm, pre-factor=13728, and diameter=1.58μm, $(4/3)\pi a^3\Delta\rho g$=0.35 $k_BT/\mu m$. Higher densities are still problematic and the application of the theory to actual experimental data will be the focus of future work. High gravitational potential on both chemically and physically pattern surfaces will cause DFT failure and we extend 3D DFT to 2D DFT to solve this issue in the Section 7 because we simplify sphere shaped colloidal particles to disk shaped colloidal particles.

We successfully implement the DFT formulation of ZR to the inhomogeneous quasi-2D colloidal fluids on patterned surface with k_BT-scale energy landscapes in both forward and inverse analysis. The accuracy of the predictions depended on the bulk particle density, potential well depth and the choice of DFT closure relationships. The new closure we modified from Zhou shows high accuracy in all the cases we studied. Results from different particle-particle and particle-surface potentials under different surface features demonstrated that the RY+LBF combination of closures is a good general choice. This closure combination should produce decent agreement (< 0.1 k_BT) at certain density ($\rho_b\sigma^2$ <0.5) for hard surfaces and ($\rho_b\sigma^2$ <0.1) for certain external potential strengths (<4k_BT) at different particle-particle, particle-surface and surface landscapes. The RY+LBF is a very useful tool to 'imaging' the three dimensional energy landscape of patterned surfaces accurately and quickly (less than 1 minute by typical PC with bin dimension 400×400). Higher densities and strong potential strengths are still problematic and the application of the theory to experimental data will be the focus of future work.

9. FUTURE RESEARCH

9.1 Improvement Method for Higher Densities and Strong Potential Well Depth

As indicated in Section 8, higher densities and strong potential well depth are still problematic for all the cases we studied in this dissertation; the predictive ability of the theory declines as the well depth or particle density increase. We may address this issue by finding good closures for specific or general particle-particle interaction potentials. The closure which we modified from Zhou et al.[74] demonstrated such potential since it has advantages in functional form over other closures, i.e. there is no limitation on $\gamma(r)$ value range like others such as PY, where $\gamma(r)$ must great than -1. This is critical especially for higher densities or strong potential well depth. The new closure showed it's highly successful work on the two dimensional disk self assembly on different surface features under strong attractive potential. We will test this new closure in 3 dimension sphere shaped particle at high density and strong potential well depth as well as in 2 dimension disk shaped particle.

Another way to solve this issue is to using third order + second order perturbation density function theory proposed Zhou,[146] gives the following equation:

$$\rho(\mathbf{r}) = \rho_b \exp\left\{ \begin{array}{l} -\beta\varphi_{ext}(\mathbf{r}) + \int d\mathbf{r}_1 \left(\rho(\mathbf{r}_1) - \rho_b\right) C_0^{(2)}(\mathbf{r}, \mathbf{r}_1; \rho_b) \\ + \dfrac{C_{0hc}^{(1)"}(\rho_b)}{2\left[C_{0hc}^{(1)'}(\rho_b)\right]^3} \int C_{0hc}^{(2)}(r, r"; \rho_b) \left[\int d\mathbf{r}'\left(\rho(\mathbf{r}') - \rho_b\right) C_{0hc}^{(2)}(\mathbf{r}', \mathbf{r}"; \rho_b)\right]^2 dr" \end{array} \right\} \quad (9.1)$$

where $c_0^{(2)}(\mathbf{r},\mathbf{r}_1;\rho_b)$ is the second order correlation function of the bulk fluid, $c_{0hc}^{(2)}(\mathbf{r},\mathbf{r}_1;\rho_b)$ is the second order correlation function of hard core part of the bulk fluid, in which can be substituted by hard sphere second order correlation function, $c_{0hc}^{(1)}(\rho_b)$ is the first order correlation function of hard core part and is difficult or impossible to obtain accurate value. Zhou[146] use a adjustable variable λ to substitute the coefficient

$\frac{C_{0hc}^{(1)''}(\rho_b)}{2\left[C_{0hc}^{(1)'}(\rho_b)\right]^3}$, where λ can be determined through equaling the single wall contacting density obtained in this DFT by adjusting λ with that obtained by simulation.[146] This approach is completely empirical and the global performance of DFT depends on this sum rule. This DFT has been successfully applied into Lennard-Jones, hard core attractive Yukawa fluid, hard core repulsive Yukawa fluid, and inverse power potential[146] at density very close to the freezing point, which will be very useful in improving our higher densities and strong potential well depth.

9.2 Freezing and Pre-crystallization of Colloids on Surfaces

Although the weighted function theories such as weighted density approximations (WDA),[81] modified weighted density approximation (MWDA),[88] planar WDA (PWDA)[90] has been used to study the bulk freezing transition successfully to hard spheres, the Lennard-Jones liquid, the hard core Yukawa fluid and so on, the surface induced freezing is still in its infancy and has much richer scenario of interfacial phase transitions such as wetting, surface reconstruction, and sedimentation equilibrium.[147] Surface freezing refers to several crystalline layers autonomously forming at temperatures well above bulk freezing on a liquid surface; while pre-crystallization refers to the formation of crystalline regions at temperatures below bulk freezing point. The microfabricated patterned surface with periodic topographic structure will be a good template for spherical colloidal particle surface freezing. Number of studies has been reported on surface freezing on patterned surface,[147,148] pre-crystallization on patterned substrates,[149] colloidal crystallization on finite structured templates,[150] crystal structure of hard sphere under gravity[151] by molecular simulation. Only two studies by Rasmussen *et al*.[152] and Chakrabarti *et al.*[153] use density functional theory to investigate the induced freezing and re-entrant melting of hard disk fluid in an external period potential.

More and more applications of classical density function theory will certainly be seen in the near future. These include the surfacing freezing and pre-crystalline

transitions and the latest work by Zhou *et al.*[146] shows very promising result, in which their DFT result is very close to the surface freezing.

9.3 Colloidal Escape Rate from Energetic Surface Pattern Features

Fig. 9.1 shows scaled cross sectional view of 2.2μm SiO2 colloids confined (black) and escaping (gray) from a harmonic potential energy well fit to a single AFM measured feature by Bahukudumbi and Bevan.[144] For the purpose of imaging the energetic landscape of patterned surface, colloidal particles should sample the whole surface instead of sticking irreversibly to the surface to generate equilibrium and dynamic 3 dimension trajectories for the further analysis such as inverse Monte Carlo or inverse DFT. For a single colloidal particle to escape the ~12 k_BT potential well and diffuse over the surface, which will take a very long time. But as we increase the particle concentration, such as in Fig. 9.1, the gray particle only need escape 2~3 k_BT potential well due to the multi-body particle interaction.

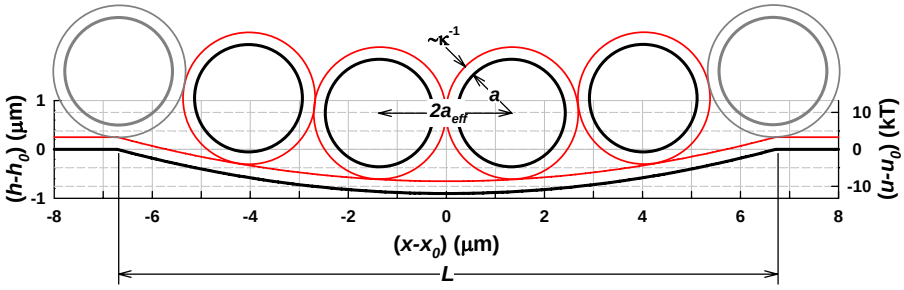

Fig 9.1.[144] Scaled cross sectional view of 2.2μm SiO_2 colloids confined (black) and escaping (gray) from a harmonic potential energy well fit to a single AFM measured feature. Red lines indicate the electrostatic double layer thickness, $\sim 3\kappa^{-1}$=270nm, that produces ~500 nm offset between colloids and the surface. Gravitational potential energy scale, $u(x, y)=Gh(x, y)$, corresponding to physical surface topography.

The free energy well can be define by[154]

$$W_j = k_B T \ln\left(\rho_j / \rho_0\right), \tag{9.2}$$

where ρ_j is the local density inside the patterned feature, ρ_0 is the local density outside the patterned feature, which is the bulk density. As we increase the average colloidal particle density, the free energy well will decrease, which will make particle escape more easily. Density Function Theory can then be used to calculate the equilibrium density profile ρ_j taking account for the multi-body interaction using experiment measured ρ_0, particle-particle interaction, and particle-surface potential as input. As a result, the free energy landscape can be correctly constructed.

After the free energy landscape work, the long time self-diffusivities D_S^L, which is the escape rate can be determined by following[144]

$$D_S^L = D_S^S \left[\exp(w_j / k_B T) + 2\phi g\left(2a_{eff}\right)\right]^{-1}, \tag{9.3}$$

where D_S^S is short-time self-diffusivities, are about half the Stokes-Einstein value ($D_0=k_BT/6\pi\mu a$) due to multi-body hydrodynamic interactions.[155] ϕ is the area fraction, $g(2a_{eff})$ can be calculated through $g(2a_{eff})=(1-0.436\phi_{eff})(1-\phi_{eff})^{-2}$. ϕ_{eff} is the effective area fraction determined by $\phi_{\text{eff}}=\rho_{\text{avg}}\pi a_{\text{eff}}^2$, where a_{eff} is the effective colloid radius from the first peak in the projected 2D radial distribution function, $g(2a_{\text{eff}})$. In Eq. (9.3), D_{S}^{S} takes care of multi-body hydrodynamic interactions.[144] Therefore, we can use Eq. (9.2) and Eq. (9.3) to get the correct colloidal particle escape rate from energetic surface pattern features.

REFERENCES

[1] H. Yabu and M. Shimomura, Langmuir **21** (5), 1709 (2005).

[2] S. A. Safran, Surface Science **500** (1-3), 127 (2002).

[3] K. Carlsson, P. E. Danielsson, R. Lenz, A. Liljeborg, L. Majlof, and N. Aslund, Optics Letters **10** (2), 53 (1985).

[4] W. A. Ducker, T. J. Senden, and R. M. Pashley, Nature **353** (6341), 239 (1991).

[5] D. C. Prieve, Advances in Colloid and Interface Science **82** (1-3), 93 (1999).

[6] G. M. Kepler and S. Fraden, Physical Review letter **73** (2), 356 (1994).

[7] H. J. Wu and M. A. Bevan, Langmuir **21** (4), 1244 (2005).

[8] M. P. Allen and D. J. Tildesley, *Computer Simulation of Liquids*. (Clarendon Press, Oxford, 1987).

[9] I. K. Snook and D. Henderson, Journal of Chemical Physics **68** (5), 2134 (1978).

[10] J.-P. Hansen and I. R. McDonald, *Theory of Simple Liquids*, 2nd ed. (Academic Press, London, 1990).

[11] J. Z. Wu, Aiche Journal **52** (3), 1169 (2006).

[12] H. Lowen, Journal of Physics-Condensed Matter **14** (46), 11897 (2002).

[13] C. Caccamo, Physics Reports-Review Section of Physics Letters **274** (1-2), 1 (1996).

[14] Y. Q. Zhou and G. Stell, Journal of Chemical Physics **92** (9), 5533 (1990).

[15] Y. Q. Zhou and G. Stell, Journal of Chemical Physics **92** (9), 5544 (1990).

[16] M. Minsky, Scanning **10** (4), 128 (1988).

[17] A. D. Dinsmore and D. A. Weitz, Journal of Physics-Condensed Matter **14** (33), 7581 (2002).

[18] U. Gasser, E. R. Weeks, A. Schofield, P. N. Pusey, and D. A. Weitz, Science **292** (5515), 258 (2001).

[19] W. K. Kegel and A. van Blaaderen, Science **287** (5451), 290 (2000).

[20] E. R. Weeks, J. C. Crocker, A. C. Levitt, A. Schofield, and D. A. Weitz, Science **287** (5453), 627 (2000).

[21] G. Binnig, C. F. Quate, and C. Gerber, Physical Review Letters **56** (9), 930 (1986).

[22] G. Binnig and H. Rohrer, Helvetica Physica Acta **55** (2), 128 (1982).

[23] D. Leckband and J. Israelachvili, Q Rev Biophys **34** (2), 105 (2001).

[24] J. N. Israelachvili, *Intermolecular and Surface Forces* 2nd ed. (Academic Press, San Diego, 1991).

[25] P. Vermette, L. Meagher, E. Gagnon, H. J. Griesser, and C. J. Doillon, Journal of Controlled Release **80** (1-3), 179 (2002).

[26] T. Strunz, K. Oroszlan, R. Schafer, and H. J. Guntherodt, Proceedings of the National Academy of Sciences of the United States of America **96** (20), 11277 (1999).

[27] R. R. Dagastine, G. W. Stevens, D. Y. C. Chan, and F. Grieser, Journal of Colloid and Interface Science **273** (1), 339 (2004).

[28] D. C. Prieve, F. Luo, and F. Lanni, Faraday Disc. **83**, 297 (1987).

[29] D. C. Prieve and N. A. Frej, Langmuir **6** (2), 396 (1990).

[30] M. A. Bevan and D. C. Prieve, Langmuir **15** (23), 7925 (1999).

[31] M. A. Bevan and D. C. Prieve, J. Chem. Phys. **113** (3), 1228 (2000).

[32] M. A. Bevan and D. C. Prieve, Langmuir **16** (24), 9274 (2000).

[33] L. Helden, G. H. Koenderink, P. Leiderer, and C. Bechinger, Langmuir **20** (14), 5662 (2004).

[34] S. K. Robertson and S. G. Bike, Langmuir **14** (4), 928 (1998).

[35] G. M. Kepler and S. Fraden, Langmuir **10** (8), 2501 (1994).

[36] R. Klein, H. H. von Grunberg, C. Bechinger, M. Brunner, and V. Lobaskin, Journal of Physics-Condensed Matter **14** (33), 7631 (2002).

[37] J. C. Crocker and D. G. Grier, Journal of Colloid and Interface Science **179** (1), 298 (1996).

[38] J. K. H. Horber and M. J. Miles, Science **302** (5647), 1002 (2003).

[39] C. Bustamante, Z. Bryant, and S. B. Smith, Nature **421** (6921), 423 (2003).

[40] W. N. Everett, H. J. Wu, S. G. Anekal, H. J. Sue, and M. A. Bevan, Biophysical Journal **92** (3), 1005 (2007).

[41] D. Frenkel and B. Smit, *Understanding molecular simulation:From algorithms to applications*. (Academic Press, San Diego, 2002).

[42] R. Evans, in *Fundamentals of Inhomogeneous Fluids*, edited by D. Henderson (Marcel-Dekker, New York, 1992), pp. 85.

[43] R. S. Saksena and L. V. Woodcock, Journal of Chemical Physics **122** (16), 164501 (2005).

[44] M. Schmidt, Journal of Physics-Condensed Matter **15** (1), S101 (2003).

[45] S. Q. Zhou and E. Ruckenstein, Journal of Chemical Physics **112** (18), 8079 (2000).

[46] H. Y. Chen and H. R. Ma, Journal of Chemical Physics **125** (2), 024510 (2006).

[47] M. Schmidt, M. Dijkstra, and J. P. Hansen, Journal of Physics-Condensed Matter **16** (38), S4185 (2004).

[48] T. Biben, J. P. Hansen, and J. L. Barrat, Journal of Chemical Physics **98** (9), 7330 (1993).

[49] S. Q. Zhou, Physical Review E **63** (5), 051203 (2001).

[50] L. Belloni, Journal of Chemical Physics **123** (20), 204705 (2005).

[51] A. Fortini, M. Schmidt, and M. Dijkstra, Physical Review E **73** (5), 051502 (2006).

[52] M. D. Carbajal-Tinoco and P. Gonzalez-Mozuelos, Journal of Chemical Physics **117** (5), 2344 (2002).

[53] P. Gonzalez-Mozuelos and M. D. Carbajal-Tinoco, Journal of Chemical Physics **109** (24), 11074 (1998).

[54] H. Lowen, J. P. Hansen, and P. A. Madden, Journal of Chemical Physics **98** (4), 3275 (1993).

[55] C. Caccamo, G. Pellicane, D. Costa, D. Pini, and G. Stell, Physical Review E **60** (5), 5533 (1999).

[56] T. W. Cochran and Y. C. Chiew, Journal of Chemical Physics **121** (3), 1480 (2004).

[57] T. C. Lee, J. T. Lee, D. R. Pilaski, and M. Robert, Physica a-Statistical Mechanics and Its Applications **329** (3-4), 411 (2003).

[58] O. Guzman and J. J. de Pablo, Journal of Chemical Physics **118** (5), 2392 (2003).

[59] G. Rodriguez and L. Vicente, Molecular Physics **87** (1), 213 (1996).

[60] A. Jamnik, Journal of Chemical Physics **109** (24), 11085 (1998).

[61] M. Chavez-Paez, P. Gonzalez-Mozuelos, M. Medina-Noyola, and J. M. Mendez-Alcaraz, Journal of Chemical Physics **119** (14), 7461 (2003).

[62] P. GonzalezMozuelos and J. Alejandre, Journal of Chemical Physics **105** (14), 5949 (1996).

[63] Y. Rosenfeld and G. Kahl, Journal of Physics-Condensed Matter **9** (7), L89 (1997).

[64] S. Bhattacharjee, A. S. Kim, and M. Elimelech, Journal of Colloid and Interface Science **212** (1), 81 (1999).

[65] J. K. Percus and G. J. Yevick, Physical Review **110** (1), 1 (1958).

[66] M. S. Wertheim, Journal of Mathematical Physics **5** (5), 643 (1964).

[67] L. Verlet, Molecular Physics **41** (1), 183 (1980).

[68] S. Labik, A. Malijevsky, and W. R. Smith, Molecular Physics **73** (1), 87 (1991).

[69] N. Choudhury and S. K. Ghosh, Journal of Chemical Physics **116** (19), 8517 (2002).

[70] N. Choudhury and S. K. Ghosh, Journal of Chemical Physics **119** (9), 4827 (2003).

[71] G. A. Martynov and G. N. Sarkisov, Molecular Physics **49** (6), 1495 (1983).

[72] F. J. Rogers and D. A. Young, Physical Review A **30** (2), 999 (1984).

[73] M. Q. Lu, M. A. Bevan, and D. M. Ford, Journal of Chemical Physics, Submitted (2007).

[74] S. Q. Zhou, H. Chen, and X. Q. Zhang, Communications in Theoretical Physics **39** (2), 231 (2003).

[75] S. Nordholm, M. Johnson, and B. C. Freasier, Australian Journal of Chemistry **33** (10), 2139 (1980).

[76] P. Tarazona, Physical Review A **31** (4), 2672 (1985).

[77] P. Tarazona, U. M. B. Marconi, and R. Evans, Molecular Physics **60** (3), 573 (1987).

[78] E. Bruno, C. Caccamo, and P. Tarazona, Physical Review A **35** (3), 1210 (1987).

[79] E. Velasco and P. Tarazona, Physical Review A **36** (2), 979 (1987).

[80] P. C. Ball and R. Evans, Langmuir **5** (3), 714 (1989).

[81] W. A. Curtin and N. W. Ashcroft, Physical Review A **32** (5), 2909 (1985).

[82] W. A. Curtin, Physical Review B **39** (10), 6775 (1989).

[83] W. A. Curtin, Physical Review Letters **59** (11), 1228 (1987).

[84] D. M. Kroll and B. B. Laird, Physical Review A **42** (8), 4806 (1990).

[85] A. R. Denton and N. W. Ashcroft, Physical Review A **42** (12), 7312 (1990).

[86] W. A. Curtin and N. W. Ashcroft, Physical Review Letters **56** (26), 2775 (1986).

[87] N. Choudhury and S. K. Ghosh, Journal of Chemical Physics **104** (23), 9563 (1996).

[88] A. R. Denton and N. W. Ashcroft, Physical Review A **39** (9), 4701 (1989).

[89] R. Ohnesorge, H. Lowen, and H. Wagner, Physical Review A **43** (6), 2870 (1991).

[90] D. W. Marr and A. P. Gast, Physical Review E **47** (2), 1212 (1993).

[91] D. W. Marr and A. P. Gast, Journal of Chemical Physics **99** (3), 2024 (1993).

[92] D. W. M. Marr and A. P. Gast, in *Chemical Applications of Density-Functional Theory* (1996), Vol. 629, pp. 229.

[93] Y. Rosenfeld, Physical Review Letters **63** (9), 980 (1989).

[94] J. K. Percus, in *The Equilibrium Theory of Classical Fluids*, edited by H. L. Frisch and J. L. Lebowitz (W.A. Benjamin, New York, 1964).

[95] M. Calleja, a. N. North, J. G. Powles, and G. Rickayzen, Molecular Physics **73** (5), 973 (1991).

[96] N. Choudhury and S. K. Ghosh, Journal of Chemical Physics **114** (19), 8530 (2001).

[97] S. Q. Zhou and E. Ruckenstein, Journal of Chemical Physics **112** (11), 5242 (2000).

[98] S. C. Kim and S. H. Suh, Journal of Chemical Physics **117** (21), 9880 (2002).

[99] S. Q. Zhou, Journal of Chemical Physics **113** (19), 8719 (2000).

[100] S. Q. Zhou, European Physical Journal E **3** (4), 343 (2000).

[101] S. Q. Zhou and X. Q. Zhang, Physical Review E **64** (1), 011112 (2001).

[102] G. Min, M. A. Bevan, D. C. Prieve, and G. D. Patterson, Colloids & Surfaces A **202** (1), 9 (2002).

[103] M. A. Bevan, S. N. Petris, and D. Y. C. Chan, Langmuir **18** (21), 7845 (2002).

[104] R. Rajagopalan and K. S. Rao, Physical Review E **55** (4), 4423 (1997).

[105] L. Reatto, D. Levesque, and J. J. Weis, Physical Review A **33** (5), 3451 (1986).

[106] F. Lado, Journal of Chemical Physics **47** (11), 4828 (1967).

[107] F. Lado, Journal of Chemical Physics **49** (7), 3092 (1968).

[108] S. Labik, A. Malijevsky, and P. Vonka, Molecular Physics **56** (3), 709 (1985).

[109] F. Lado, J. Comput. Phys. **8** (3), 417 (1971).

[110] W. H. Press, B. P. Flannery, S. A. Teukolsky, and W. T. Vetterling, *Numerical Recipes in FORTRAN: The Art of Scientific Computing*, 2nd ed. (Cambridge University Press, New York, 1992).

[111] W. B. Russel, D. A. Saville, and W. R. Schowalter, *Colloidal Dispersions*. (Cambridge University Press, New York, 1989).

[112] A. P. Gast and W. B. Russel, Physics Today **51** (12), 24 (1998).

[113] P. Gonzalezmozuelos, J. Alejandre, and M. Medinanoyola, Journal of Chemical Physics **95** (11), 8337 (1991).

[114] N. Choudhury and S. K. Ghosh, Journal of Chemical Physics **111** (4), 1737 (1999).

[115] D. Fu, Y. G. Li, and J. Z. Wu, Physical Review E **68** (1), 011403 (2003).

[116] M. Q. Lu, M. A. Bevan, and D. M. Ford, Journal of Chemical Physics **122** (22), 224710 (2005).

[117] P. N. Pusey, W. C. K. Poon, S. M. Ilett, and P. Bartlett, Journal of Physics-Condensed Matter **6** (JUN), A29 (1994).

[118] A. Malijevsky, S. Labik, and W. R. Smith, Molecular Physics **72** (1), 193 (1991).

[119] G. Sarkisov, Journal of Chemical Physics **114** (21), 9496 (2001).

[120] R. E. Beckham and M. A. Bevan, in preparation (2007).

[121] J. Perrin, Comptes Rendus Hebdomadaires Des Seances De L Academie Des Sciences **158**, 1168 (1914).

[122] A. Mori, S. Yanagiya, Y. Suzuki, T. Sawada, and K. Ito, Journal of Chemical Physics **124** (17) (2006).

[123] S. V. Savenko and M. Dijkstra, Physical Review E **70** (5), 051401 (2004).

[124] N. Choudhury and S. K. Ghosh, Journal of Chemical Physics **116** (1), 384 (2002).

[125] S. Q. Zhou and H. W. Sun, Journal of Physical Chemistry B **109** (13), 6397 (2005).

[126] S. Q. Zhou and A. Jamnik, Journal of Chemical Physics **123** (12) (2005).

[127] C. Alba-Simionesco, B. Coasne, G. Dosseh, G. Dudziak, K. E. Gubbins, R. Radhakrishnan, and M. Sliwinska-Bartkowiak, Journal of Physics-Condensed Matter **18** (6), R15 (2006).

[128] H. Dong and G. T. Evans, Journal of Chemical Physics **125** (20), 204506 (2006).

[129] S. G. Anekal and M. A. Bevan, Journal of Chemical Physics **122** (3), 034903 (2005).

[130] I. Chung, J. B. Witkoskie, J. P. Zimmer, J. Cao, and M. G. Bawendi, Phys. Rev. B **75** (4), 045311 (2007).

[131] S. Q. Zhou, Chinese Physics Letters **20** (12), 2107 (2003).

[132] U. Jonas, A. del Campo, C. Kruger, G. Glasser, and D. Boos, Proceedings of the National Academy of Sciences of the United States of America **99** (8), 5034 (2002).

[133] J. S. Shumaker-Parry and C. T. Campbell, Analytical Chemistry **76** (4), 907 (2004).

[134] C. F. Wertz and M. M. Santore, Langmuir **17** (10), 3006 (2001).

[135] C. D. Frisbie, L. F. Rozsnyai, A. Noy, M. S. Wrighton, and C. M. Lieber, Science **265** (5181), 2071 (1994).

[136] H. J. Wu, W. N. Everett, S. G. Anekal, and M. A. Bevan, Langmuir **22** (16), 6826 (2006).

[137] J. Aizenberg, P. V. Braun, and P. Wiltzius, Physical Review Letters **84** (13), 2997 (2000).

[138] L. J. D. Frink and A. G. Salinger, Journal of Chemical Physics **110** (12), 5969 (1999).

[139] L. B. Goetting, T. Deng, and G. M. Whitesides, Langmuir **15** (4), 1182 (1999).

[140] K. M. Chen, X. P. Jiang, L. C. Kimerling, and P. T. Hammond, Langmuir **16** (20), 7825 (2000).

[141] A. D. Dinsmore and A. G. Yodh, Langmuir **15** (2), 314 (1999).

[142] K.-h. Lin, J. C. Crocker, V. Prasad, A. Schofield, D. A. Weitz, T. C. Lubensky, and A. G. Yodh, Physical Review Letters **85** (8), 1770 (2000).

[143] G. M. Whitesides and B. Grzybowski, Science **295** (5564), 2418 (2002).

[144] P. P. Bahukudumbi and M. A. Bevan, Journal of Chemical Physics **In press** (2007).

[145] E. Kokkoli and C. F. Zukoski, Langmuir **17** (2), 369 (2001).

[146] S. Q. Zhou and A. Jamnik, Physical Chemistry Chemical Physics **8** (34), 4009 (2006).

[147] M. Heni and H. Lowen, Physical Review Letters **85** (17), 3668 (2000).

[148] A. Esztermann and H. Lowen, Journal of Physics-Condensed Matter **17** (9), S429 (2005).

[149] M. Heni and H. Lowen, Journal of Physics-Condensed Matter **13** (21), 4675 (2001).

[150] A. Cacciuto and D. Frenkel, Physical Review E **72** (4), 041604 (2005).

[151] A. Mori, S. Yanagiya, Y. Suzuki, T. Sawada, and K. Ito, Science and Technology of Advanced Materials **7** (3), 296 (2006).

[152] L. L. Rasmussen and D. W. Oxtoby, Journal of Physics-Condensed Matter **14** (46), 12021 (2002).

[153] J. Chakrabarti, H. R. Krishnamurthy, and A. K. Sood, Physical Review Letters **73** (21), 2923 (1994).

[154] J. A. Thomas and A. J. H. McGaughey, Journal of Chemical Physics **126** (3) (2007).

[155] S. Anekal and M. A. Bevan, J. Chem. Phys. **125** (3), 034906 (2006).

VITA

Mingqing Lu received his Bachelor of Science degrees in chemical engineering and computer science from Daqing Petroleum Institute, China. He joined the Department of Chemical Engineering at Texas A&M University in August 2003 as a Ph.D. student. His current research interests include Monte Carlo simulation and density function theory for colloidal fluids.

Mr. Lu may be reached at Department of Chemical Engineering (c/o Dr. David Ford), University of Massachusetts Amherst, Amherst, Massachusetts, USA 01003-9303. His email address is mingqinglu@gmail.com.